Models for the Circumstellar Medium of Long Gamma-Ray Burst Progenitor Candidates

Models for the Circumstellar Medium of long Gamma-Ray Burst Progenitor Candidates
Allard Jan van Marle
Ph. D. Thesis Utrecht University, May 2006
ISBN: 90-39342113

Models for the Circumstellar Medium of Long Gamma-Ray Burst Progenitor Candidates

Modellen van de Materie rond Sterren, die mogelijk Langdurige Gamma Flitsen Voortbrengen

(met een samenvatting in het Nederlands)

Proefschrift

Ter verkrijging van de graad van doctor aan de Universiteit Utrecht op gezag van de Rector Magnificus, Prof. Dr. W. H. Gispen, in gevolge het besluit van het College voor Promoties in het openbaar te verdedigen op woensdag 3 mei 2006 des middags te 12:45 uur

door

Allard Jan van Marle

geboren op 19 maart 1978 te Amsterdam

Promotor: Prof. Dr. N. Langer
Faculteit der Natuur- en Sterrenkunde Universiteit Utrecht

This research was done as part of the AstroHydro3D project.
(http://www.strw.leidenuniv.nl/AstroHydro3D/)
This work was sponsored by the Stichting Nationale Computerfaciliteiten (National Computing Facilities Foundation, NCF), with financial support from the Nederlandse Organisatie voor Wetenschappelijk Onderzoek (Netherlands Organization for Scientific Research, NWO).

Who sees with equal eye, as God of all,
A hero perish, or a sparrow fall,
Atoms or systems into ruin hurl'd,
And now a bubble burst, and now a world.

Alexander Pope (1688-1744), Essay on Man

Cover page: circumstellar medium around a massive star.

Contents

1

Introduction

1.1 Introduction

Massive stars are rare. For every thousand solar type stars, the universe forms only one star with a mass ten times as large (Rana [58]). Increasingly rare moreover, since massive stars have far shorter lives than their smaller cousins. Whereas the sun has an expected lifetime of about ten **billion** years, a 10 $M_\odot$ (solar mass) star will die after less than twenty seven **million** years (Maeder & Meynet [40]). In spite of their small numbers and short lives, massive stars have considerable impact on the evolution of their host galaxy, since they are the source of heavy elements with isotope mass numbers between mass 16 and 90 (Woosley et al. [86]). During their lives, massive stars have an impact on their surroundings, since they add large amounts of mass, kinetic energy and radiation to their surroundings (Freyer et al. [20]). Their endings are catastrophic: they explode as Type II or Type Ib/c supernovae. (Type II supernovae are supernova explosions that show the presence of a significant amount of hydrogen in the supernova ejecta. Type Ib supernovae show little or no hydrogen and Type Ic supernovae show neither hydrogen nor helium.) When this occurs, they briefly light up the sky as a whole galaxy, and they eject their outer layers into the surrounding medium at high velocity. These ejecta disturb the surrounding gas so much that a new round of star formation can be triggered (Rana & Gajria [59]). It is currently believed, that massive stars are the progenitors of long gamma-ray bursts (Woosley [84]; MacFadyen & Woosley [39]). For an explanation of the gamma-ray burst phenomenon, see Sect. 1.6.

In this thesis, we describe the effect of the evolution of a massive star on the surrounding medium. We will then explore the connection between massive stars and gamma-ray bursts by comparing our results for the circumstellar medium of massive stars with the observations and models of long gamma-ray bursts.

1.2 Evolution of massive stars

Massive stars start their lives on the main sequence, where they produce energy by fusing hydrogen in their core. This energy leaves the star at the surface in the form of radiation and, to a lesser extent, as a stellar wind. The evolution of a star can be described in the Hertzsprung-Russel diagram (see Fig. 1.1). This shows the luminosity of the star versus its surface temperature. Typically, a massive main sequence star (O star) will have a surface temperature of more than 25 000 K, giving it a blue color, and a surface luminosity of more than 100 000 times the luminosity of the sun. As long as the supply of hydrogen in the core is not exhausted the star maintains its surface temperature and luminosity. Once the hydrogen runs out, the star shrinks and the temperature in the center will increase accordingly. Soon it reaches the point, where it can start to fuse hydrogen in a layer outside the core (where hydrogen is still available.)

As the central temperature increases even further, the star starts to fuse Helium in its core. As a result of this extra energy production the star swells up, which causes the surface temperature to drop (it moves to the right in the Hertzsprung-Russel diagram). It now becomes either a red supergiant (RSG) or a luminous blue variable (LBV), depending on its original mass. Red Supergiants are extremely large, cold stars. A luminous blue variable is an extremely bright star. So bright, that the radiation pressure in the outer layers is nearly equal to the gravitational force, which means that it can expel large amounts of

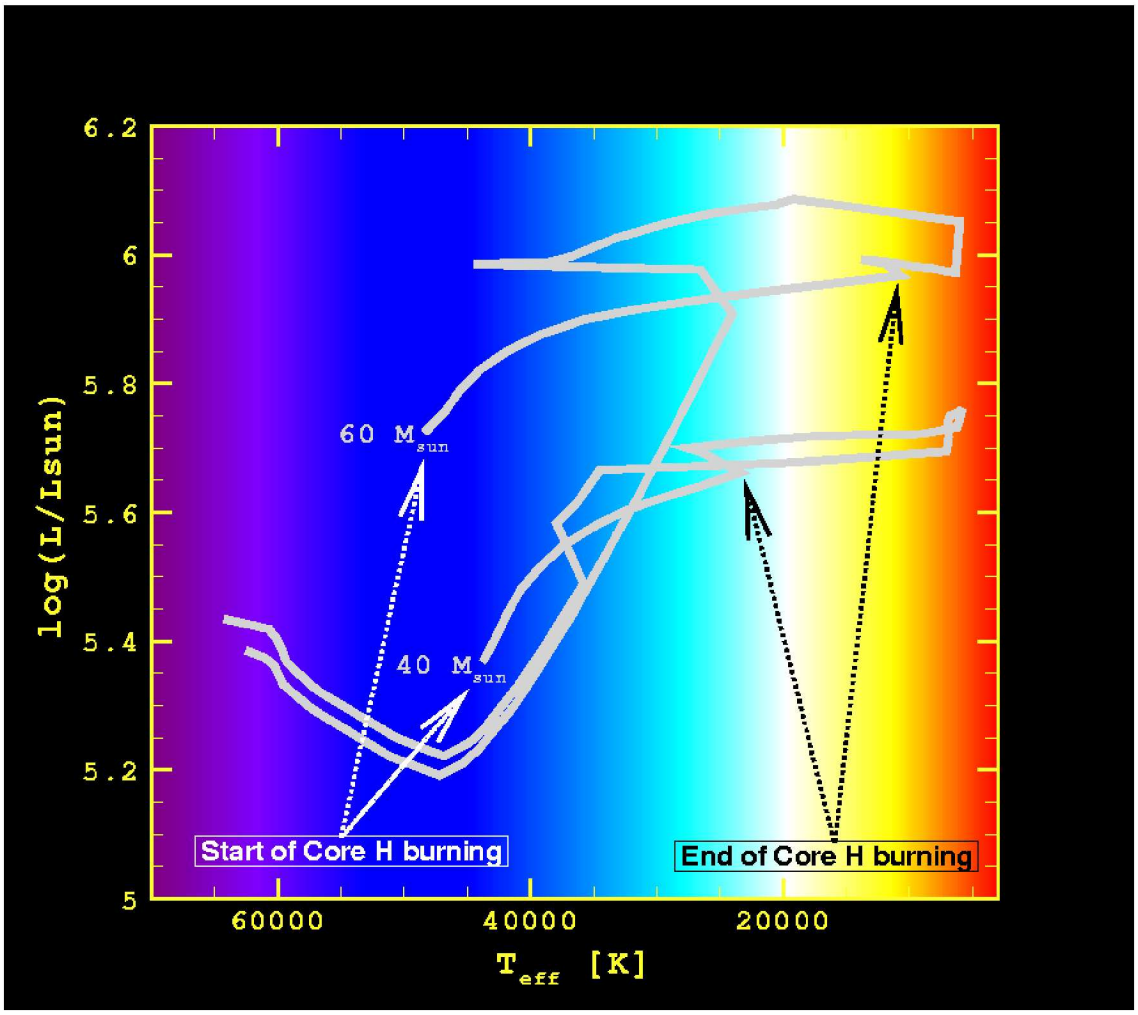

Figure 1.1: Hertzsprung-Russel diagram for the evolution of massive stars, showing surface temperature and luminosity for two stars during their evolution. Both stars start on the main sequence, move toward the right to become a red supergiant (40 $M_\odot$ star) or a luminous blue variable (60 $M_\odot$ star) and then turn back to the left, as they evolve into Wolf-Rayet stars. (Stellar evolution tracks from Schaller et al. [63].)

mass in a very short time. Eventually, if the star is massive enough (more than $\sim 30\ M_\odot$, it evolves into a Wolf-Rayet star, a hot ($T \geq 50\,000$ K), very bright ($L \sim 10^{5-6}\ L_\odot$, where $L_\odot$ is the solar luminosity) star, which loses mass in the form of stellar wind at a high rate (Schaller et al. [63]). When the helium in the core runs out as well and the star starts to fuse even heavier elements. However, it has nearly reached the end of its life and these final stages of fusing heavier elements will only last a short period of time.

In the end, the star loses its battle to produce energy, as the fuel supply runs out. It collapses and in the case of a massive star ends its life as a supernova, in order to become a neutron star (original star $\lesssim 30\ M_\odot$) or a black hole (Eldridge & Tout [17]).

1.3 Stellar wind interactions around massive stars

Massive stars lose a significant part of their mass during their evolution. This matter leaves the star in the form of a stellar wind, a stream of matter that is driven away from the surface of the star. The parameters of this stellar wind depend on luminosity, mass, radius and metallicity of the star. These in turn change as the star evolves. Since the wind interacts with the surrounding matter and these interactions depend on the wind parameters, we can use the morphology of the circumstellar medium (CSM) as a finger print of the past evolution of the star.

1.3.1 Wind interactions around main sequence stars

As the stellar wind material leaves the star, it comes into collision with the surrounding gas. Since the wind is moving at supersonic speed, a shock is formed where it collides with the interstellar medium (ISM). The wind sweeps up the surrounding gas into a shell that moves away from the star, driven by the wind, forming a bubble around the star. The morphology of the bubble is as follows: Moving away from the star, we first encounter the free-streaming stellar wind, which moves away from the star with a constant velocity. The density of the wind decreases with the radius squared. The next layer of the circumstellar bubble consists of shocked wind material. This is the part of the stellar wind that has passed through the wind termination shock. It has decelerated considerably and most of its kinetic energy has been converted into thermal energy. This 'hot bubble' of shocked wind material has near constant density and pressure. At the outer edge of the hot bubble, we encounter the moving shell of shocked interstellar material. This shell has been swept up originally by the stellar wind and is now moving outward, driven by the thermal pressure of the 'hot bubble'. Outside this shell we find the unperturbed ISM, into which the shell moves. This is the situation for a wind with constant, or near constant parameters, such as is produced during the main sequence (Weaver et al. [79], García-Segura et al. [24], [25]).

1.3.2 Wind interactions around post main sequence stars

As a massive star reaches the end of it core hydrogen burning phase, it leaves the main sequence to become a red supergiant (RSG), or a luminous blue variable (LBV). During this phase the radius of the star increases, causing a decrease in wind velocity, while the mass loss rate increases. As a result, a new shell (the RSG/LBV shell) is formed at the wind termination shock of the old main sequence bubble.

What happens next depends on the nature of the central star. For stars with an original mass of 20....30 $M_\odot$, the RSG phase is the end of their evolution, so the morphology of the bubble will not change significantly any longer. Stars with a higher mass, but less than ca. 50 $M_\odot$, will eventually become Wolf-Rayet stars (Maeder, A. & Meynet [41]). They move toward the left of the Hertzsprung-Russel diagram. Wolf-Rayet winds are very strong, both in terms of mass loss rate and wind velocity. This new, strong wind sweeps up the material of the RSG wind into a third shell. This process is reminiscent of the formation of 'planetary nebulae' around post-AGB (Asymptotic Giant Branch) stars, where the fast post-AGB wind sweeps up the slow AGB wind (Kwok [34]). The Wolf-Rayet wind driven shell travels outward quickly, until it comes into collision with the

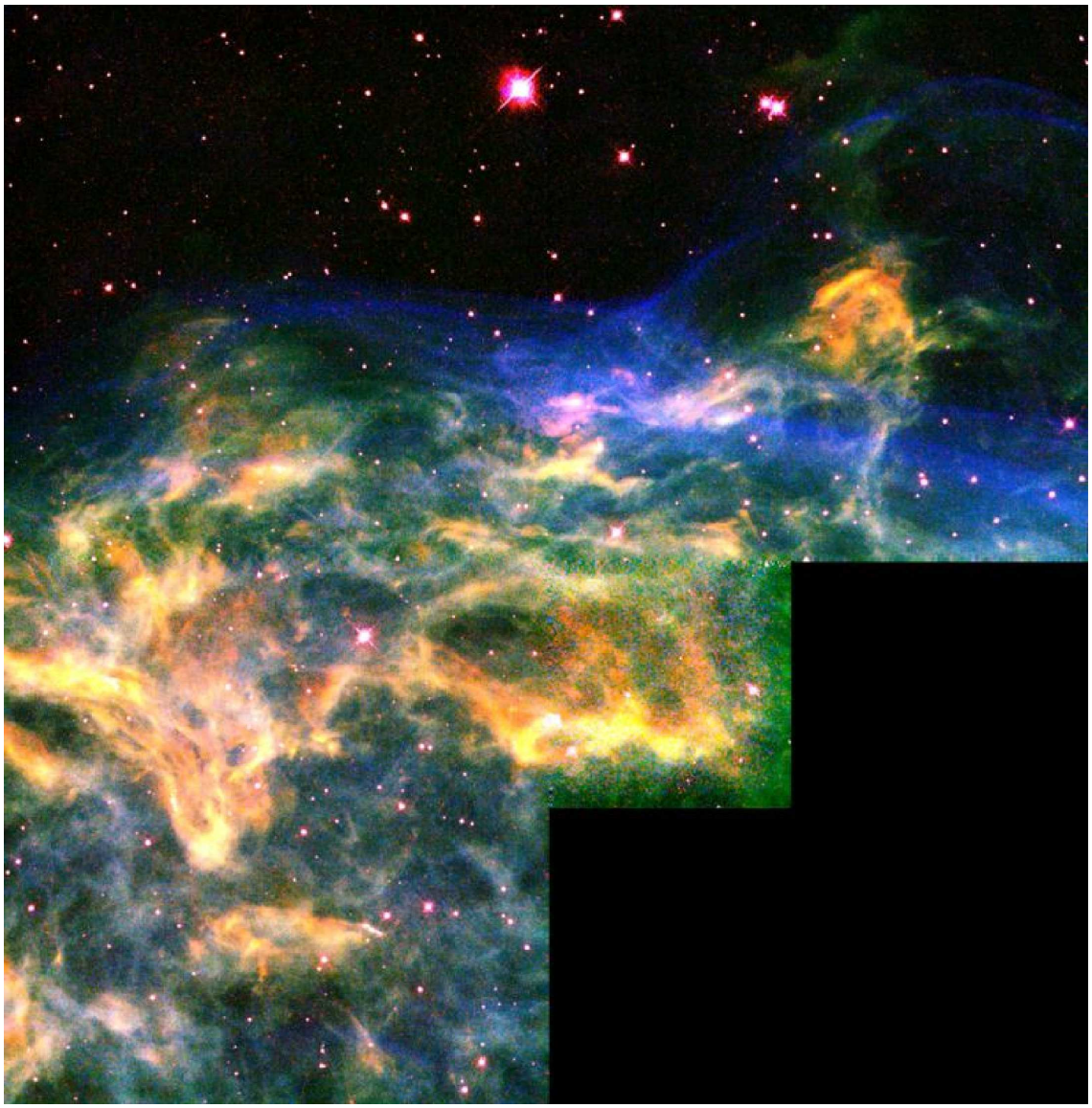

Figure 1.2: The 'Crescent Nebula', NGC 6888, was formed by the collision between a Wolf-Rayet wind driven shell and the older red supergiant shell. This image show only a small part of the total nebula. The colors represent ionization states, with blue being the highest and red the lowest. The highly structured morphology is the result of hydrodynamical instabilities, both during and after the collision (HST).

RSG shell. Neither shell survives the collision and their remnants move out into the hot bubble, where they eventually dissipate. Shells like these, as well as their post-collision remnants can be observed as circumstellar nebulae (García-Segura et al. [25]). A good example of such a nebulae is NGC 6888, also known as the 'Crescent Nebula' (see Fig. 1.2).

Stars with a mass of more than about 50 $M_\odot$ become LBVs rather than RSGs after their main sequence evolution. The circumstellar medium generally follows the same evolution as that of 30...50 $M_\odot$ stars. However, the LBV wind is, typically, faster than the wind of a RSG, while the LBV phase is much shorter. As a result, an LBV shell moves away from the central star more quickly than an RSG shell. Therefore, it has a lower

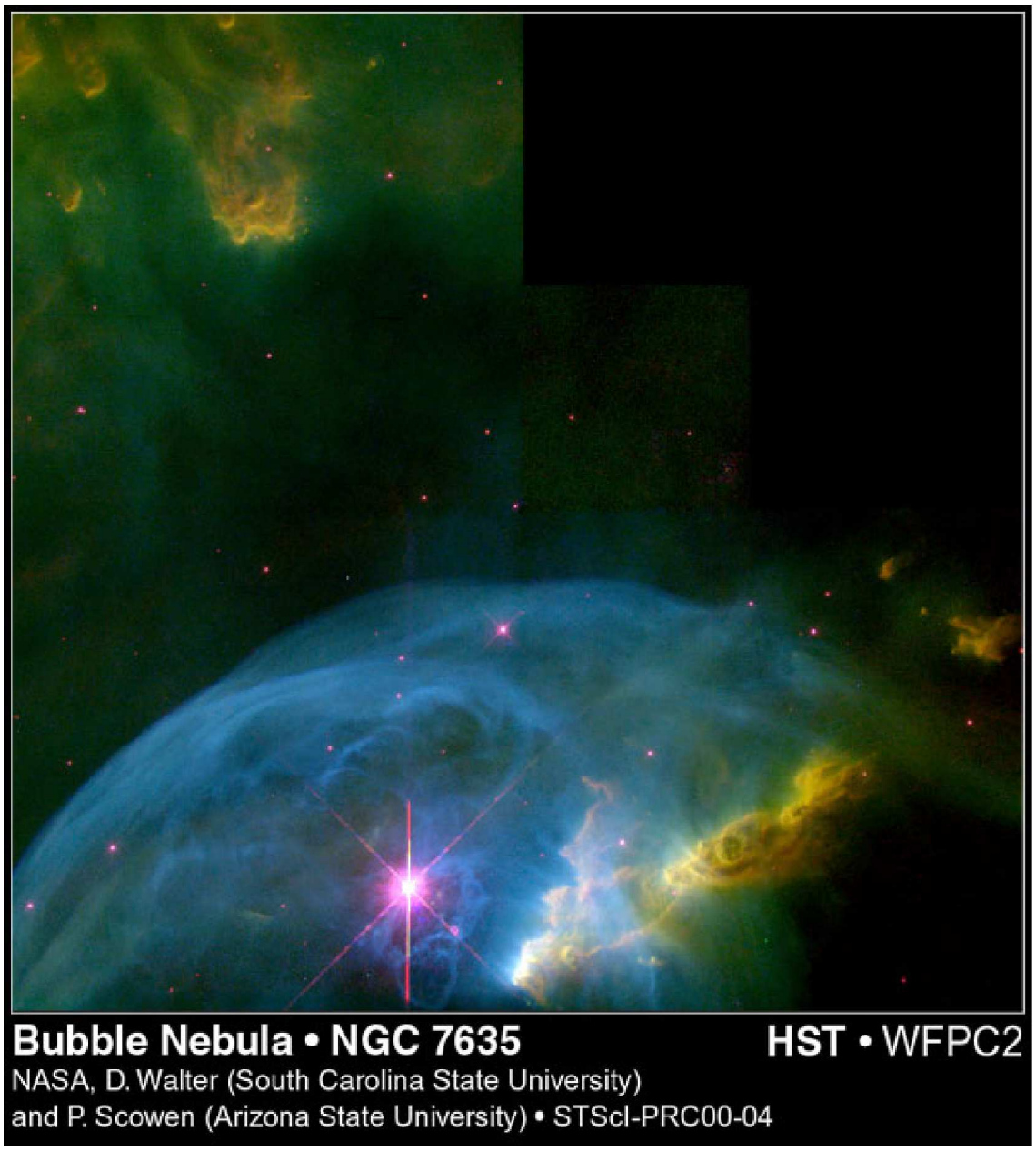

Figure 1.3: The 'Bubble Nebula',NGC 7635, shows the wind bubble (blue) sweeps up the surrounding ionized gas (green). Like in Fig. 1.2 the colors show degree of ionization, with blue the highest and red the lowest ionization states. The central stars is not visible in this image (HST).

density when the following Wolf-Rayet shell collides with it. The collision tends to be less destructive, leaving the matter of the two shells in a single, very unstable shell (van Marle et al. [75]).

1.4 The influence of photo-ionization on the evolution of the circumstellar medium

Massive stars not only have strong winds, they also produce a large number of high-energy photons. As a result, the CSM around such stars tends to be photo-ionized. Instead of sweeping up a cold ISM, the wind now sweeps up the photo-ionized gas of the HII region that surrounds the star. This can be observed in the 'Bubble nebula' NGC 7635 (see Fig. 1.3). If the wind is strong enough (as in the case of stars that become LBVs), the thermal pressure of the HII region is insufficient to stop the outward movement of the shell. However, if the wind is not strong enough, the velocity of the shell drops below the local sound speed (~ 10 km s^{-1} for ionized hydrogen). Once the shell becomes subsonic, it starts to expand under its own internal pressure and eventually dissipates. This leaves a structured main sequence bubble, which has a density discontinuity half way, where the inner part of the bubble consists of shocked wind material, while the outer part consists of photo-ionized ISM. Together, they drive a shell into the surrounding medium, which marks the Strömgren radius, i.e.the outer limit of hydrogen ionization of the star.

Once the star leaves the main sequence, its surface temperature drops, which in turn decreases the number of high energy photons. An LBV still puts out enough photons to ionize the surrounding bubble, but an RSG is too cold. (In Fig. 1.1 both stars seem to reach about the same minimum temperature. However, the 40 $M_\odot$ star stays at that temperature, whereas the surface temperature of the 60 $M_\odot$ star immediately increases again.) Since stars that become RSGs typically have the more complicated bubble described above, the region outside the shocked wind material is no longer photoionized. Its thermal pressure drops and the shells at its outer edge is no longer driven outward and eventually starts to dissipate. The region of shocked wind material maintains its high temperature and starts to drive a new shell into the old HII region. Since the density in the HII region is lower than in the original ISM, this shell will move outward rapidly.

Wolf-Rayet stars are very hot and therefore produce a large number of high energy photons. However, their immediate surroundings contain a large amount of mass, with several high density shells, which can 'trap' the photon field. As a result, the Strömgren radius of a Wolf-Rayet star can vary wildly from one direction to another, as local clumps of wind or shell material stop the high energy photons from moving further outward.

1.5 How to model the wind interactions

The hydrodynamical interactions described above can be modeled numerically. Analytical solutions only exist for the interaction between a constant wind and the ISM, and for the interaction between two winds (Castor et al. [7]; Weaver et al. [79]; Ostriker & McKee [49]). However, for the more complex case of time dependent winds, this is no longer possible. Therefore, we use a numerical approach.

1.5.1 Input for the hydrodynamical simulations

As a basis for our simulations we use evolutionary models of massive stars, which provide us with the mass loss history of the star. The mass loss rate is adopted directly from the stellar evolution model, while the wind velocity needs to be calculated separately (using

the escape velocity of the star as basis). The number of ionizing photons follow from the surface temperature of the star.

1.5.2 Numerical hydrodynamics

We use the ZEUS 3D hydrodynamics code by Stone & Norman [67] to simulate the evolution of the circumstellar medium. This is an explicit non-conservative code that solves the hydrodynamical equations as partial, finite difference equations on a fixed, staggered mesh grid. The equations are:

$$\begin{aligned} \frac{\partial \rho}{\partial t} &= -\nabla \cdot (\rho \mathbf{v}), \\ \frac{\partial \mathbf{S}}{\partial t} &= -\nabla \cdot (\mathbf{S}\mathbf{v}) - \nabla P, \\ \frac{\partial e}{\partial t} &= -\nabla \cdot (e\mathbf{v}) - P\nabla \cdot \mathbf{v}, \end{aligned} \tag{1.1}$$

with: ρ the mass density, $\mathbf{v}$ the velocity flow field, $\mathbf{S} = \rho\mathbf{v}$ the momentum vector field, P the thermal pressure and e the internal energy density per unit volume. The relation between thermal pressure and internal energy is given by:

$$P = (\gamma - 1)e, \tag{1.2}$$

with $\gamma = 5/3$ for an adiabatic gas. The ZEUS code can also account for the effects of gravity and magnetic fields. However, neither is used in the research described in this thesis. The first equation in Eq: 1.1 is the continuity equation. It describes the amount of mass in a grid cell in terms of the mass flows entering and leaving the cell. The second equation is the conservation of momentum. The momentum of the mass in a grid cell depends on the mass and velocity of the matter entering and leaving the cell, and on the thermal pressure gradient of the gas. The final equation describes the change in internal energy of the gas as a function of the matter entering and leaving the grid cell, and the compressional heating of the gas.

The code also calculates the amount of energy lost through radiative cooling using the radiative cooling curve from MacDonald & Bailey [38]. This changes the internal energy equation:

$$\frac{\partial e}{\partial t} \rightarrow \frac{\partial e}{\partial t} - n_{\mathrm{e}} n_{\mathrm{H}} \Lambda(T), \tag{1.3}$$

with n_{e} and n_{H} the free electron and total hydrogen particle densities respectively and $\Lambda(T)$ a cooling function, which depends on temperature and metallicity. Since the code does not keep track of composition, only one cooling function is used throughout the simulation.

Photo-ionization can also be included in the simulations; an addition, which is not part of the original code. We use the same routine that was used by García-Segura et al. [26]. This does not solve the equations for radiative transfer. Instead, it calculates the Strömgren radius along each radial gridline, and considers the matter within this radius to be fully ionized, while all matter outside is considered to be neutral.

The stellar wind simulations are generally done in the following manner: We fill a spherical grid with constant density matter (the ISM) and start the simulation by letting

matter flow into the grid in the central region (the stellar wind). The parameters of the wind are adjusted over time, in order to follow the evolution of the central star (García-Segura et al. [24], [25]).

Since 3D calculations are very time consuming, we use the spherical symmetry of the progenitor star in order to simplify the problem. Typically, it is enough to simulate the main sequence phase in only one dimension and use a two-dimensional grid only for the post main sequence phases (see also chapter 3). This method was also used by García-Segura et al. [24], [25].

1.6 Gamma-ray burst - CSM interactions

Gamma-ray bursts are highly energetic events (energy $E \geq 10^{51}$ erg), which are visible from earth in the form of a flash of gamma rays (photons with an energy of more than 10^5 eV). Events within the class of long gamma-ray bursts last seconds up to minutes, and are often followed by an afterglow in x-ray, ultra violet, optical or even radio wavelengths. The most favored theoretical model for long gamma-ray bursts is the collapsar model (Woosley [84]; MacFadyen & Woosley [39]). In this model a massive star collapses at the end of its life to form a black hole. Around this black hole an accretion disk is formed of infalling stellar material. The energy gained from the infalling material is focused, probably by magnetic fields in jets that burst out with relativistic speed from the poles of the collapsing star. The shock that accompanies these jets as they move outward produces the gamma rays.

As the jets move further away from the progenitor star, it encounters the surrounding medium, sweeping it up. Particles accelerated to relativistic speeds in the presence of a strong magnetic field produce synchrotron radiation. This is observed as the gamma-ray burst afterglow.

The predictions of the collapsar model for long gamma-ray bursts are consistent with the observations that supernova type lightcurves dominate the late optical afterglows of two long gamma-ray bursts. These models predict that a fraction of the massive stars which evolve into Type Ib/c supernovae are the progenitors for long gamma-ray bursts. Also the somewhat less massive stars, which explode as Type II supernovae are possible gamma-ray burst progenitors (Rigon et al. [61]).

The gamma-ray burst expands into a medium, that has been shaped by the processes described in Sects. 1.3 and 1.4. Furthermore, the radiation coming from the gamma-ray burst has to pass through that part of the circumstellar medium, which has not yet been touched by the expanding fireball of the gamma-ray burst itself. This gives us at least two ways to detect the influence of the circumstellar medium in our observations of gamma-ray bursts.

First, the gamma-ray burst afterglow is created by synchrotron emission generated as the expanding fireball sweeps up the surrounding medium. Therefore, the lightcurve of the afterglow can give us information about the density the fireball encounters as it moves away from the progenitor. Since the material closest to the progenitor star is the stellar wind, one would expect the density profiles to resemble those of free-streaming winds: a density that decreases with the radius squared. Instead, many gamma-ray burst afterglows seem to be produced in a medium with a constant density (Chevalier & Li [9]; Panaitescu & Kumar [50]; Panaitescu & Kumar, [51]; Chevalier et al. [10]). In this thesis we will try

to find an explanation for this phenomenon (see Chapter 6).

Second, the radiation of the afterglow will be partly absorbed by the CSM. Circumstellar matter will show up in the afterglow as absorption lines. Since the material surrounding the star moves at a number of different velocities, a single absorption line may show up multiple times, each at a different blue-shift relative to the progenitor star. This is the case for gamma-ray burst GRB 021004 (Schaefer et al. [62]), Mirabal et al. [47], Fiore et al. [19] and Starling et al. [65]).

The blue shifted absorption profile can be calculated from the results of our hydrodynamical simulations. We have developed a computer code to do so, which works as follows: We move outward from the star along a radial grid line. At each grid point encountered, we note the local density, temperature and radial velocity. The density, multiplied by the length of the grid cell gives us the local column density. From the local temperature we calculate the Maxwell-Boltzmann distribution for moving particles. These two combined give us the column density as a function of the velocity in the local rest frame along the radial axis. Now all that is left to do, is to move this entire velocity distribution until the average velocity of the particles conforms to the bulk radial velocity of the gas. This gives us the column density as a function of radial velocity for gas at the local temperature. We repeat this process for each radial grid point. Adding up the results for each radial velocity interval gives us the column density as a function of radial velocity. For an optically thin gas this is the equivalent of the absorption as a function of blue-shift. Since the ZEUS hydrodynamics code does not keep track of the composition of the gas, we can not produce an actual spectrum. However, we can predict how many blue-shifted components a single absorption feature can generate.

In Chapters 4 and 5 we discuss these models and explain where in the CSM these absorption lines are produced and how this helps us in constraining gamma-ray burst progenitors.

1.7 Conclusions

In this thesis we show the results of numerical hydrodynamical simulations of the circumstellar medium of those stars that are thought to be potential progenitors of long gamma-ray bursts. We investigate the surroundings of such stars and the ways in which those surroundings show up in the observations of gamma-ray bursts.

Our simulations are primarily one and two dimensional. We have also done a limited study of the effect of going to a full 3D simulation. For this purpose, we ran the same simulation (a fast wind sweeping up its slow predecessor) in 1D, 2D and 3D, which is discussed in Chapter 3. From the results we conclude that it is not immediately necessary to use three dimensional calculations. However, we describe differences between 2D and 3D results, especially as regards the structure of hydrodynamical instabilities.

In Chapters 4 and 5 we describe the evolution of the circumstellar medium around stars of 40 and 60 $M_{\odot}$. From our results we calculate the possible shape of the absorption lines that would be observed in the afterglow of a gamma-ray burst from the central star. From our results in Chapters 4 and 5 we conclude that the blue-shifted absorption lines visible in the afterglow of gamma-ray burst GRB 021004 are most likely caused by material in the circumstellar medium of the progenitor star. The different velocities at which this material moves relative to the star, can be explained by the hydrodynamical

interactions that took place in the circumstellar medium during previous phases of the stellar evolution. The time dependence of the computed column density profile leads us to the conclusion that the progenitor star had only a short Wolf-Rayet period. This is in accordance with current gamma-ray burst models, which predict that the gamma-ray burst progenitor must be spinning rapidly (MacFadyen & Woosley [39]). A long Wolf-Rayet period makes this unlikely, since the star would lose angular momentum, due to the high mass loss rate (Langer [36],Petrovic et al. [53]). The short Wolf-Rayet lifetime may be due to a comparatively low ($\lesssim 30\ M_\odot$) original mass of the star (Schaller et al. [63]), or to binary evolution with mass transfer, which would have stripped the star of much of its outer layers (Petrovic et al. [52]).

We have also explored ways to obtain matter with a constant density close to gamma-ray burst progenitors. Possible explanations include low intensity progenitor winds, high density or temperature in the CSM and the motion of the progenitor star relative to the surrounding medium. Although we can not point at a single explanation that accounts for all instances of this phenomenon, we do believe that we take into consideration the most likely causes in Chapter 6, which together can explain that this occurs so often. Typically, external influences such as the density and pressure of the interstellar medium can not bring the constant density medium close enough to the star. in order to achieve this, we have to assume that the stellar wind is comparatively weak. This leads us the conclusion, that gamma ray bursts, which show a constant density medium in their afterglow most likely had low metallicity progenitor stars.

1.8 What's next?

The work described in this thesis can serve as basis for several new lines of research. Currently, we are working on simulations of the circumstellar medium around rapidly rotating, chemically homogeneously evolving stars (Yoon & Langer [87]), which represent the first realistic gamma-ray burst progenitor evolution models. The rapid rotation of such a star creates an aspherical stellar wind, which in turn creates anisotropies in the circumstellar medium.

Another interesting research topic will be to analyze the chemical composition of the circumstellar bubbles. In our simulations we have treated the gas as chemically homogeneous. However, as the composition of the star changes during the evolution, so does the composition of the stellar wind. By tracking the composition of the material, we could make more accurate predictions about the emission and absorption spectra of the circumstellar medium.

Finally, the advent of better computer codes and more powerful computers allows us to make fully three dimensional simulations of the circumstellar medium. Not only will this enable us to predict the morphology of the CSM with greater accuracy, it will also create the possibility to simulate the evolution of the circumstellar medium around close binaries. Since many stars are part of binaries or even more complex systems, this will be of great importance to our understanding of the evolution of the circumstellar medium.

1.9 Thesis summary

The layout of this thesis is as follows:

1. Chapter 2: The evolution of the CSM around a massive star that ends its life as a Red Supergiant is considered. We describe the results of 1D hydrodynamical simulation of the interstellar medium around a 25 $M_\odot$ star. This simulation includes the effect of the stellar wind as well as that of photo-ionization. We find that during the main sequence this star produces an HII region outside its wind bubble. During the red supergiant phase, the HII region disappears due to a lack of high energy photons from the central star

2. Chapter 3: Differences between 1D, 2D and 3D simulations of circumstellar shells are worked out. We present the results of 1D, 2D and 3D simulations of the same hydrodynamical interaction: the formation of a shell, that is driven by a fast wind and sweeps up a slow wind. From this example we describe the differences in results that occur, in case more dimensions are used for the same numerical simulation. The difference between 1D and 2D results is considerable, since the 2D simulations show instabilities that are suppressed in 1D. A 3D simulation is usually unnecessary, since it follows the same general trend as the 2D simulation. However, it is useful to note the (small) differences and to see how the 2D shape translates into a 3D structure

3. Chapters 4 and 5: The CSM around potential long gamma-ray burst progenitors and the way their surrounding media show up in the absorption spectrum of the gamma-ray burst afterglow is computed. We have made simulations of the circumstellar medium around a 40 $M_\odot$ and a 60 $M_\odot$ star. From the results we calculate the blue-shifted column density profile that would be visible in the spectrum of a supernova or gamma-ray burst at the end of the life of such a star. We find that the time dependent column density features can be used to constrain the progenitor. The presence of intermediate (100..700 km s^{-1}) absorption features in gamma-ray burst GRB 021004 leads us to conclude that the progenitor star had only a short Wolf-Rayet phase. This means it was either a comparatively low mass ($\lesssim 30$ $M_\odot$) star, or part of a binary, which went through a late mass transfer phase.

4. Chapter 6: Possible ways to obtain constant circumstellar medium density profile around observed gamma-ray bursts are explored. A constant density profile close to a star requires a small radius of the wind termination shock. We present numerical simulations of the hydrodynamical interactions of the possible interactions that can lead to this situation. All such probable scenarios require rather extreme conditions, either in the ISM or in the wind parameters. This makes it unlikely, that any single explanation can account for all instances of a constant density medium in a gamma-ray burst afterglow. The large number of possible scenarios, however, can explain why this is such a common occurrence. In all cases, a weak stellar wind is helpful. This means, that these gamma-ray bursts most likely had low metallicity progenitor stars.

2

Wind-Blown Bubbles around Massive Stars. The effects of stellar wind and photo-ionization on the circumstellar Medium

A. J. van Marle, N. Langer and G. García-Segura
*ReMxAC,2004,***22***,136*

Abstract

We simulate the evolution of the circumstellar medium around a massive star. We take the relevant input parameters for our simulation from a stellar evolution calculation: mass loss rate, wind velocity and the number of ionizing photons as a function of time. By pursuing the calculation through the various stages of massive star evolution, using a realistic mass loss history as input, we simulate the creation and evolution of a wind-blown bubble around the star up to the time of the supernova explosion. Unlike most previous work on this subject we include the effects from photo-ionization. From our calculations we can conclude that photo-ionization affects both the size and mass-distribution of the circumstellar bubble during the main sequence and red supergiant stage.

2.1 Introduction

The evolution of the circumstellar medium around a massive star can be divided into three stages, according to the evolution of its central star. A star in the range of 25 $M_\odot$ to 40 $M_\odot$ starts as a main sequence star, develops into a red supergiant and finally, at least for the more massive stars, becomes a Wolf-Rayet star. This means that in the circumstellar medium three interactions take place: First, an interaction between the fast, low density main sequence wind and the interstellar medium; then the slow, high density red supergiant wind hits the bubble created by the main sequence wind. Finally, the massive, high velocity Wolf-Rayet wind sweeps up the remnants of its predecessors. During the main sequence and Wolf-Rayet phases, the star emits a large number of high energy photons. This radiation ionizes the surrounding medium, so rather than expanding into cold gas, the wind encounters an HII region. The interaction between a spherically symmetric wind and the surrounding ambient medium can be approximated by the analytical solution presented by Castor et al. [7] and Weaver et al. [79]. In this model the interaction between wind and interstellar medium (ISM) works as follows:
The outflowing matter encounters an inner shock, where its velocity is reduced to nearly zero. The kinetic energy of the wind becomes thermal energy. This interaction creates a ”hot bubble” of nearly stationary, hot gas. The thermal pressure of the hot bubble drives a shell into the surrounding ISM. Here it is assumed, that the pressure driven shell will be restrained only by the ram pressure created by its own velocity and the density of the surrounding medium.
This assumption is correct if we consider the surrounding medium to be cold. However, if we take photo-ionization into account the situation becomes rather more complicated. First of all, the photo-ionized gas will have a much higher pressure than the cold ISM. Therefore, the HII region will expand, driving a shell into the ISM. Second, the hot-bubble created by the stellar wind will now expand into a hot HII region, which means that the thermal pressure restraining the shell, will no longer be negligeable compared to the ram pressure. A wind-blown bubble expanding into a compact HII region can be observed in NGC 7635. This situation has no analytical solution and must be simulated numerically. A schematic view of the circumstellar medium can be seen in Figure 2.1.

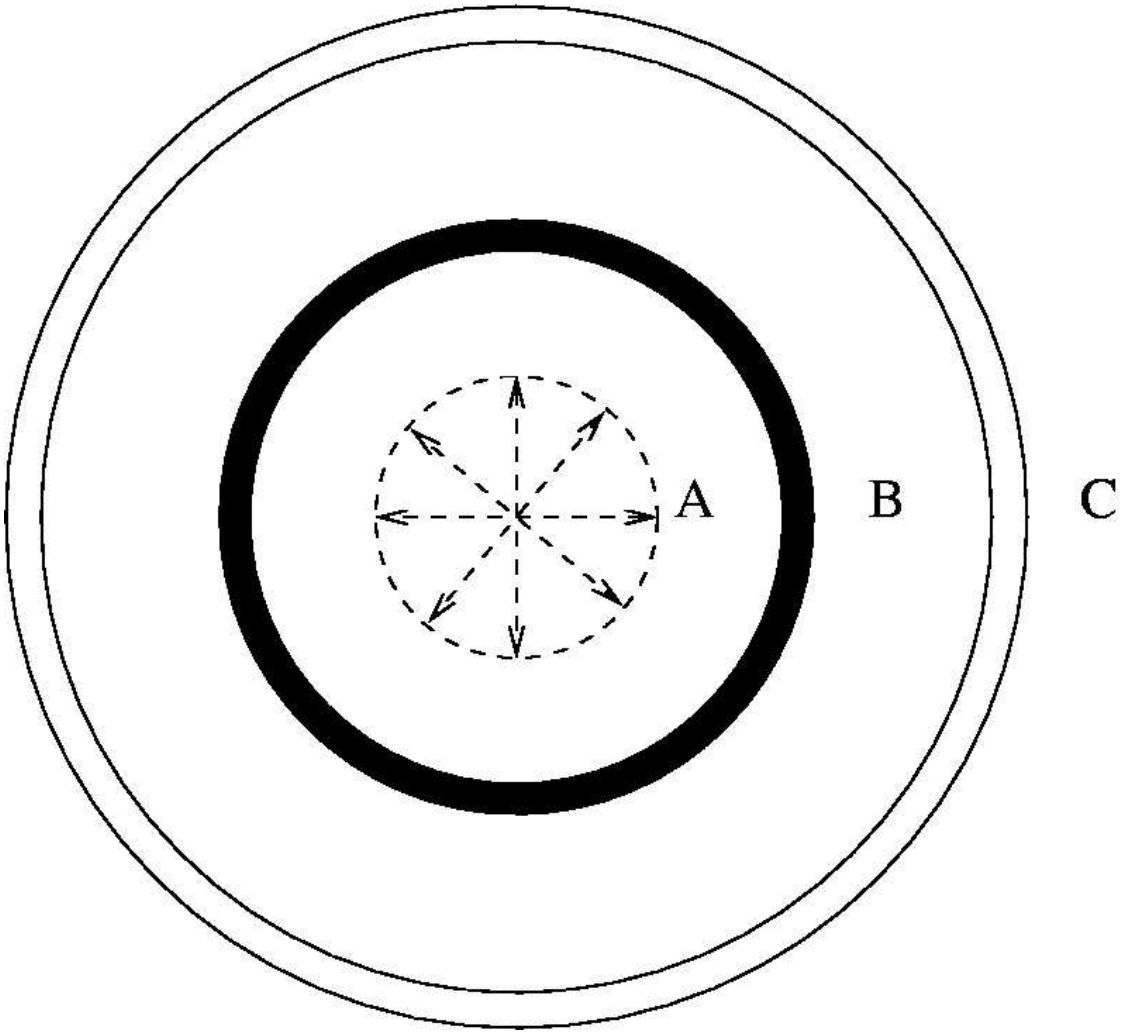

Figure 2.1: Schematic view of the circumstellar medium around a massive star. The wind expands freely until it hits the inner shock (dashed line). Here kinetic energy is converted into thermal energy, heating up the "hot bubble" (A), which pushes a shell (thick line) into the HII region (B). The HII region pushes a shell (double line) into the interstellar medium (C).

2.2 Mass loss history of massive stars

We have used the stellar models presented by Schaller et al. (1992). From these models we constructed a mass loss history for a 25 $M_\odot$ with solar metallicity. The mass loss history consists of a main sequence phase and a red supergiant (RSG) phase. The mass loss rate and the number of ionizing photons can be taken directly from the model. For the wind velocity during the main sequence we used the escape velocity of the star. The velocity of the RSG wind is more difficult to estimate, since the mechanism that drives the wind is not fully understood. The value we used for the velocity is based on observational data and is the same as in García-Segura et al. [25]; hereafter GLM96.: 15 km/s. The wind parameters used in our calculations can be found in Table 2.1. Using these values and the analytical solution referred to in Sect. 2.1 we expect the shell to reach a distance of approx. 26 pc from the star. This number is probably too high since some energy is lost to radiative cooling, but earlier results show that this should not make a difference of

Table 2.1: Mass loss history for a 25 $M_\odot$ star.

Phase	Time [yr]	$\dot{m}$ [$M_\odot$ yr^{-1}]	V [km s^{-1}]	$n_{\rm photon}$ [s^{-1}]
main sequence	0.64215E+07	0.21190E-06	0.88850E+03	0.13740E+49
red supergiant	0.70591E+07	0.12639E-04	0.15000E+02	0.16293E+38

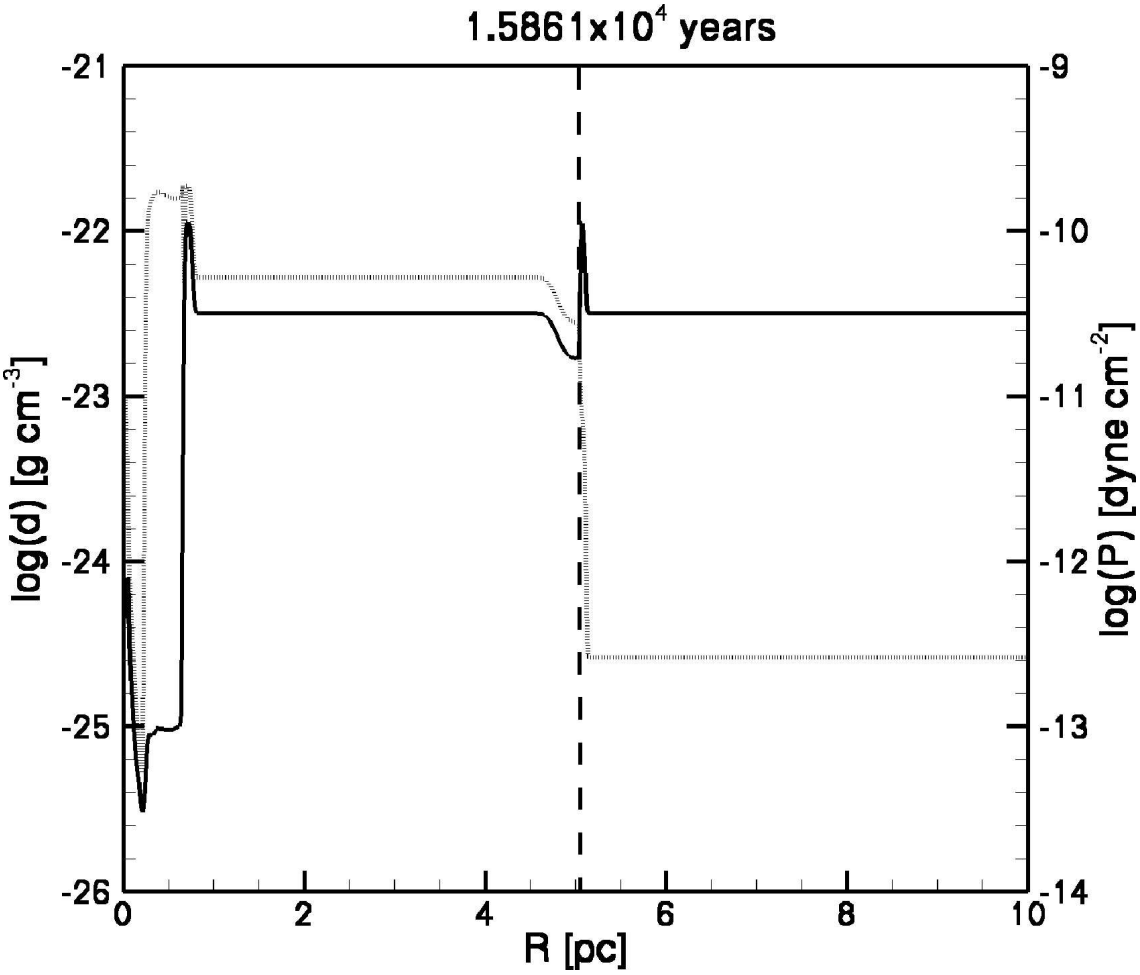

Figure 2.2: The density (continuous line) and pressure (dotted line) in the circumstellar medium around a 25 $M_\odot$ star during the early main sequence stage, as function of the distance from the central star. The dashed line shows the outer edge of the photo-ionized zone. Both the wind driven shell ($r \simeq 1$ pc) and the ionization driven shell ($r \simeq 5$ pc) are visible.

more than ca. 10 percent.

2.3 Method

We have simulated the evolution of the circumstellar medium, using a 1D grid with 3000 gridpoints. The calculations were done with the ZEUS-3D code (See Stone & Norman [67]), which solves the Euler equations on a fixed grid. In order to simulate the wind interactions we have used the method described in GLM96. However, instead of using

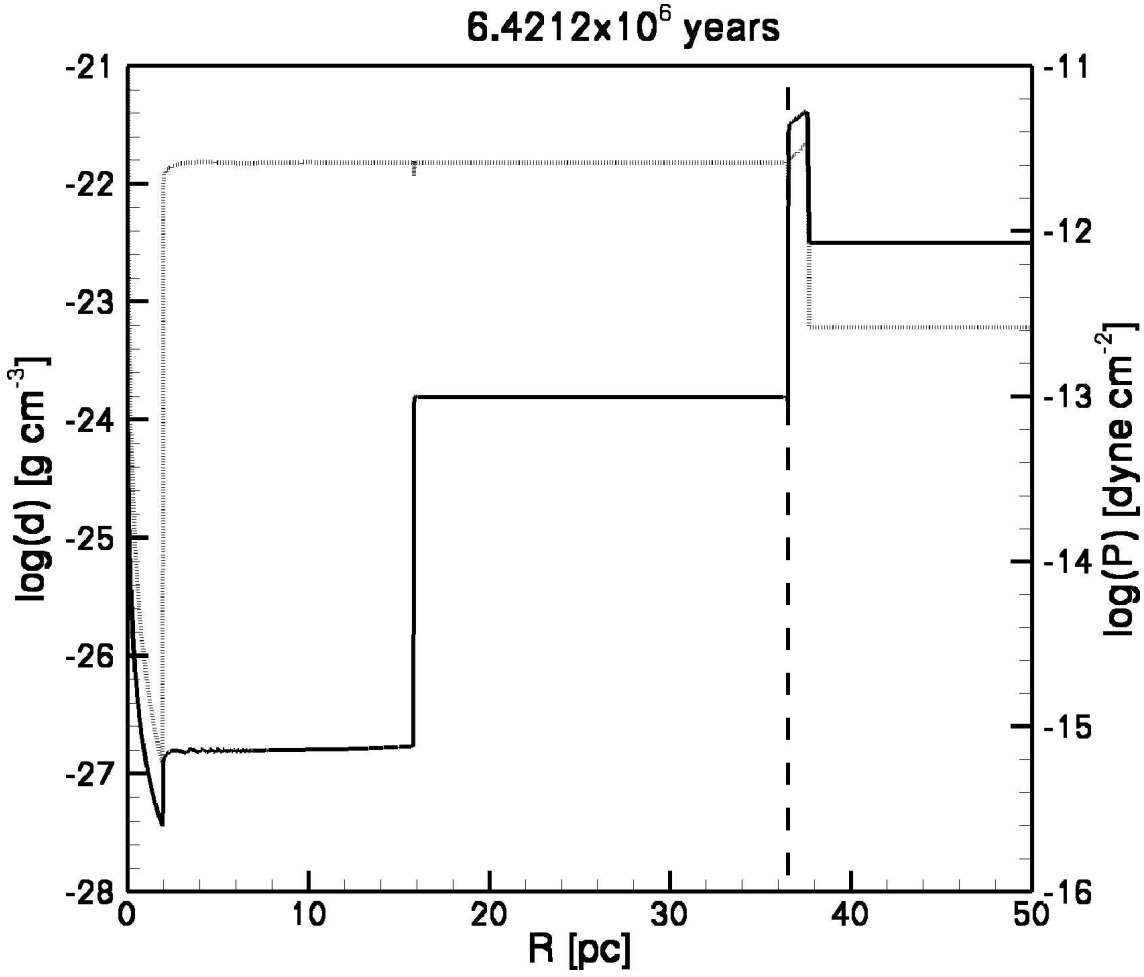

Figure 2.3: The same as Figure 2.2, but at the end of the main sequence stage. Although the inner shell has disappeared, the 'hot-bubble' is still split into two parts: One containing wind material, the other containing ionized ISM.

a time dependent model of the mass loss we assume a two stage model. The values for mass loss rate, wind velocity and photon number as given in Table 2.1 are averages over the main sequence and red supergiant phases.

Photo-ionization was included in the calculations in the following manner. The stellar evolution model provides us with the total number of photons capable of ionizing hydrogen that the star produces. Using this number as a basis, we move outward through the grid, starting at the inner boundary (closest to the star). At each gridpoint we calculate the number of photons necessary to ionize the matter in the local cell and substract that number from the original photon count. As long as we have photons left we can conclude that the matter is ionized, which means that it has a minimum temperature of 10^4 K. Once the number of available photons reaches zero, we stop and define our location in the grid as the Strömgren Radius. All matter outside this radius is considered neutral, all matter inside as fully ionized. This method has been previously described in García-Segura et al. [26].

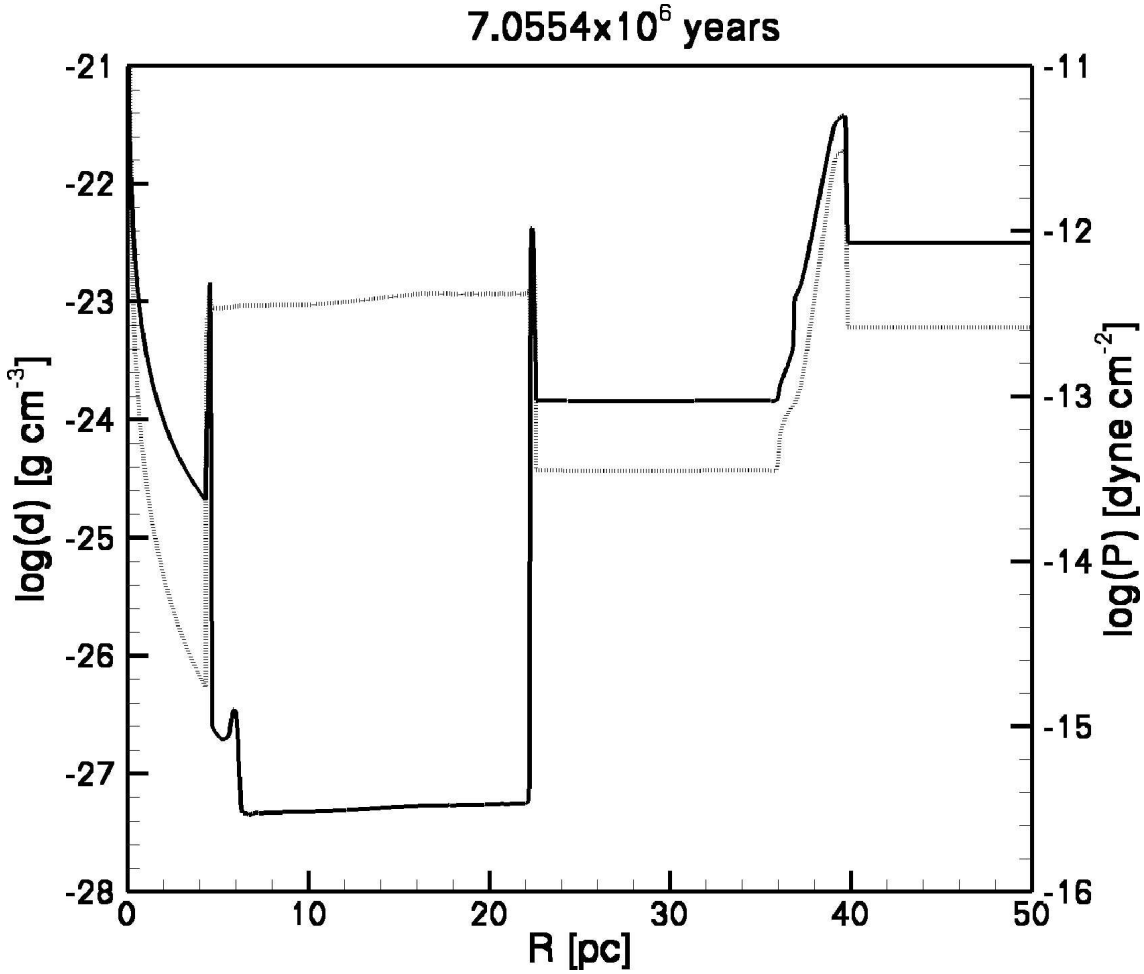

Figure 2.4: The same as Figure 2.3, but at the end of the red supergiant stage. The photo-ionization has disappeared. The outer shell is collapsing inward due to the diminishing pressure. The thermalized main sequence wind drives a new shell into the former HII region, and a third shell is forming where the high density wind reaches the inner shock.

2.4 Evolution of the circumstellar medium

Figures 2.2 to 2.4 illustrate the time evolution of the various structures created in the circumstellar medium. During the main sequence stage, the HII region created by the star is expanding, driving a shell into the interstellar medium ($r \simeq 5$ pc in Fig. 2.2, and $r \simeq 36$ pc in Fig. 2.3). At the inner wind shock ($r \simeq 0.2$ pc in Fig. 2.2), the kinetic energy of the wind is converted into thermal energy, which drives a shell into the HII region ($r \simeq 1$ pc). Figure 3 shows the situation at a later stage. The pressure in the wind bubble and the pressure in the HII region have become equal. As a result, the shell between the two has disappeared, albeit the density discontinuity remains. The outer shell is no longer driven by the photo-ionization, since this driving process stops when pressure equilibrium has been achieved between the HII region and the ISM. This will happen when the HII region has expanded so far that its decrease in density compensates for the higher temperature. The energy needed to drive the outer shell is now provided by the stellar wind.

As the star ages, it becomes a red supergiant with a dense and slow wind. The number

of ionizing photons drops. Therefore, the HII region disappears (see Fig. 2.4). Owing to the low density, recombination will take a long time, but radiative cooling will cause a decrease in thermal pressure. The hot wind-bubble, which keeps its high pressure, expands into the surrounding gas, creating a new shell. A third shell appears close to the star, as the drop in ram pressure from the RSG wind causes the wind bubble to expand inward, sweeping up the wind material.

2.5 Conclusions

The influence of photo-ionization on the evolution of the circumstellar medium can be seen both in the size and the mass-distribution of the circumstellar bubble. At the end of the main sequence phase the nebula has expanded to a radius of 35 pc, rather than 26 pc as predicted by the analytical solution mentioned in Sect. 2.1. This changes as the red supergiant stage begins and the number of ionizing photons decreases. The extent of the wind-blown part of the bubble is only 16 pc at the end of the main sequence phase. The presence of an expanding HII region changes the density structure of the nebula during the main sequence. Our main goal at this time is to simulate the circumstellar environment of stars between 25 $M_\odot$ and 40 $M_\odot$ at the time of the supernova explosion. For those stars that end their lives as Wolf-Rayet stars we intend to provide 2D and 3D simulations of the final phases of the evolution in order to account for the effects of instability in the nebulae around Wolf-Rayet stars.

Acknowledgements

This research was done as part of the AstroHydro3D project.
(http://www.strw.leidenuniv.nl/AstroHydro3D/)
We thank Michael L. Norman and the Laboratory for Computational Astrophysics for the permission to use ZEUS-3D.
This work was sponsored by the Stichting Nationale Computerfaciliteiten (National Computing Facilities Foundation, NCF), with financial support from the Nederlandse Organisatie voor Wetenschappelijk Onderzoek (Netherlands Organization for Scientific Research, NWO).

3

Hydrodynamical simulations of circumstellar shells

A. J. van Marle, N. Langer and G. García-Segura
to be submitted to Astronomy & Astrophysics

Abstract

We perform idealized simulations for the evolution of a shell, driven by a stellar wind into the gas of a previous wind, in 1D, 2D, and 3D, in order to investigate the differences resulting from adding dimensions to the simulation. The difference between 1D and 2D simulations is quite clear, since a 1D simulation can not account for instabilities in the moving shell. From 2D to 3D, we find that the instabilities become more pronounced, and that the density distribution in the shell changes. With increasing time, the 2D model develops characteristics similar to the 3D simulation, rendering it a satisfactory model for describe the bulk properties of the shell. However, it appears if one wishes to investigate the details of the shell morphology a 3D simulation should be required.

3.1 Introduction

The parameters of a stellar wind change repeatedly during the evolution of the star, creating hydrodynamical interactions in the circumstellar medium. For instance when a star moves from the right to the left in the Hertzsprung-Russel diagram, its radius shrinks, causing an increase in escape velocity and therefore an increase in wind velocity. The fast wind will collide with the preceding slow wind, sweeping it up in a moving shell. Such interactions form planetary nebulae (Kwok [34]; García-Segura et al. [26]) and the moving shells around Wolf-Rayet stars (García-Segura et al. [24], [25]; van Marle et al. [73], [74]). To make hydrodynamical simulations of these interactions is a time-consuming effort. Hence, the need to simplify the problem. The most common way to do this is by reducing the number of dimensions in which the calculation is performed, assuming certain symmetries.

Since stars are usually spherically symmetric, it is possible to assume spherical symmetry for the stellar wind as well. Therefore, we can take a spherical grid for our calculations and use only the radial axis. After all, in spherical symmetry it is irrelevant which radial gridline one uses for the computation. (N.B. The influence of stellar rotation and/or strong magnetic fields can destroy the spherical symmetry of the stellar wind, which would make this approach invalid.) While such a one-dimensional simulation gives a good approximations of the interaction, it fails to account for instabilities in the moving shell. A moving shell of this kind is subject to Rayleigh-Taylor instabilities (Young et al. [88]) or "ram-ram" pressure instabilities (García-Segura et al. [25]). These instabilities only occur in a multi-dimensional shell. Since the instabilities can become violent, especially in fast moving shells, it becomes necessary to model the shell in at least two dimensions. For a completely realistic simulation we have to go to three dimensions. However, this also means using a much larger grid, which leads to increased computation time and the need for a larger, more powerful computer, that can handle such grids. Consequently, most simulations done so far have been done only in two dimensions while the third axis (usually the angle in the equatorial plane) is used as the symmetry-axis. In this article, we investigate the limitations of this approach.

Table 3.1: Mass-loss history of a massive star.

	$\dot{M}$ [$M_\odot$ yr^{-1}]	V [km s^{-1}]
slow wind	0.1×10^{-3}	0.1×10^{2}
fast wind	0.3×10^{-4}	0.2×10^{4}

3.2 Numerical method

For our simulations we use the ZEUS 3D code by Stone & Norman [67]. In order to facilitate the three-dimensional simulation we used a version of this code that has been parallelized using MPI routines. We specify a spherical grid with an inner boundary radius of 1.0×10^{-3} pc and an outer boundary radius of 1.25 pc. The grid has 250 radial grid points. For the two-dimensional calculation we add an angular coordinate with a size of 45 degrees and 100 grid points. For the three-dimensional calculation we add a second angle, with the same size and resolution.

The physical parameters for the simulation are given in Table 3.1. The slow wind has the typical characteristics found in a Red Supergiant wind, while the fast wind has the characteristics of a Wolf-Rayet wind. Since Wolf-Rayet stars characteristically have a strong radiation output at high energies, we assume the entire grid to be photo-ionized as soon as the fast wind starts. We treat the gas as pure hydrogen, so in practice this means that the minimum temperature of the grid is set to 10 000 K, while the mean molecular weight per free electron is set to 0.5. Radiative cooling is included in the form of the cooling curve from MacDonald & Bailey [38]. The entire grid is filled with slow wind material conform the parameters in Table 3.1. This means that the velocity is constant throughout the grid, while the density drops with the radius squared. Subsequently we start the simulation by filling the inner five grid points with material from the fast wind (with parameters that conform to the values in Table 3.1).

The collision between slow wind material and fast wind material creates a moving shell, which is driven outward by the thermal pressure in a hot bubble of shocked fast wind material.

3.3 Results

The results of our simulations can be seen in Figs. 3.1 to 3.3. These figures show the morphology of the circumstellar medium at the same moment in time for the 1D, 2D and 3D simulations. The general shape is observed best in the one-dimensional plot (Fig. 3.1). Starting from the inner boundary we first see the free-streaming fast wind, then the bubble of hot shocked fast wind material, then the shell and finally the free-streaming slow wind.

In Fig. 3.2 we see the result of adding a second dimension. The shell is clearly unstable. Moreover, on average the shell has not progressed as far outward. This is caused by energy loss to radiative cooling. Radiative cooling increases with the density squared. This means that the instabilities of the 2D shell make the process more effective, since local density can increase. The three-dimensional simulation (Fig. 3.3) shows the same pattern as the 2D model, but it is much more pronounced. Whereas, in the 2D case, all instabilities tend to be approximately the same size, the 3D simulation shows a clear

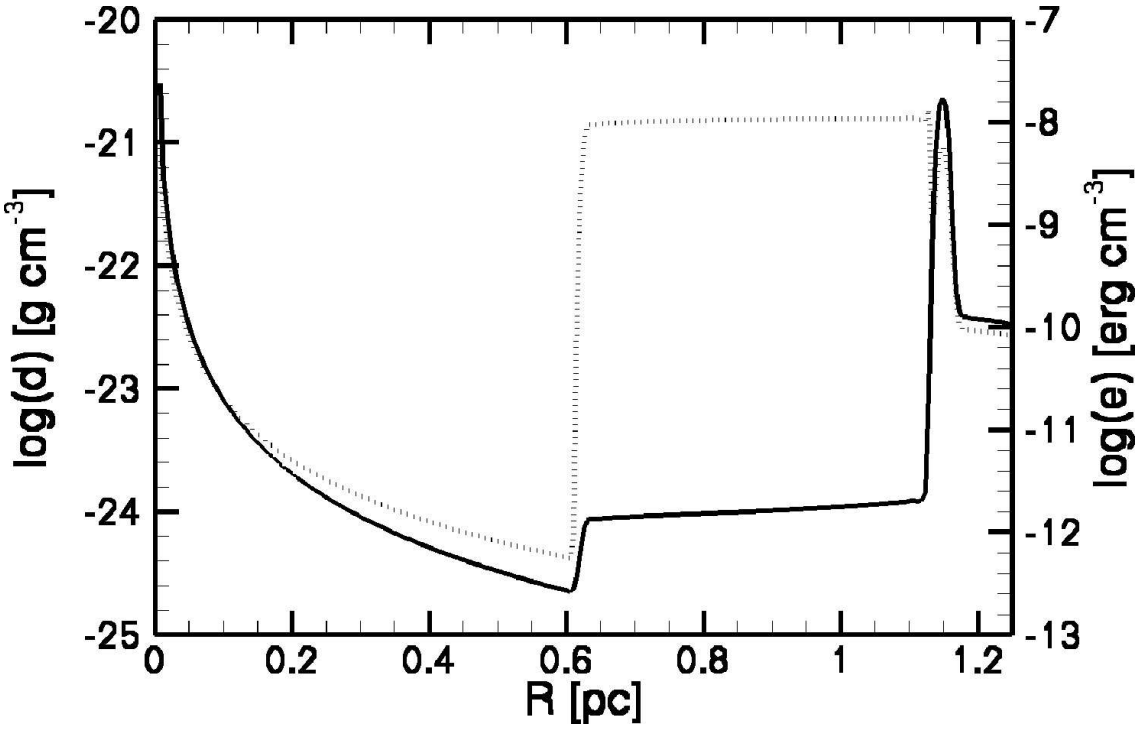

Figure 3.1: Morphology of the circumstellar medium after 7 769 years for the 1D simulation. The mass density (straight line) clearly shows the moving shell at 1.15 pc, while the internal energy density (dotted line) shows the hot bubble (0.6...1.15 pc) that drives the shell outward.

division between a small number of large instabilities and a large number of much smaller instabilities. This is similar to the results obtained by Young et al. [88], who found that 2D Rayleigh-Taylor instabilities are dominated by large structures, while 3D instabilities are much more complex. Figure 3.3 shows an iso-baric surface defined by all the points where the internal energy density is equal to $10^{-9.27}$ erg cm^{-3}. This shows us the inner and outer edge of the hot bubble. The inner edge is, of course, the wind termination shock; the outer edge is the the inner boundary of the moving shell.

Figures 3.4 and 3.5 show the density distribution of matter in the shell. The shells are optically thin and the radiative energy loss increases with the density squared. Therefore, if the shell is observed, the highest density clumps will be visible in emission. These figures show the maximum density along each radial gridline and the position where this maximum density occurs. In the case of the 2D simulation (Fig. 3.4) the density distribution seems to be unrelated to the shape of the shell. The high density area in the center is lagging in radius, but the difference is not very large and the high density and low density areas are similar in size. For the 3D simulation (Fig. 3.4), the highest density clearly occurs in the filaments between the large structures. The differences in the maximum density and the variation in radius where this occurs are more extreme in the 3D simulation. The difference in density in Fig. 3.5 is two orders of magnitude, while it is less than an order of magnitude in Fig. 3.4. The radius at which the density is largest varies over 0.3 pc in the 3D simulation instead of 0.2 pc in the 2D case. This density distribution closely resembles the morphology observed in NGC 6888.

There are several reasons for the difference in density distributions between the 2D and 3D results. First of all, if part of the shell is pushed out further than the rest, the

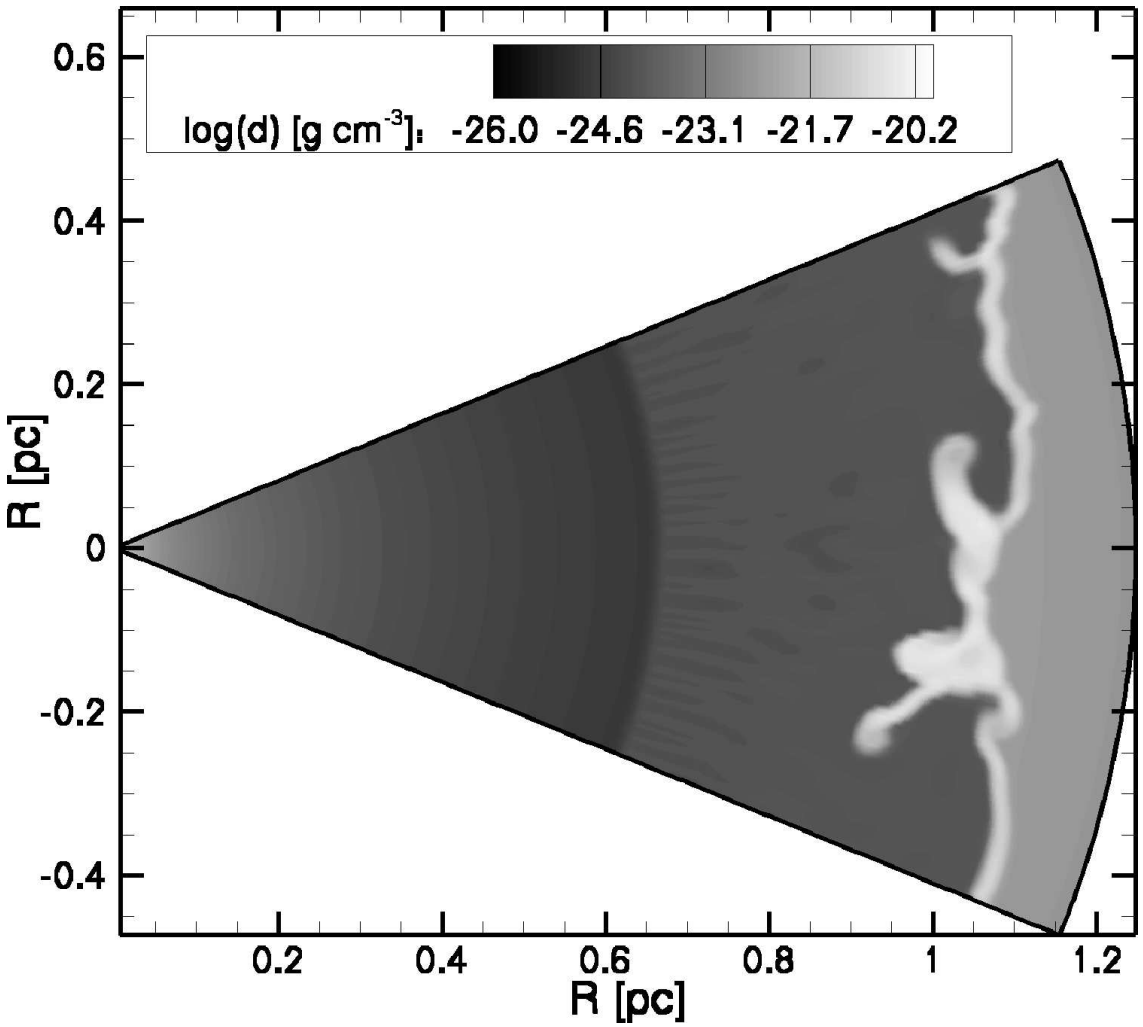

Figure 3.2: Density of the circumstellar medium after 7 769 years for the 2D simulation. The shell shows large instabilities.

local density in the shell will decrease, since the matter has to cover a larger surface. In the 2D simulation, the matter spreads out along a single axis, which means that the density will decrease with the radius of the instability. In the 3D simulation, the matter will spread out over a surface area, which means that the local density will decrease with the square of the radius. Therefore, the larger the instability, the more pronounced the differences in density distribution. These areas become the large 'bulges' in Fig. 3.3. Indeed, if the matter in the local instability decreases, the relative density in the surrounding area increases, which means that these high density regions in the shell will fall further behind, since it is more difficult to push them outward. Since the density differences in the 3D simulation are more pronounced than in the 2D simulation, this effect will be stronger in the 3D case, increasing the density differences even more. Secondly, the increase in density in the filaments between the big 'bulges' makes the matter in those place more difficult to move around, which means that instabilities in the filaments will remain relatively small. Thirdly, the larger differences in density also increase the effect of radiative cooling. The dense clumps will cool more efficiently than the surrounding area, decreasing their internal pressure, so they are compressed further, which increases

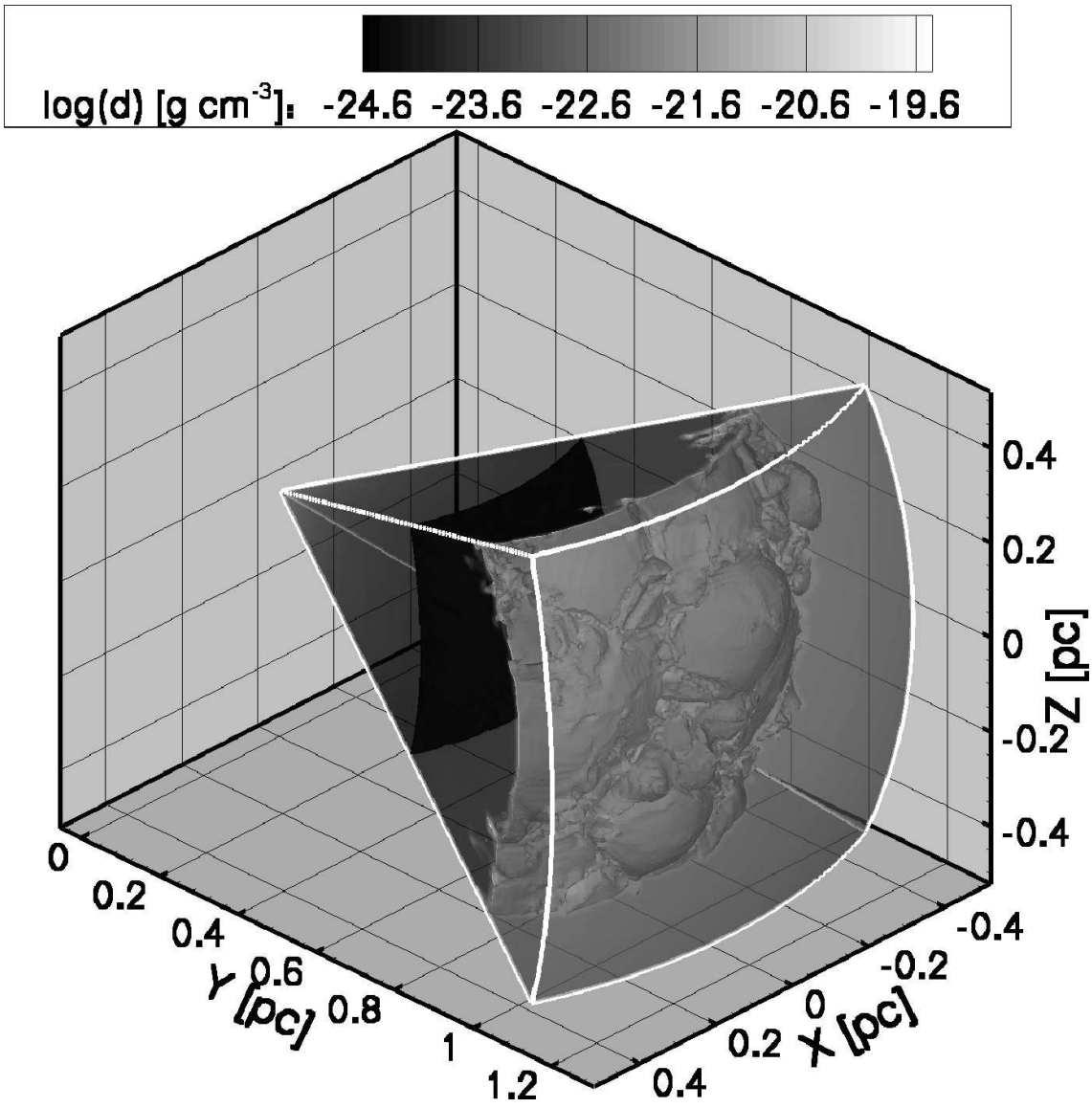

Figure 3.3: Similar to Fig. 3.2, but for the 3D simulation. The instabilities in the shell are even more pronounced and can show clearly filamentary structures. A small number of large structures, where the shell has moved fastest are surrounded by rings of small instabilities that are falling behind. This figure shows the iso-surface were the internal energy of the gas is equal to $10^{-9.27}$ erg cm^{-3}. This gives us the inner and outer boundaries of the hot bubble.

the density even more. Finally, in 2D, any movement along the surface of the shell is only impeded by gas, that lies directly in the line of movement. It is as though a ring of gas, circling the shell, is moving all at once. In the 3D simulation, any gas that lies next to a moving blob of gas has to be dragged along as well, which costs extra energy. Since this effect becomes stronger at higher density, it will decrease the size of the perturbations in the high density filaments. All these effects combine to create the structure observed in Figs. 3.3 and 3.5.

In the 2D simulation, all these effects (with the exception of the last) occur as well, but to a lesser extent. As a result, the formation of the filamentary morphology will be more slowly. In Fig. 3.6 the 2D simulation has been repeated on a larger grid, but with the same

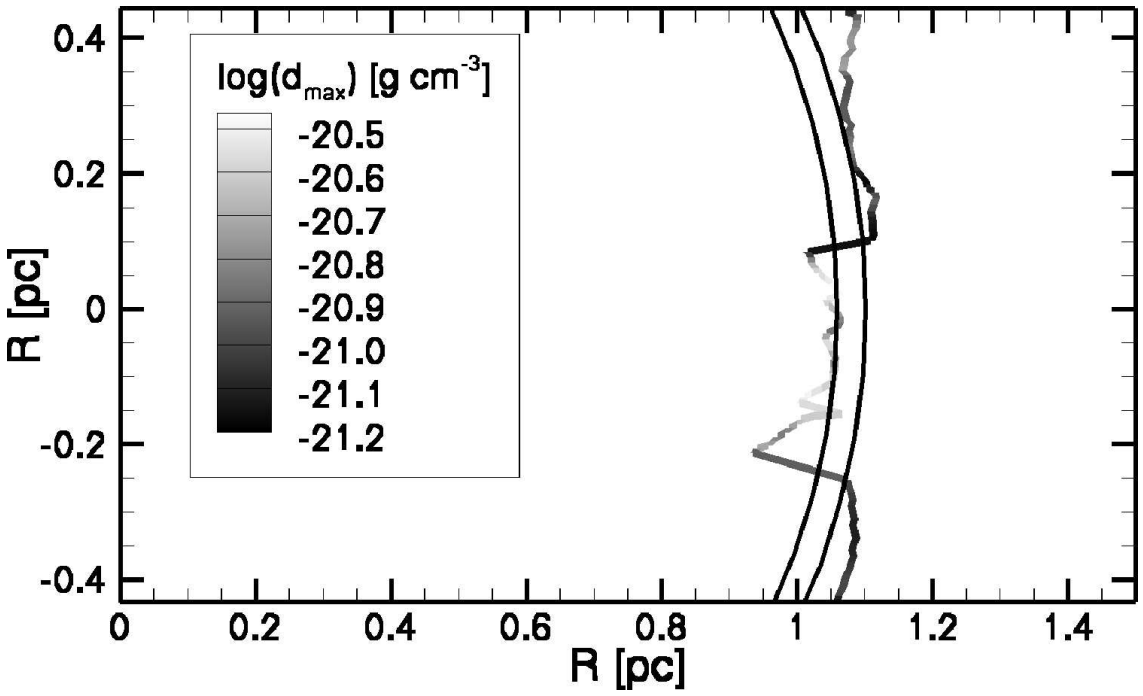

Figure 3.4: The maximum density along each radial grid line and the value of the maximum density for the 2D simulation, at the same moment in time as Fig. 3.2. The distribution of the density in the shell seems to be almost unrelated to the shape. The high density region is falling behind, but the effect is small. High density and low density areas are of the same size. For comparison: the two continuous lines show what a shell with constant radius would look like

resolution, so the shell can be followed for a longer period of time. This figure shows the maximum density along each radial grid line, after 15 538 years. Now the high density regions are falling behind, but the effect is still not as strong as in the 3D simulation. The high density ares are now somewhat smaller than the low density areas, but their sizes are still of the same order of magnitude.

The dense clumps tend to fall behind as the shell moves outward. Since the density contrast is higher for the 3D simulation, this effect is stronger than in the 2D case. However, the difference in velocity between the 2D and 3D simulations is no more than about fifteen percent.

3.4 Conclusions

The difference between the 1D and 2D calculations is considerable, and it is clearly necessary to do 2D simulations in order to achieve a realistic result. The next step, three dimensions, does not change the bulk characteristics and the general evolution of the shell. However, structures inside the shell become more complex and develop more quickly in the 3D simulation, due to changes in the density distribution. Although 2D models may suffice for deriving qualitative conclusions, 3D models are to be preferred if quantitative predictions are involved This is true in particular for studies of shell fragment morphologies.

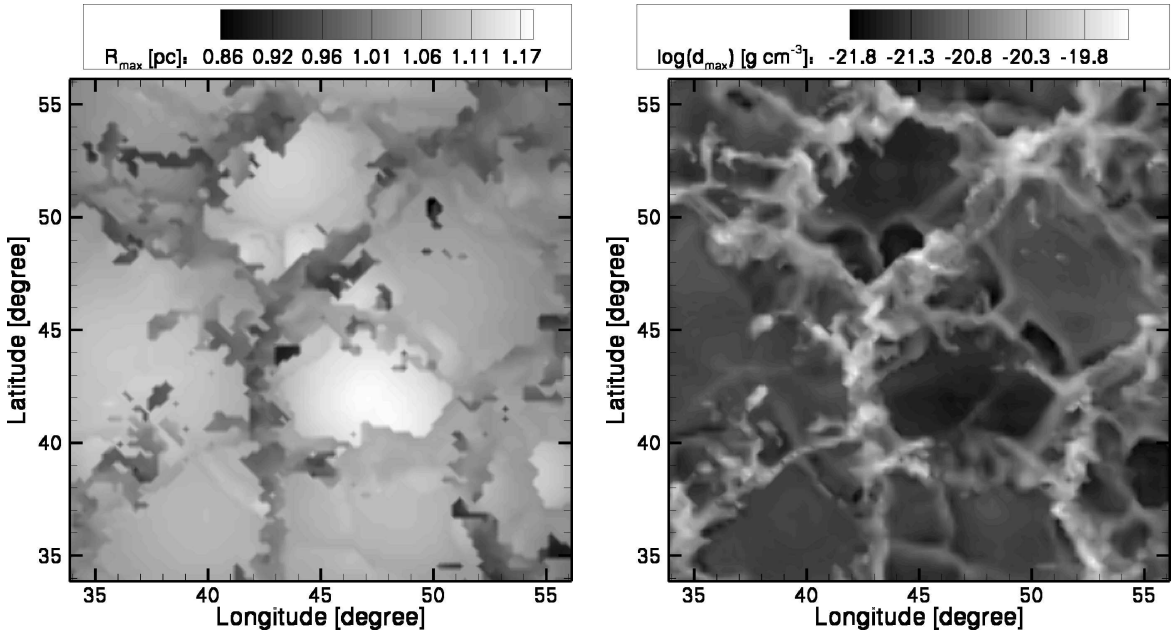

Figure 3.5: The same as Fig. 3.4 for the 3D simulation. The figure on the left shows the radius at which maximum density for each radial grid line occurs. The figure on the left shows the maximum density along each grid line. The structure is clearly filamentary, with the highest density concentrated in thin layers between the large, low density structures.

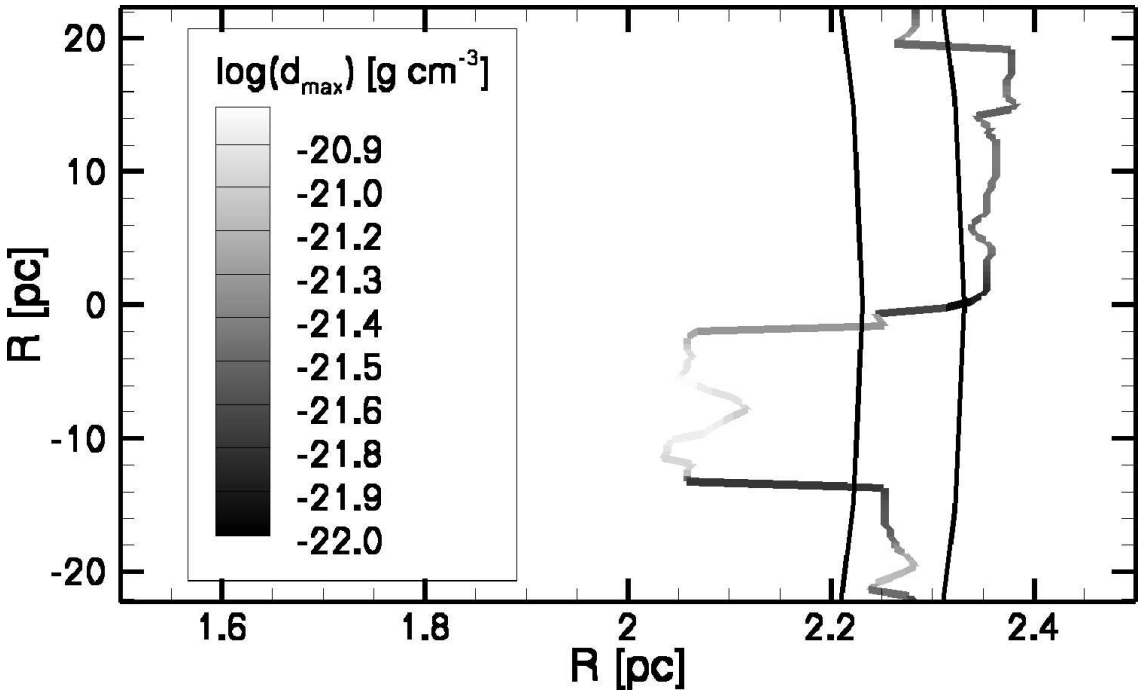

Figure 3.6: The same as in Fig. 3.4, but after twice the time. The high density parts of the shell are beginning to fall behind, though the effect is smaller than in the 3D simulation. High density areas are smaller than low density areas but the difference is not very large. Again the continuous lines show a shell with constant radius.

Acknowledgements

We would like to thank Wim Rijks at SARA Computing and Networking Services (http://www.sara.nl/) for parallelizing the code.
This work was sponsored by the Stichting Nationale Computerfaciliteiten (National Computing Facilities Foundation, NCF), with financial support from the Nederlandse Organisatie voor Wetenschappelijk Onderzoek (Netherlands Organization for Scientific research, NWO). This research was done as part of the AstroHydro3D project:
(http://www.strw.leidenuniv.nl/AstroHydro3D/)

4

Constraints on gamma-ray burst and supernova progenitors through circumstellar absorption lines (I)

A. J. van Marle, N. Langer and G. García-Segura
Astronomy & Astrophyscis, *2005*,**444**,*837*

Abstract

Long gamma-ray bursts are thought to be caused by a subset of exploding Wolf-Rayet stars. We argue that the circumstellar absorption lines in early supernova and in gamma-ray burst afterglow spectra may allow us to determine the main properties of the Wolf-Rayet star progenitors that can produce those two events. To demonstrate this, we first simulate the hydrodynamic evolution of the circumstellar medium around a 40 $M_\odot$ *star from the creation and evolution of a wind-blown, photo-ionized bubble around the star up to the time of the supernova explosion. Knowledge of density, temperature, and radial velocity of the circumstellar matter as function of position and time allows us to compute the column density in the line of sight to the centre of the nebula, as a function of radial velocity, angle, and time. While without radiative transfer modeling and without detailed knowledge of the spatial distribution of chemical elements we cannot produce spectra, our column density profiles indicate the possible number, strengths, widths, and velocities of absorption line components in supernova and gamma-ray burst afterglow spectra. Our example calculation shows four distinct line features during the Wolf-Rayet stage, at about 0, 50, 150-700, and 2200* $\mathrm{km\,s^{-1}}$*, with only those of the lowest and highest velocity present at all times. The 150-700* $\mathrm{km\,s^{-1}}$ *feature decays rapidly as a function of time after the onset of the Wolf-Rayet stage. It consists of a variable number of components, and, especially in its evolved stage, depends strongly on the particular line of sight. A comparison with absorption lines detected in the afterglow of GRB 021004 suggests that the high velocity absorption component in GRB 021004 may be attributed to the free streaming Wolf-Rayet wind, which is consistent with the steep density drop indicated by the afterglow light curve. The presence of the intermediate velocity components implies that the duration of the Wolf-Rayet phase of the progenitor of GRB 021004 was much smaller than the average Wolf-Rayet life time, which strongly constrains its progenitor evolution.*

4.1 Introduction

Planetary nebulae are the result of wind-wind interaction, with a fast wind emitted by a hot post-AGB star sweeping up a previously emitted slow outflow (e.g., Villaver et al. [77]). Stars above $\simeq 25...30\,M_\odot$ also undergo a red-blue evolution in the Hertzsprung-Russell diagram, moving from the red supergiant or Luminous Blue Variable (LBV) stage into the Wolf-Rayet phase (Meynet & Maeder [44]). As (in both cases) dense outflows occur, first at a low and then at a high speed, Wolf-Rayet stars are expected to produce circumstellar nebulae just like post-AGB stars (García-Segura et al. [24] and [25]), which are indeed observable around a large fraction of the Wolf-Rayet stars (Miller & Chu [46]).

Unlike AGB stars, massive stars end their evolution in a violent event triggered by the collapse of the massive iron core in the stellar interior. While it cannot be excluded that some of the Wolf-Rayet stars quietly collapse into a black hole, it is believed today that Type Ib/c supernovae and long gamma-ray bursts are both in fact exploding Wolf-Rayet stars. In Type Ib/c supernovae, photospheric hydrogen appears to be absent, while their location and their late time spectra are consistent with core collapse events (van Dyk [71]; Clocchiatti et al. [11]; Wang et al. [78]). Also hydrogen-rich Wolf-Rayet stars are potential supernova progenitors (Langer [35]).

For gamma-ray bursts, Type Ic supernovae were found to dominate the late afterglow

emission in two cases (Galama et al. [22]; Stanek et al. [64]), consistent with the predictions of the collapsar model for long gamma-ray bursts (Woosley [84]; MacFadyen & Woosley [39]). Rigon et al. [61] argue, based on possible GRB associations with the peculiar Type II supernovae SN 1997cy and SN 1999E, that some hydrogen-rich supernovae may also be related to gamma-ray bursts.

In the supernova and the afterglow cases, the explosion creates a powerful source of UV...IR photons, either in the supernova photosphere or in the interaction of the jet with its surroundings. While in gamma-ray bursts the photons produced by the interaction of the explosively ejected material with the circumstellar matter — e.g., the gamma-ray burst afterglows — probe the innermost parts of the wind bubble (Chevalier et al. [10]), it is the absorption of photons in the line of sight to the central light source which traces the structure of the whole bubble and thus carries the most information about the evolution of the progenitor star.

With the optical and near-infrared spectroscopy of the afterglow of GRB 021004 starting only 0.6 days after the burst, it has become possible for the first time to use absorption line systems to analyze the entire circumstellar bubble surrounding a gamma-ray burst, as proposed by Schaefer et al. [62], Mirabal et al. [47], Fiore et al. [19] and Starling et al. [65]. With continuously refined GRB and afterglow observing techniques, more and better afterglow spectra might soon provide more such cases.

Since Type II and Type Ib/c supernovae also have massive star progenitors, one may also expect narrow circumstellar lines in their spectra. Indeed, Dopita et al. [15] attributed narrow P Cygni profiles seen in Hα and Hδ in the spectrum of the Type IIL SN 1984E to a Wolf-Rayet wind with a velocity of about 3000 km s^{-1}. Bowen at al. [4] and Fassia et al. [18] note the presence of a broad absorption feature at ~ 350 km s^{-1} in the spectrum of the Type IIL SN 1998S, which, as they argue, may be caused by a moving shell. Dedicated searches for circumstellar absorption lines in very early supernova spectra might again provide more and better cases.

It is the main aim of this paper to demonstrate that circumstellar lines in supernovae and GRB afterglows can be used not only to identify the Wolf-Rayet nature of their progenitor stars, but also to strongly constrain some of its main properties. Here, we present a 2D-hydrodynamic model of the evolution of the circumstellar medium surrounding a massive star, improving upon the models produced by García-Segura et al. [24], [25]. Using this model, we then calculate the column density of the circumstellar medium as a function of the radial velocity throughout the evolution, which allows a comparison with observed circumstellar spectral lines.

This article is structured as follows: In Sect. 4.2 we give an overview of the method we use for our numerical simulation of the circumstellar medium. In Sects. 4.3 and 4.4 we present the results of these simulations. In Sects. 4.5 and 4.6 we explain the method to compute the column density as function of radial velocity. Finally, in Sect. 4.7 we discuss the result of our simulations and in Sect. 4.8 we summarize our main conclusions.

4.2 Numerical technique and assumptions

At solar metallicity, stars in the mass range of about 25 $M_\odot$ to 40 $M_\odot$ are thought to develop into red supergiants and thereafter to become Wolf-Rayet stars. This means that three interactions take place in the circumstellar medium (CSM):

Table 4.1: Assumed parameters for the three evolutionary stages of our 40 $M_\odot$ model (Z=0.20).

Phase	End of phase [yr]	$\dot{m}$ [$M_\odot$ yr^{-1}]	v_{wind} [$km\,s^{-1}$]	n_{photon} [s^{-1}]
Main Sequence	4.309×10^{6}	9.1×10^{-7}	890	4.62×10^{47}
Red supergiant	4.508×10^{6}	8.3×10^{-5}	15	3.00×10^{41}
Wolf-Rayet	4.786×10^{6}	4.1×10^{-5}	2160	3.86×10^{47}

1. An interaction between the fast, low density main-sequence wind and the interstellar medium.

2. The slow, high density Red Super Giant wind then hits the hot bubble created by the main-sequence wind.

3. Finally, the massive, high velocity Wolf-Rayet wind sweeps up the previously created structures.

For the hydrodynamical simulations, we used the ZEUS 3D code by Stone and Norman [67]. We simulated the main sequence and early red supergiant (RSG) phase only in 1D. The Wolf-Rayet wind interaction was computed in 2D, so we took the end result of the 1D simulation and map this onto a 2D grid, as described in García-Segura, Langer & Mac-Low [25]. However, since we followed the evolution of the circumstellar medium up to the supernova stage, we calculated the whole circumstellar bubble in 2D, instead of cutting out the inner part. For simplicity, we divided the stellar evolution into three stages: main sequence, red supergiant and Wolf-Rayet. As input model we used the 40 $M_\odot$ star model with metallicity 0.02 as calculated by Schaller et al. [63]. The resulting parameters for the stellar wind and photon emission rate are given in Table 4.1.

Mass-loss rate, wind velocity and the number of ionizing photons were taken as average over these three stages. The mass-loss rate follows directly from the evolutionary model, as does the photon count, for which we used a black body approximation. The wind velocity was chosen so that the kinetic energy output of the star during each stage is reproduced. We chose to use the kinetic energy rather than the momentum, since wind driven shells are energy-driven for most of their existence (Weaver et al. [79]). The density of the interstellar medium was set at $20^{-22.5}$ g cm^{-3}. The effect of photo-ionization was included in the simulation by calculating the Strömgren radius along each radial gridline and correcting the temperature and mean particle weight within this radius as described by García-Segura & Franco [23] and García-Segura et al. [26]. A similar calculation for a 60 $M_\odot$ star was recently performed completely in 2D by Freyer et al. [20].

4.3 The CSM during main sequence and RSG phase

From the beginning of the main sequence, the HII region created by radiation from a massive star pushes a shell into the interstellar gas. This shell consists of neutral hydrogen and is produced by a D-type front; i.e., the gas in the shell enters the ionization front

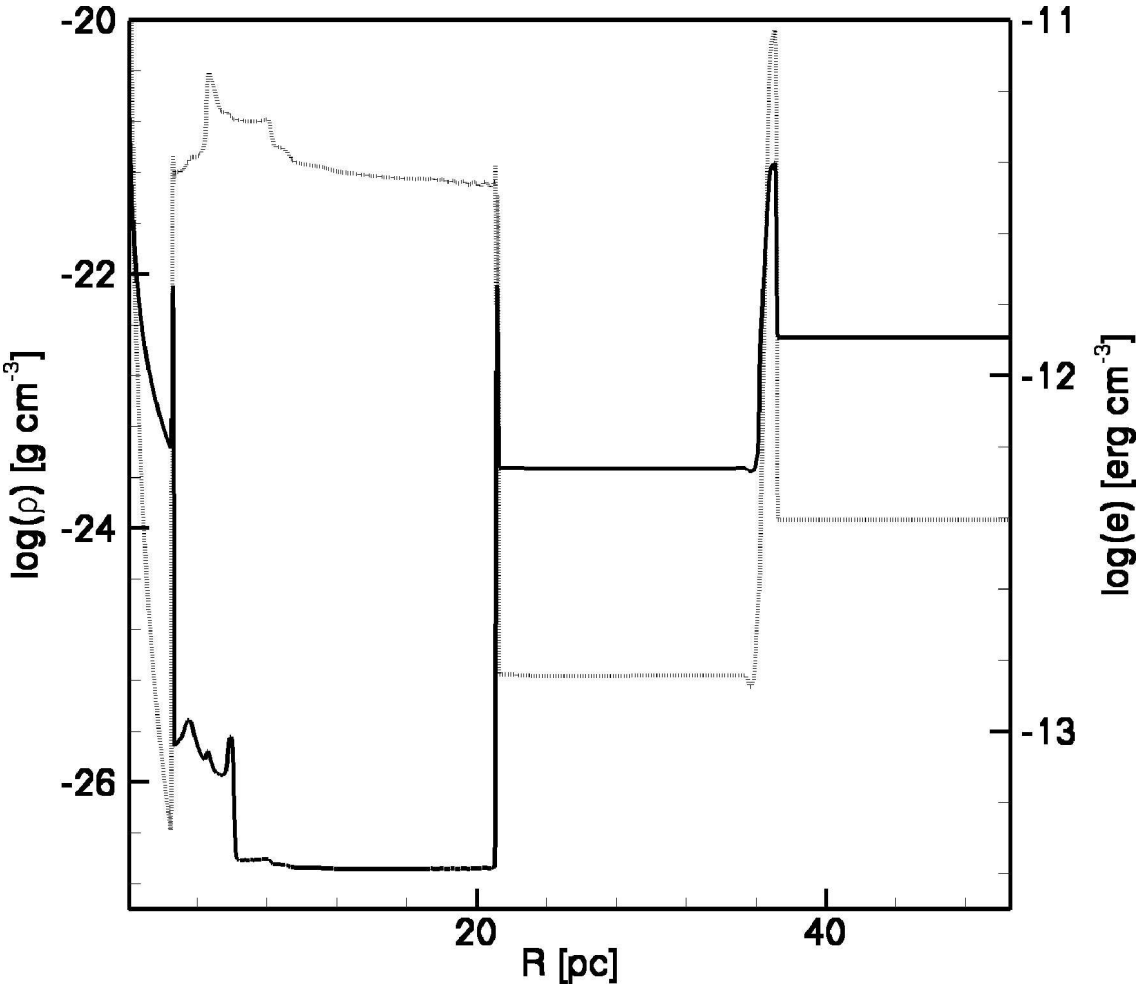

Figure 4.1: Structure of the circumstellar bubble around our 40 $M_\odot$ star at the end of the red supergiant phase. This figure gives mass density (continuous line) and internal energy density (dotted line) as a function of the radius. From left to right we have: the freely expanding RSG wind, the wind termination shock with the thin RSG shell, the hot bubble, the energy driven shell, the former HII region, the 'old' shell (which was driven into the interstellar medium during the main sequence phase and is now dissipating, since the photo-ionization no longer extends beyond the wind bubble), and the interstellar medium.

subsonically. At the same time the kinetic energy of the wind is converted into thermal energy through the collision with the surrounding matter. This creates a hot bubble which pushes a shell into the HII region. Eventually, the HII region and the wind-blown bubble reach pressure equilibrium. Together they drive a shell into the interstellar medium. The shell between the wind-blown bubble and the HII region disappears, though the density discontinuity remains.

This sequence of events depends on the pressure balance between wind-driven bubble and HII region. If the pressure in the wind-driven bubble becomes so high that it drives the shell into the HII region with supersonic speed, then the two regions will not find a pressure balance. In that case the wind-driven shell will sweep up the HII region. The end result will be a single bubble without density discontinuity, driving a shell into the interstellar medium. The density profile will resemble that shown in García-Segura et al. [25], although the photo-ionization will cause instabilities in the shells (García-Segura &

Franco [23] and García-Segura et al. [26]). The deciding factors here are the ram pressure of the stellar wind, the number of ionizing photons, and the density of the interstellar medium, which together determine the thermal pressure in the bubble and the radius of the surrounding HII region. Since the ram pressure of the wind depends on both wind velocity and mass loss rate, which in turn depend on such factors as stellar mass and metallicity, the ram pressure can vary considerably. The same is true for the number of high-energy photons and the density of the interstellar medium. These two factors determine the radius of the HII region. If this radius is large enough, the wind-driven shell will have slowed down to subsonic speeds before it reaches the photo-ionization driven shell. In that case pressure balance will be reached after all, and a bubble with an internal density discontinuity will be created. In this paper we shall continue to use the model with a two-part bubble, in order to show the widest range of possible phenomena in the circumstellar medium.

During the red supergiant (RSG) phase, the number of ionizing photons is low, so the HII region disappears. The wind-blown bubble maintains its high pressure and pushes a new shell into the surrounding medium. A third shell forms at the location of the termination shock due to the lower ram pressure and much higher density of the stellar wind. At the end of the red supergiant phase, the circumstellar medium is built up as follows (see also Fig: 4.1): closest to the star is the freely expanding RSG wind, which ends at about 3 pc in the wind termination shock. The shock itself is marked by a thin shell of shocked RSG wind material. Next comes the hot bubble, which in turn pushes a shell (r $\sim$ 21 pc in Fig. 4.1) into the former HII region. Finally, at about 37 pc, there is the old shell, which was pushed into the interstellar medium during the main sequence phase, but is now slowly dissipating since it is no longer supported by thermal pressure. The velocities of these three shells are low. In fact, the old shell at 37 pc is standing still, since there is no longer any force to drive it outward. The shell at 21 pc moves outward slowly ($v \simeq 10..20\,\mathrm{km\,s^{-1}}$), driven by the thermal pressure in the hot bubble. The movement of the shell at the wind termination shock varies through the RSG phase. During the early part of this phase, the wind termination shock moves inward, due to the decreased ram-pressure of the stellar wind. The shell at the wind termination shock is formed during this phase. The thermal pressure in the hot bubble decreases over time, causing the wind termination shock (and the shell at that location) to move outward with a velocity of about 10 $\mathrm{km\,s^{-1}}$. For stars with a mass of 25 $\mathrm{M_\odot}$ or less, this is the end of the evolution, as was shown in van Marle, et al. [72].

4.4 The CSM during the Wolf-Rayet phase

The period that is of interest to us is the Wolf-Rayet phase, which can be subdivided roughly into three parts, based on the evolution of the circumstellar medium rather than the evolution of the star itself. During the first part (WR1), the ram pressure of the wind rises dramatically as the wind velocity increases (see Table 4.1). This creates a new shell, which moves rapidly through the free-streaming RSG wind and collides with the RSG shell at the wind termination shock (see Sect. 4.3). Both shells are broken up during the collision, and their shattered remains coast into the surrounding bubble. This process was described in great detail by García-Segura et al. [25]. The collision can be seen in Fig. 4.2. The sudden increase in the number of ionizing photons causes most of the former

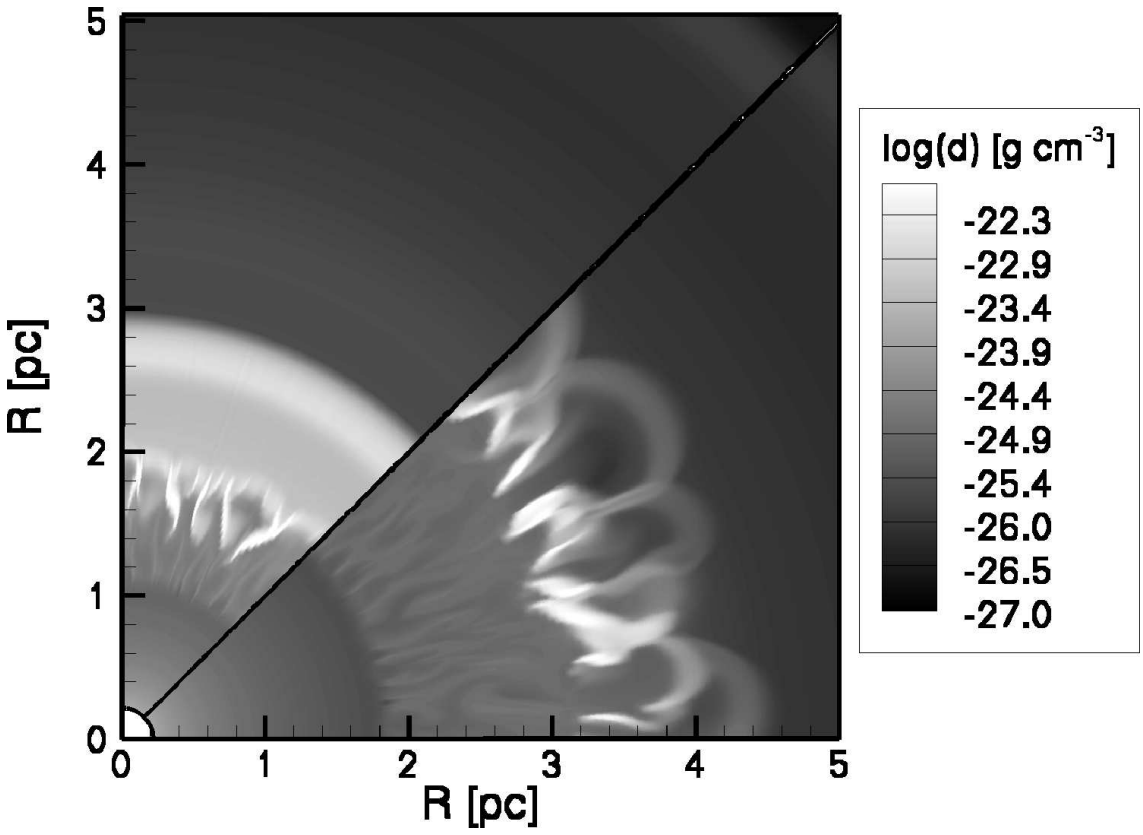

Figure 4.2: The logarithm of the density [g cm^{-3}] of the circumstellar medium close to the star, just before (upper part, t = 4.514 Myr) and just after (lower part, t = 4.522 Myr) the collision between the RSG shell and the Wolf-Rayet shell. As can be seen, the Wolf-Rayet shell is already fragmented due to Rayleigh-Taylor instabilities before the collision. After the collision, the remnants of the two shells move outward together.

HII region (see Fig. 4.1) to re-ionize.

The second part of the Wolf-Rayet phase (WR2) is a period of stabilization. The isobarity of the wind-blown bubble was severely disrupted during WR1, and it takes some time to re-establish a uniform pressure, since the remnants of the collided shells move into the bubble at velocities close to the speed of sound. During WR2 these remnants travel outward into the bubble, where they eventually dissipate. The high density of the Wolf-Rayet wind makes it difficult for the ionizing photons to penetrate deeply into the circumstellar bubble, causing the Strömgren radius to move inward. The Strömgren radius will eventually end up at the same radius as the shell that is still being pushed outward by the wind-blown bubble (see Fig. 4.3 and 4.4). As the kinetic energy of the Wolf-Rayet wind is very high, the thermal energy of the wind-blown bubble will increase, causing the shell that it pushes to accelerate to a velocity of about 50 km s^{-1}.

During the third part of the Wolf-Rayet phase (WR3), there is only one hot bubble maintained by both the stellar wind and the photo-ionization. This bubble pushes a shell into the surrounding medium (the former HII region). Photo-ionization causes the shells to fragment (García-Segura et al. [26]), i.e. the radiation will penetrate through the moving shell at some location and start ionizing the material beyond. The result is an extremely fractured Strömgren radius (see Fig. 4.5). As the pressure in the wind-blown bubble decreases and the moving shell sweeps up more material, it will decelerate. It

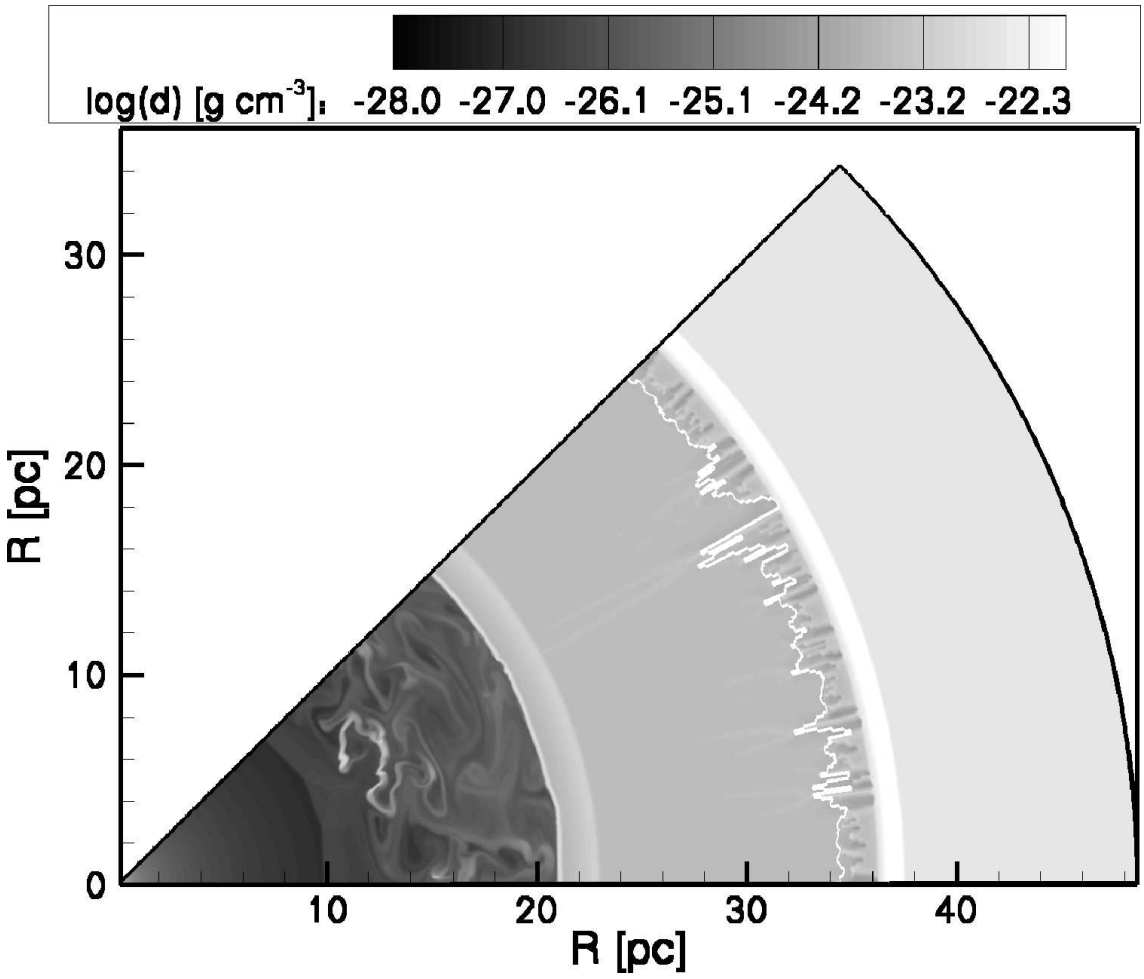

Figure 4.3: Circumstellar bubble around a 40 $M_\odot$ star during the second part of the Wolf-Rayet stage (WR2). This figure shows the density of the circumstellar medium after 4.566 Myr. Moving outward from the star, we have the freely expanding wind, the wind termination shock, the hot bubble, which drives a shell into the surrounding HII region, and finally the old shell. The white line shows the Strömgren radius. The blobs of matter inside the hot bubble are the remnants of the RSG shell and Wolf-Rayet shell after collision (cf. Fig. 4.2). They are dissipating into the surrounding medium.

reaches the original main sequence shell (see Fig. 4.1) almost at the same time as the central star explodes as a supernova. Note that not every Wolf-Rayet star necessarily goes through all three phases. Whether it does depends on the total time the star spends as a Wolf-Rayet star, which varies greatly depending on the metallicity and initial mass of the star.

4.5 CSM column densities

A gamma-ray burst afterglow occurs at a typical radius of 0.01-0.1 pc from the star. This makes it so small, compared to the total size of the circumstellar bubble, that it can be described as a point source in the center of our grid. In order to compare the column densities, we take a single radial line in this grid. Moving outward from the center and at

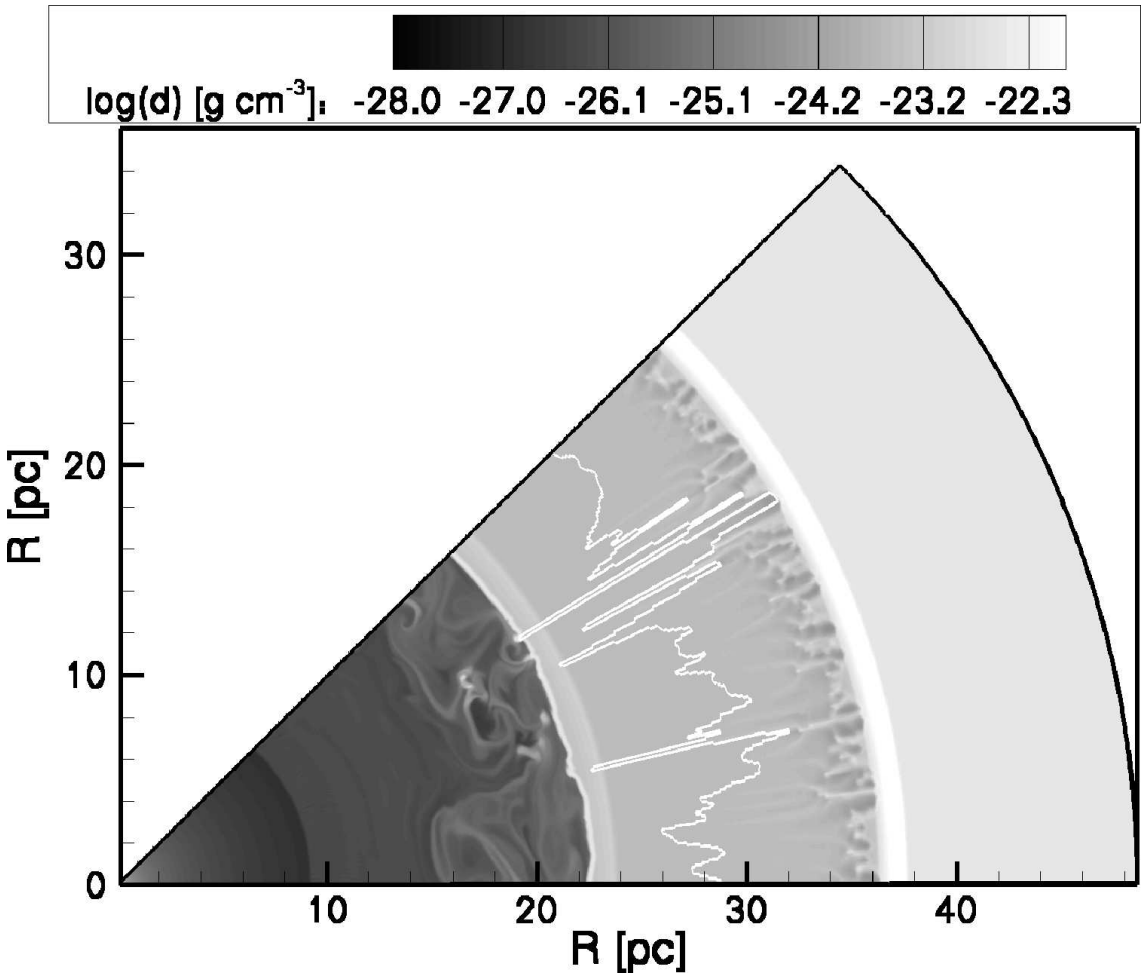

Figure 4.4: Similar to Fig. 4.3, but at at 4.598 Myr. The Strömgren radius is receding as the Wolf-Rayet wind adds more matter to the circumstellar medium.

each grid point, we take the local radial velocity and the column density (density × radial length of the grid cell). This gives us the column density as a function of radial velocity, which is equivalent to the absorption as a function of the blue-shift since the optical depth of the circumstellar bubble is low. Typically, the column density as a function of the velocity will look like Fig. 4.6. Winds give narrow lines, while shells produce a much broader profile. Since the circumstellar medium shows considerable variations, we do this for all radial lines in the grid and take the average, in order to make sure that all possible observable features are accounted for.

Temperatures in the circumstellar medium can rise as high as $T \simeq 10^8$ K. Therefore, it is necessary to spread the column density given in each grid point over a velocity range, dictated by the Maxwell-Boltzmann distribution for the thermal velocity in a single direction:

$$\mathrm{P}(v_\mathrm{r}) = \left(\frac{m}{2\pi kT}\right)^{1/2} e^{-mv_\mathrm{r}^2/2kT}, \tag{4.1}$$

with m the particle mass, k the Boltzmann constant, and T the local temperature. The probability that a particle has a velocity between v_r and $v_\mathrm{r} + \mathrm{d}v_\mathrm{r}$ is given by $\mathrm{P}(v_\mathrm{r})\mathrm{d}v_\mathrm{r}$. In order to calculate the column density as a function of velocity, we first calculate the

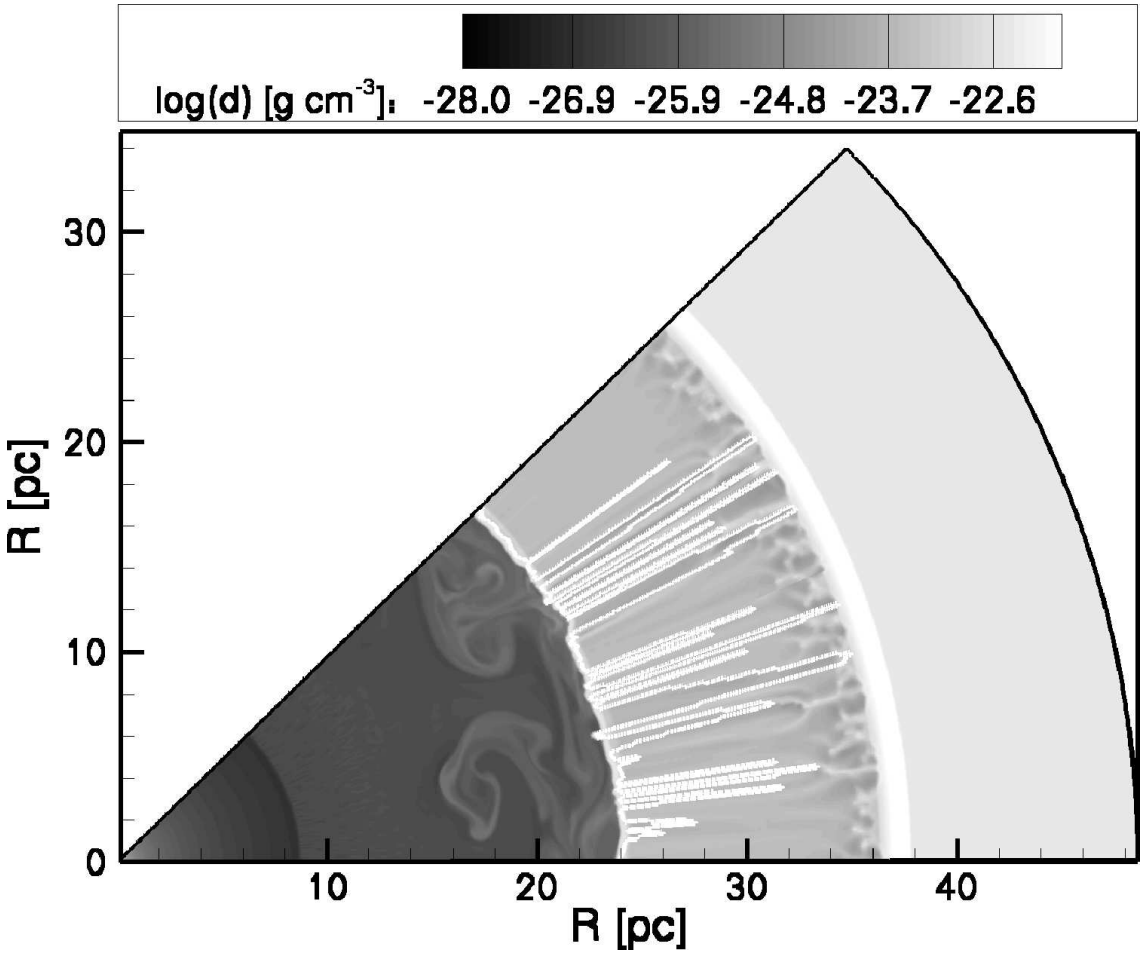

Figure 4.5: Similar to Figs. 4.3 and 4.4, but during the third part of the Wolf-Rayet stage (WR3; t = 4.630 Myr). The Strömgren radius is now at the same distance as the wind driven shell. The remnants of the RSG shell and Wolf-Rayet shell have almost completely disappeared.

Maxwell-Boltzmann distribution for the local temperature. Multiplying the distribution function by the mass density gives us the mass density of particles moving within a certain velocity interval. We use a velocity interval $\Delta v_{\rm r}$ of 1 $\mathrm{km\,s^{-1}}$, so the mass of gas particles with thermal velocities in the interval $\Delta v_{\rm r}$ is:

$$\rho \mathrm{P}(v_r)\Delta v_{\rm r} = \rho\left(\frac{m}{2\pi kT}\right)^{1/2} e^{-m{v_r}^2/2kT}\Delta v_{\rm r}, \tag{4.2}$$

with Δv_r equal to 1 $\mathrm{km\,s^{-1}}$. In the co-moving frame, the result is a Gaussian curve with mean velocity zero; i.e., the amount of gas moving away from us equals the amount of gas moving toward us. We then shift this entire curve until the mean velocity equals the radial velocity of the gas, as found in the hydrodynamical simulation. Multiplying this by the length of a grid cell (dr) gives us the column density of mass in a velocity interval as a function of the velocity for one grid cell. We repeat this process for all the grid cells along a radial line and integrate them for each velocity interval separately. The quantity we end up with is $\mathrm{d_c}(v, \Delta v)$:

$$\mathrm{d_c}(v, \Delta v) = \int_{\mathrm{r=0}}^{\mathrm{r=R}} \rho(\mathrm{r})\mathrm{P}(v_{\rm r})\Delta v_{\rm r}\mathrm{dr}, \tag{4.3}$$

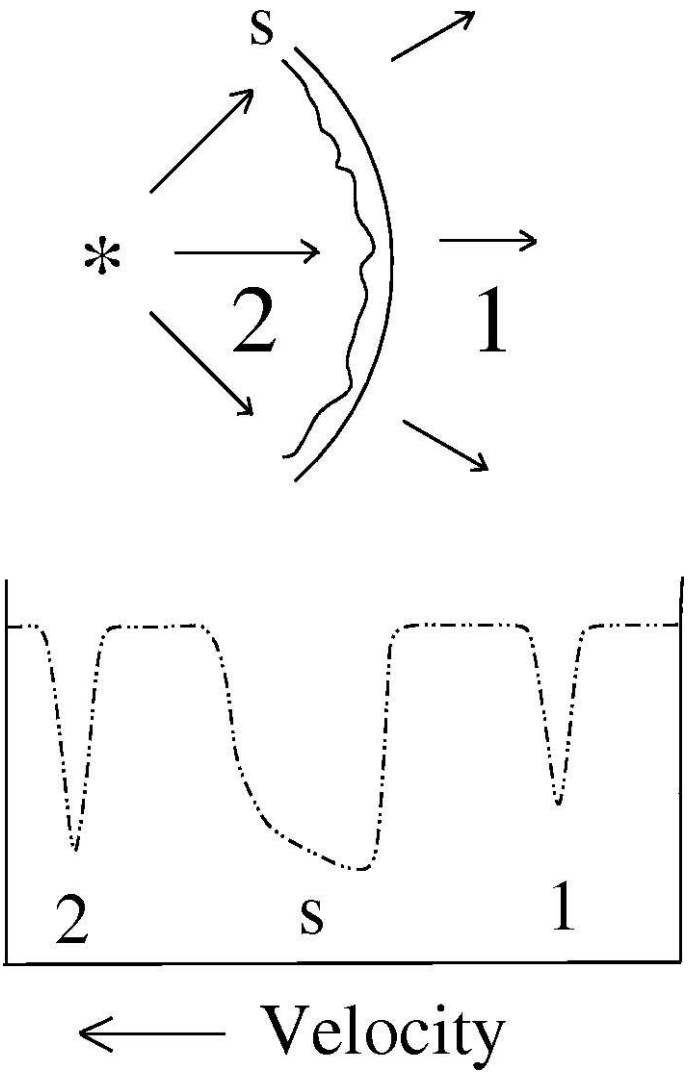

Figure 4.6: Schematically, the column density profile produced by a typical wind-wind interaction. Here, a slow wind (1) is overtaken by a much faster wind (2). If the collision is supersonic, a shell (S) is created. Winds give narrow absorption lines, since all particles have about the same velocity; only thermal broadening may somewhat increase the width of the line. Shells, on the other hand, contain material that is slowing down, so the material will be spread out over a larger velocity range, creating a much broader line. Wind-wind interactions tend to last only a short period of time, but a similar situation occurs when the material in region 1 is stationary.

with R the total radial size of the grid. This is the column density resulting from all particles along a radial line moving with velocities within 0.5 $\mathrm{km\,s^{-1}}$ of v_r.

4.5.1 Angle-averaged column densities

Figure 4.7 shows the angle-averaged CSM column density as function of the radial velocity over the entire Wolf-Rayet period; i.e., in order to ensure that all features are contributing, we repeat the process described above for all 200 radial grid lines and take the average. To obtain the total column density within a given velocity interval, we need to specify the minimum and maximum velocity and then add up the column densities of the

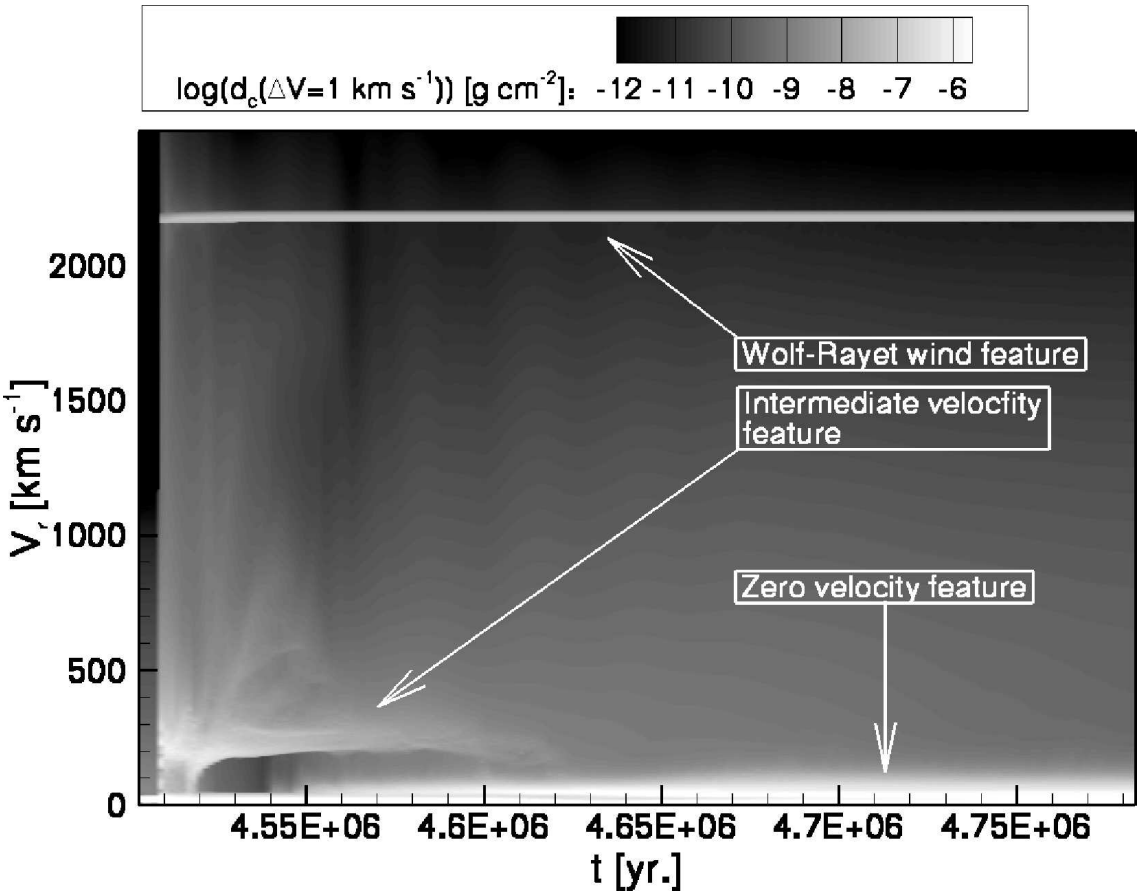

Figure 4.7: Column density $d_c(v, \Delta v)$ with $\Delta v = 1$ km s^{-1} of the circumstellar medium around a Wolf-Rayet star as a function of radial velocity and time, averaged over 200 radial grid lines. On the horizontal axis: the time since the birth of the star in years. On the vertical axis: the radial velocity in km s^{-1}. The plot starts at the end of the red supergiant phase, when there is only matter moving at low velocity. As the Wolf-Rayet phase sets in a narrow feature at the Wolf-Rayet, wind velocity appears as does a much broader feature at intermediate velocity, caused by the collision between Wolf-Rayet and RSG wind. This feature disappears after about 80 000 years, when the remnant of the Wolf-Rayet shell dissipates into the circumstellar bubble. The low velocity line splits at about the same time into two separate lines close together, as the increased thermal pressure of the wind bubble drives a shell into the surrounding medium.

individual 1 kms^{-1} intervals between those two.

The chosen time interval in Fig. 4.7 starts at the end of the red supergiant phase and ends at the pre-supernova stage of the underlying stellar model. While the central star is a red supergiant, there is only one clear line feature, at a radial velocity of nearly zero. There are no high speed features, since the RSG wind, the shells, and the gas in the hot bubble, all move at low velocities. As the Wolf-Rayet wind starts, two new features appear: 1) the Wolf-Rayet wind itself, traveling at about 2200 km s^{-1}, and 2) the region where the Wolf-Rayet wind collides with the much slower RSG wind (i.e. the Wolf-Rayet shell).

During the initial Wolf-Rayet phase (WR1 in Sect. 4.4) three absorption features are produced: the zero velocity feature, which was already visible during the RSG phase, a narrow strong line at high velocity (2200 km s^{-1}) caused by the Wolf-Rayet wind, and

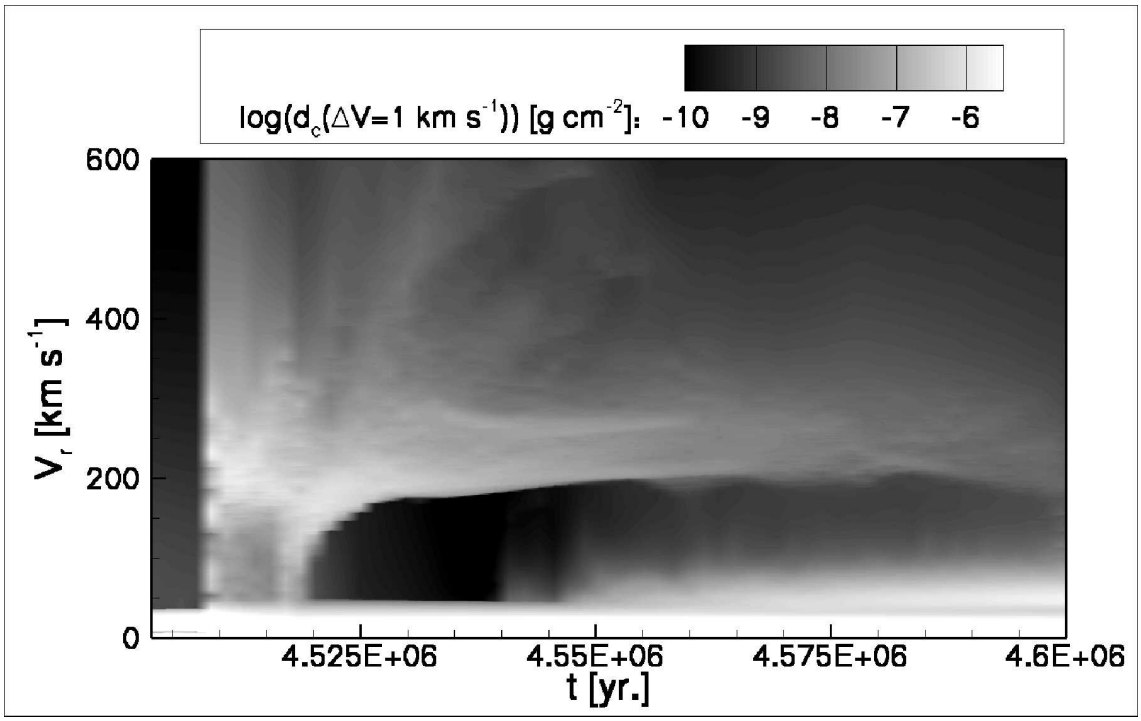

Figure 4.8: Blow-up of the low velocity part of Fig. 4.7 for the period during which the intermediate velocity feature is visible. This feature starts at about 4.508 Myr and is the result of the shell swept up by the Wolf-Rayet wind. Initially, the column density between the zero velocity feature and the intermediate velocity feature is quite high, as slow-moving RSG wind material is swept up by the shell and accelerated. After the collision between the Wolf-Rayet shell and the RSG shell (t = 4.52 Myr), this situation no longer applies. The fragments of the shells no longer sweep up a significant amount of mass. Therefore, no matter is accelerated and the column density between the zero velocity feature and the intermediate velocity feature decreases. The intermediate velocity feature is strongest between 150 and 300 $\mathrm{km\,s^{-1}}$, but fainter components occur at velocities up to 700 $\mathrm{km\,s^{-1}}$. At the end of this period, the zero velocity feature splits up into two separate parts. The new feature, showing material moving at about 50 $\mathrm{km\,s^{-1}}$, is created by the wind-bubble-driven shell, which moves out into the HII region.

a feature at intermediate velocity, which is first produced by the swept-up red supergiant wind shell and later by its collision with the RSG shell (cf. Fig. 2). Initially, the intermediate velocity feature extends over a large velocity range (100...600 $\mathrm{km\,s^{-1}}$). This is due to both the high temperature (which causes the particle velocities to be spread over a large velocity range) and the fact that gas moving at a velocity of 2200 $\mathrm{km\,s^{-1}}$ is slowed down abruptly. However, this feature becomes narrower over time. The bulk material of the shell moves outward at a velocity of about 200 $\mathrm{km\,s^{-1}}$ and eventually hits the RSG shell (see Fig. 4.2). After the shell collision, the largest fragments maintain their original speed, which is between 150 and 300 $\mathrm{km\,s^{-1}}$. In some places shocked Wolf-Rayet wind material breaks through the fragmented shells to form smaller clumps, which can have velocities of up to ca. 700 $\mathrm{km\,s^{-1}}$. This marks the beginning of phase WR2.

During this phase the number of visible features is variable. There is still the intermediate velocity feature caused by the remnants of the RSG and Wolf-Rayet shell. However, since this feature is then caused by shell fragments which cover only a fraction of the possible viewing angles (cf. Figs. 4.4 and 4.5), it may or may not show up in an observation

(see below). As the shell fragments start to dissipate into the surrounding medium, the intermediate velocity feature disappears.

At about the same time, a new feature appears close to the zero velocity line. This feature, which shows a velocity of about 50 $\mathrm{km\,s^{-1}}$, is the result of the wind driven shell which moves outward as the pressure in the wind blown bubble increases (see Sect. 4.4). Since this shell is not fractured, the line will always be present, although it may be difficult to identify due to its proximity to the zero velocity feature.

The period during which the intermediate velocity feature exists and the 50 $\mathrm{km\,s^{-1}}$ feature is formed is shown in Fig. 4.8, which is a magnified part of Fig. 4.7. It shows that the intermediate velocity feature is concentrated between 150 and 300 $\mathrm{km\,s^{-1}}$, with subcomponents of up to ca. 700 $\mathrm{km\,s^{-1}}$ present during the first 40 000 yr of the Wolf-Rayet stage. Figure 4.9 shows vertical cuts of Fig. 4.7 for the times which correspond to the CSM density plots in Figs. 4.3 to 4.5. During the third WR phase, WR3, the 50 $\mathrm{km\,s^{-1}}$ feature disappears as the shell moves further outward, sweeping up material and slowing down. In the end only two lines are visible, one at zero velocity and one at the velocity of the Wolf-Rayet wind.

Any ion which is present throughout the circumstellar medium should show up in a set of absorption features as described here. The relative height of the lines, or depth of the absorption, is more difficult to estimate as it depends on the percentage of the particle density of the gas that the ion takes up, which depends both on the chemical composition of the gas and on the degree of ionization (cf. Sect. 4.7.3).

4.5.2 Line of sight dependence

The inclination of the faster parts in the intermediate velocity feature in Figs. 4.7 and 4.8, resp. — i.e. the fact that these features do not appear as vertical structures, but are somewhat inclined — may lead us to expect multiple absorption components at certain times. However, since the displayed column densities are averaged over all angles, the presence of multiple components of the intermediate velocity feature in the angle-averaged representation does not warrant visibility along a single line of sight (see below). On the other hand, even if the angle-averaged representation does not indicate multiple components for a given time, they might well exist at this time for specific lines of sight. We therefore provide a discussion here of the line of sight dependence of the various features. The zero velocity line, the Wolf-Rayet wind line, and the line caused by the intact shell (at 50 $\mathrm{km\,s^{-1}}$) can be observed independent of the angle.

The intermediate velocity feature caused by the fragmented Wolf-Rayet and RSG shells is only visible if a major fragment is in the line of sight. Its probability is strongly dependent on time, as can be seen in Fig. 4.10. In this figure we have taken the average column density of the gas moving at velocities between 150 and 300 $\mathrm{km\,s^{-1}}$, between 400 and 450 $\mathrm{km\,s^{-1}}$, and between 450 and 600 $\mathrm{km\,s^{-1}}$. The first interval contains most of the shell fragments; the last contains the clumps with moderately high velocity (cf. Fig. 4.8). If both these intervals contain a high column density while the intermediate interval does not, they may show up as separate absorption components in an observed spectrum.

As Fig. 4.10 shows, the intermediate velocity feature is visible at nearly any angle throughout the entire velocity interval before the Wolf-Rayet shell collides with the RSG shell ($t \simeq 4.525 \times 10^6$ years). After the collision, the shell remnants are broken up into independent, confined fragments. During this period the feature can only be observed if

such a fragment happens to be in the line of sight.

The probability of such an occurrence is estimated in Fig. 4.11. This figure shows the percentage of radial gridlines, along which the column density at 200 $\mathrm{km\,s^{-1}}$ is more than five times as high as the column density at 100 $\mathrm{km\,s^{-1}}$. As can be seen, the chance of observing the line is highest before the shell collision; afterwards, it drops rapidly. The increased probability of observing the intermediate velocity feature at about 4.57 million years (Fig. 4.11) is due to dissipation of the shell fragments. These fragments reach the edge of the hot bubble, at which time they are unable to continue their radial movement and start to spread out in an angular direction. However, by then the column density has dropped appreciably, and the velocity tends to zero.

Figure 4.10 clearly shows the complexity of the intermediate velocity feature in the angle and velocity space. While based on a 2D simulation with limited resolution, quantitative statements are difficult, it appears clearly from this figure that may expect to observe multiple velocity components in the interval of 100 to 700 $\mathrm{km\,s^{-1}}$ for certain times and viewing angles. It is obvious that the clumps have considerable angular velocities, which means that they may drift in front of each other during their movements in the hot bubble.

Figure 4.12 shows the column density as a function of the velocity along a single line of sight, at a time shortly after the collision of the WR shell and the RSG shell. Time and angle were chosen from inspection of Fig. 4.10, such that the lower (150...300 $\mathrm{km\,s^{-1}}$) and higher (450...600 $\mathrm{km\,s^{-1}}$) velocity intervals of the intermediate velocity feature are populated, but the middle one (400...450 $\mathrm{km\,s^{-1}}$) is not (pink color in Fig. 4.10). And indeed, Fig. 4.12 suggests that an observer looking at the specified time and angle might see two separate components of the intermediate velocity feature. However, it is also clear from Fig. 4.12 that the number of observed separate components may depend sensitively on the spectral resolution of the observation. It should be emphasized that compared to Figs. 4.7, 4.8, and 4.9, which show averages over all angles, the structure of the intermediate velocity feature is much more complex when viewed along a single line of sight.

4.6 Chemical composition of the CSM

The column densities calculated in Sect. 4.5 are based on the assumption that a given ion is present throughout the circumstellar medium. This, of course, depends on both the chemical composition and the temperature of the material. The composition of the freely expanding Wolf-Rayet wind, which produces the 2200 $\mathrm{km\,s^{-1}}$ feature, changes over time as the star evolves from the WN into the WC phase (Maeder & Meynet [41]). The composition of the wind will depend on the initial metallicity of the Wolf-Rayet star. During the WN phase, the wind will consist mostly of helium with some heavier ions. As the star becomes a WC star, carbon (produced by He burning) appears at the surface, becoming the dominant component of the wind.

The wind blown bubble has a mixed composition, since it contains all the material that the star has ejected during its evolution. The remnants of the RSG and Wolf-Rayet shell, which cause the intermediate velocity line, have the composition of the RSG and early Wolf-Rayet phase, plus some material of the hot bubble that they have swept up as they travel outward. The main source of heavy elements here is the red supergiant wind. The energy0driven shell on the edge of the bubble, the HII region, and the old main sequence shell, all have the composition of the interstellar medium.

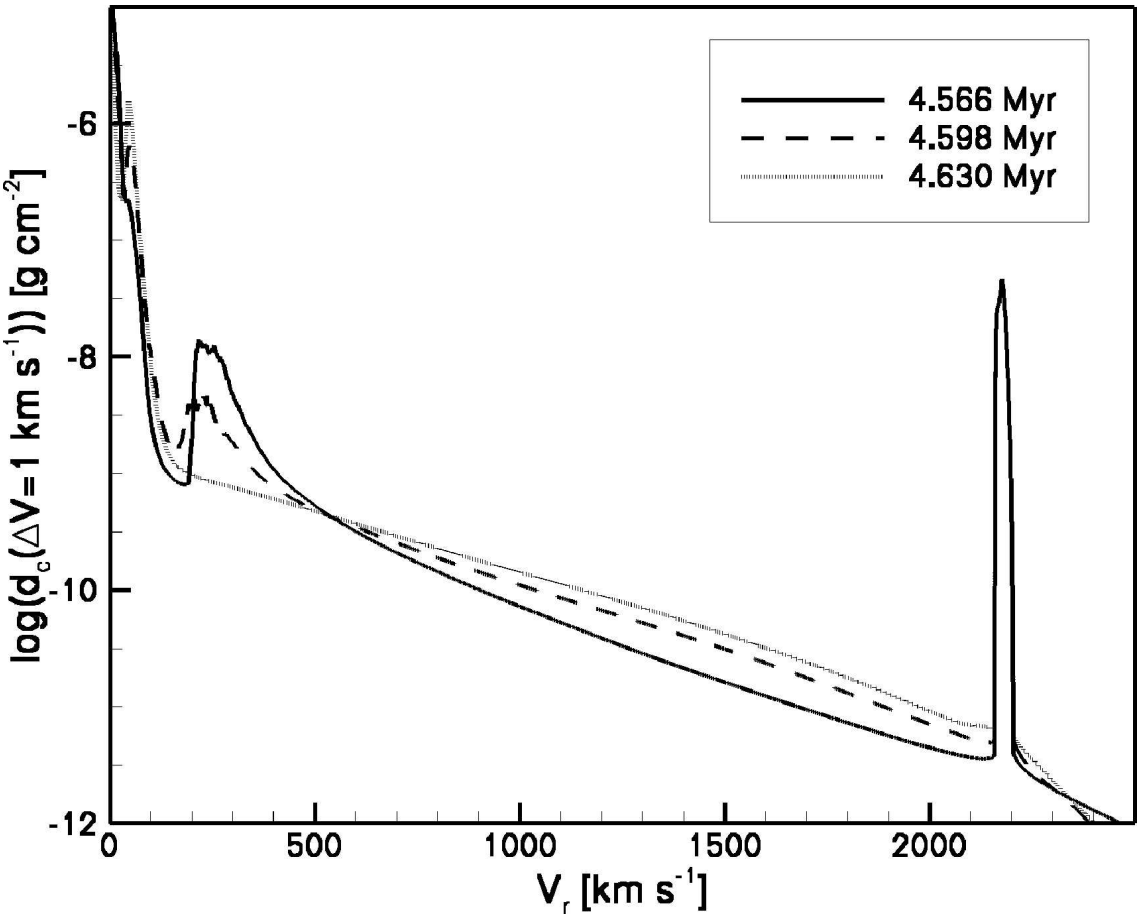

Figure 4.9: Angle-averaged column density per velocity interval $d_c(v, \Delta v)$ with $\Delta v = 1$ km s^{-1} as function of the radial velocity at the same moments in time as the circumstellar medium plots in Figs. 4.3 to 4.5. The formation of the 50 km s^{-1} line can be observed, as well as the disappearance of the intermediate velocity feature (cf. also Fig. 4.7).

The degree of ionization of the circumstellar gas depends on both temperature and photo-ionization. Ignoring photo-ionization, the temperature of the Wolf-Rayet wind would be comparatively low. The wind leaves the star with a temperature of about 10^5 K but would cool down rapidly. Ionization in this region comes from the radiation of the star. The temperature of wind-blown bubbles depends on the kinetic energy of the wind and density of the medium into which the bubble expands. Before the Wolf-Rayet shell collides with the RSG shell, temperatures in the bubble that drives the Wolf-Rayet shell can rise as high as 10^8 K. After the collision, the remnants move into the bubble created by the main sequence wind, where temperatures are lower. As the bubble becomes isobaric, the temperatures in the high density areas will be lower, but the temperature of the bubble as a whole increases due to the high kinetic energy of the Wolf-Rayet wind. Throughout the bubble, temperatures between 10^5 K and 10^7 K can be found. The energy-driven shell and the region beyond form an HII region, which has a temperature of about 10^4 K. The old shell and the interstellar medium are cold. This is the situation before the central star collapses. However, we should keep in mind that the emission from the gamma-ray burst afterglow passes through a medium through which the high energy photons of the gamma-ray burst itself have already passed, which is not taken into account in our model.

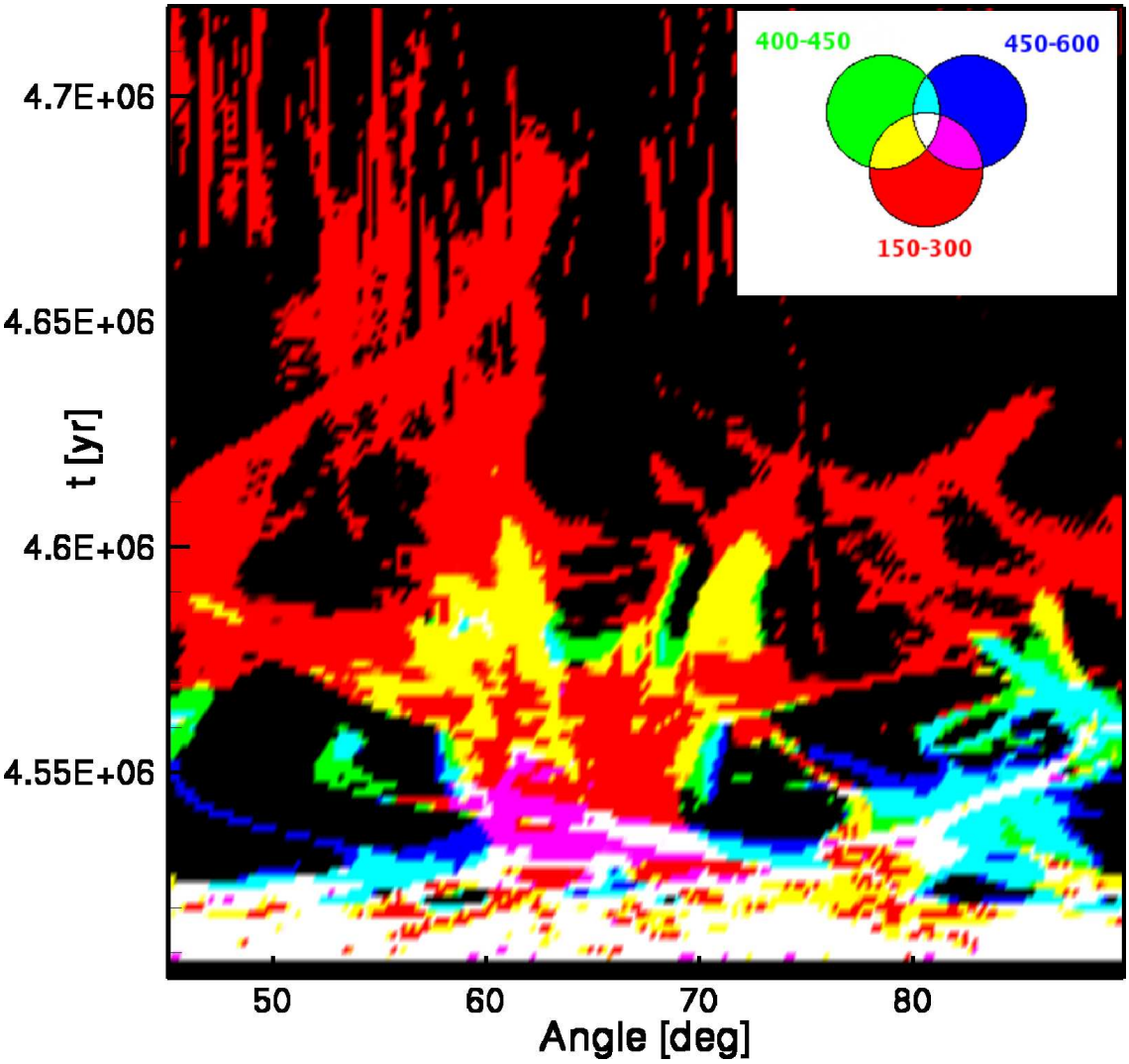

Figure 4.10: The presence of gas with a radial column density above a threshold value (10^{-9} g cm^{-2}) moving in three velocity intervals, as a function of angle and time. The angle is measured from the pole down, so an angle of 90 degrees is equivalent to the equatorial plane. Red color indicates the presence of gas in the 150-300 km s^{-1} interval, while green and blue indicate the same for the 400-450 km s^{-1} and 450-600 km s^{-1} intervals, respectively. Mixed colors indicate that more than one interval has a high enough column density; e.g., white indicates the presence of gas with high enough column density in all three intervals. Pink areas are of particular interest, as these indicate a high column density in both the 150-300 km s^{-1} and the 450-600 km s^{-1} intervals, whereas the 400-450 km s^{-1} interval has a low column density. This means that the intermediate velocity feature will show two well-separated components (see also Fig. 4.12).

4.7 Implications for GRB afterglow spectra

Figures 4.7 to 4.11 show that circumstellar absorption features, to be expected in a gamma-ray burst afterglow spectrum, strongly depend on the duration of the Wolf-Rayet phase of the progenitor star. This may enable us to draw several conclusions regarding a gamma-ray burst progenitor and its surrounding medium.

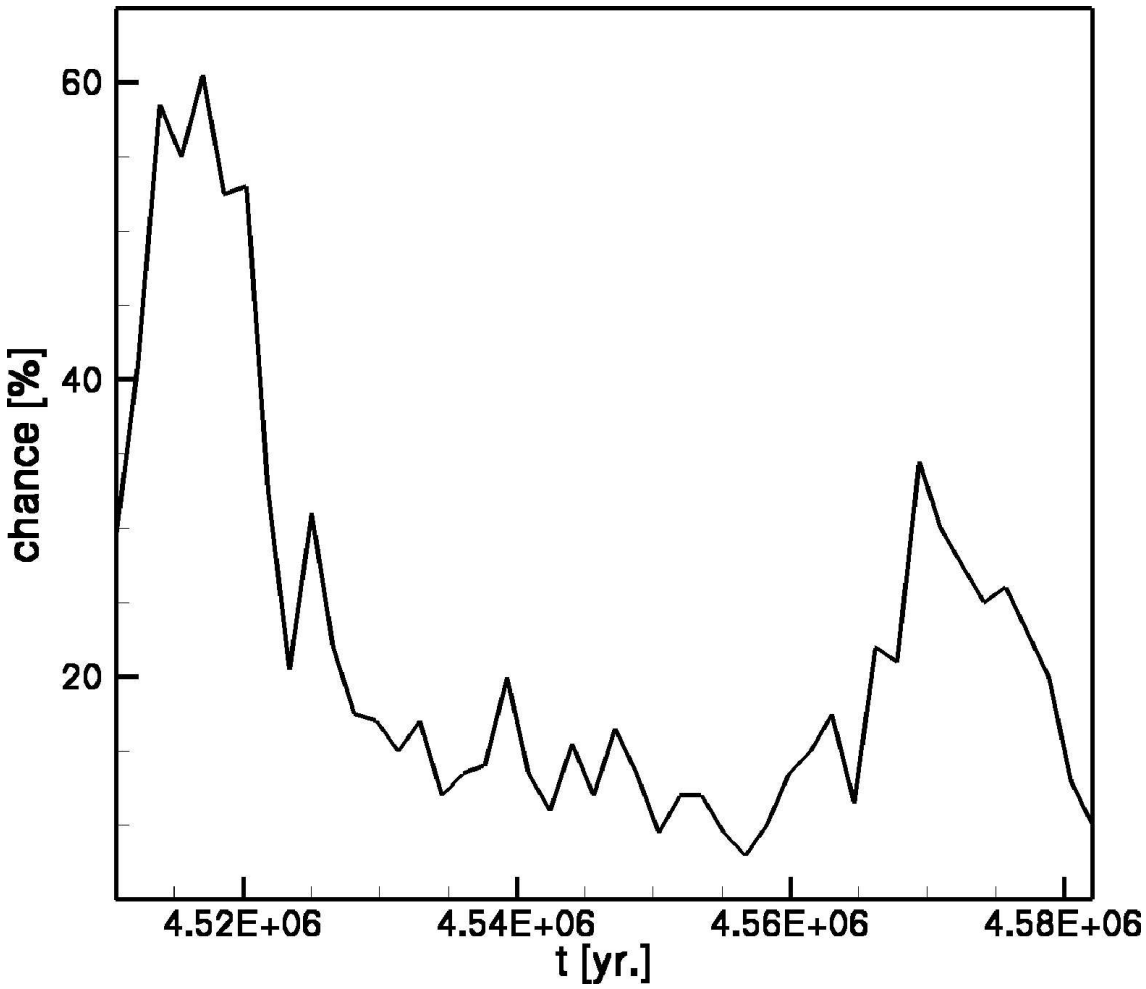

Figure 4.11: The probability of observing the intermediate velocity feature as function of time. To estimate this probability, we have taken the 2D results during the early Wolf-Rayet phase (WR1 and the first half of WR2) and checked along each radial gridline whether the intermediate velocity line would be visible. The criterion for this was a five-fold increase in the column density between the velocity interval around 100 $\mathrm{km\,s^{-1}}$ and the velocity interval around 200 $\mathrm{km\,s^{-1}}$.

4.7.1 The progenitor star

Absorption lines at zero velocity and at the Wolf-Rayet wind velocity might be observed throughout the Wolf-Rayet phase. However, the absorption line at intermediate velocity is only visible for a short period of time (approx. 80 000 yr). The exact speed at which this line appears depends on the relative mass-loss rates and wind velocities during the Wolf-Rayet phase and the preceding stage. This line, caused by the Wolf-Rayet wind-driven shell, reaches its final velocity while the shell is expanding into the freely expanding RSG wind. After it hits the RSG shell at the wind termination shock, the high thermal pressure in the hot bubble may slow down the shell fragments, although this does not happen with this particular model.

It is possible to use an analytical estimate of the shell velocity during its earlier phase, in order to find the velocity at which the absorption line will appear. The velocity of an energy-driven shell, expanding into a previously emitted stellar wind, is given by Kwok

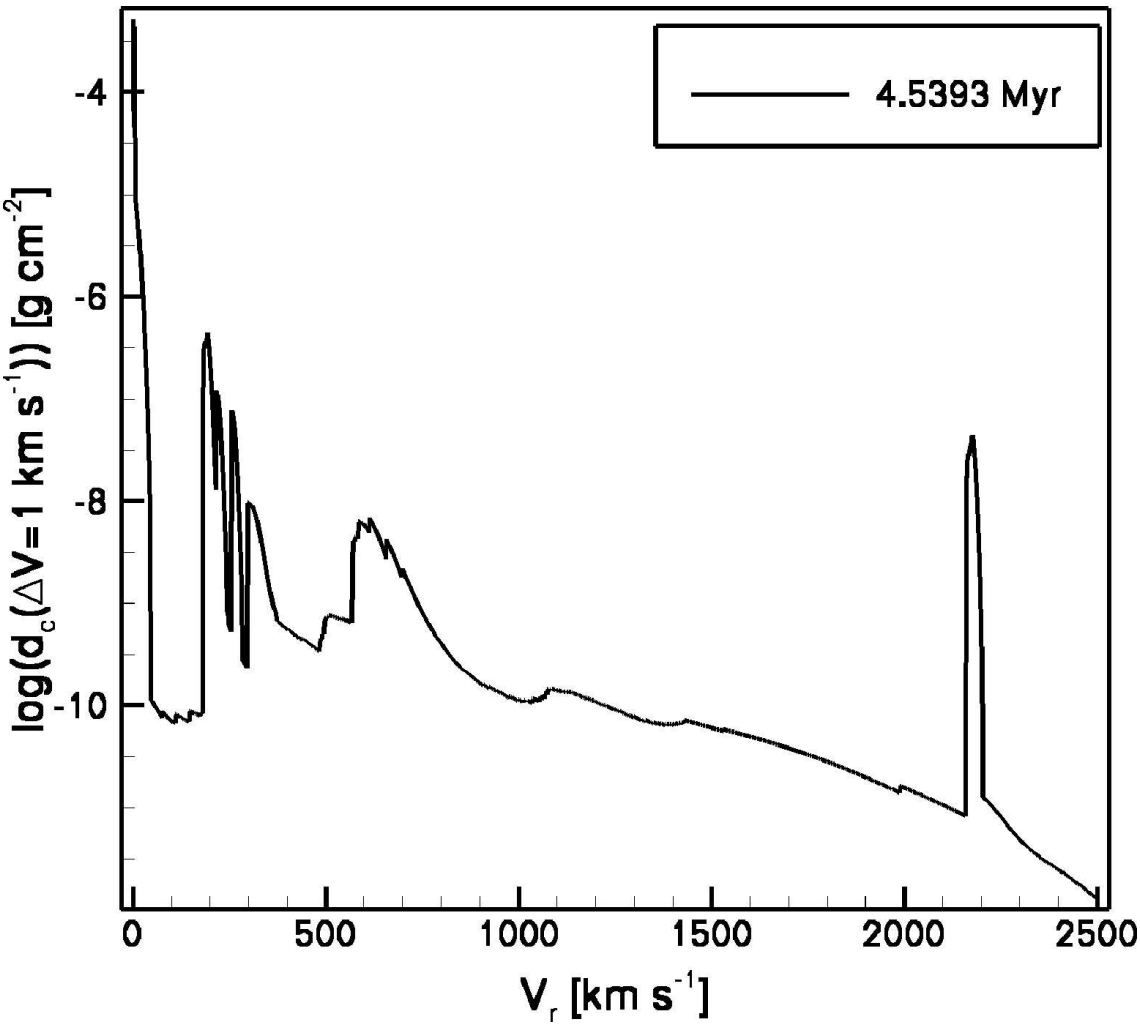

Figure 4.12: Column density along a single line of sight, i.e. $d_c(v, \Delta v)$ with $\Delta v = 1$ km s^{-1} for an angle of 61^o at time t = 4.5393 Myr. Angle and time were chosen from Fig. 4.10 so that two well-separated components of the intermediate velocity feature are present.

(citeKwok as:

$$V_s = \left(\frac{\dot{m}_2 V_2^2 V_1}{3\dot{m}_1}\right)^{1/3}, \tag{4.4}$$

with V_s the velocity of the shell, V_1 and $\dot{m}_1$ the velocity and mass-loss rate of the old wind, and V_2 and $\dot{m}_2$ the velocity and mass-loss rate of the new wind. With typical velocities and mass-loss rates for RSG and Wolf-Rayet winds, this yields a shell velocity on the order of 200 km s^{-1}, which is indeed what we found. However, both wind velocity and mass-loss rate depend on the metallicity and the initial mass of the star, and they can vary even for one star, if the stellar wind is not spherically symmetric. Since rapidly rotating stars have aspherical wind distributions and gamma-ray burst progenitors are thought to be rapidly rotating stars, this is a sensible scenario. For heavier stars, which pass through a Luminous Blue Variable stage rather than a red supergiant stage, the values would be different as well (García-Segura et al. [24]). Whether the line will be visible at all depends, of course, on the exact moment at which the star collapses. If the line is visible, it would indicate a short Wolf-Rayet phase, i.e. no more than about 50 000 to 80 000 years.

It is also possible that the freely expanding wind area around the star is much larger. Possible explanations for this would be a low density interstellar medium, or a lower mass-loss rate during the main sequence. Either would create a lower thermal pressure in the main sequence bubble, which in turn would place the wind termination shock further away from the star. That this can indeed occur would seem to follow from the calculations of Chevalier et al. [10], which give a wind termination shock 28 pc from the central star for GRB 990123. The intermediate velocity and 50 $\mathrm{km\,s^{-1}}$ lines can be used to find out how much time the star spent as a Wolf-Rayet star before producing a supernova.

The intermediate velocity line is only visible during WR1 and the first part of WR2, although the absence of this line may be the result of the position of the shell fragments (see Sect. 4.5). The line at 50 $\mathrm{km\,s^{-1}}$ appears later, marking the transition from WR2 to WR3, and thus providing another reference point for the age of the progenitor star, although we cannot be certain of being able to identify this line at all, since it is so close to the zero velocity line.

4.7.2 The circumstellar medium

While some gamma-ray burst afterglows indicate a $1/r^2$ density distribution in the circumstellar medium, others appear to indicate a constant density (Chevalier et al. [10]). The only areas with constant density in the circumstellar medium are the hot bubbles of shocked wind material, which drive the shells outward. If the gamma-ray burst afterglow indicates a constant density medium, this means that the relativistic jet has reached the hot bubble and therefore already passed the freely expanding wind region. Consequently, in a constant density afterglow profile, the high velocity line caused by the Wolf-Rayet wind should not be visible, since the afterglow source is already between that area and the observer. Similarly, the presence of a high velocity absorption line would seem to indicate that the afterglow was caused in a $1/r^2$ density region.

4.7.3 GRB 021004

The best observations so far of the spectrum of a Gamma-ray burst afterglow have been made of GRB 021004. Identification of the CIV and SiIV lines indicate distinctive absorption lines at velocities: 0 $\mathrm{km\,s^{-1}}$, 560 $\mathrm{km\,s^{-1}}$, and 3000 $\mathrm{km\,s^{-1}}$ (Schaefer et al. [62]), although the last line may actually consist of two separate components, both at high velocities. This pattern agrees qualitatively with our column density simulations during the early Wolf-Rayet phase, which would indicate that the progenitor star only spent a short time as a Wolf-Rayet star. A faster Wolf-Rayet wind ($\sim$ 3000 $\mathrm{km\,s^{-1}}$ rather than 2200 $\mathrm{km\,s^{-1}}$) remains within acceptable parameters for massive stars. Shell velocities of $\sim$ 500 $\mathrm{km\,s^{-1}}$ can be reached by adjusting the wind velocities and mass-loss rates of the red supergiant and Wolf-Rayet winds (cf. Eq. 4.4). Calculations done by Li & Chevalier [37] indicate that the afterglow of GRB 021004 results from interaction with stellar wind rather than a constant density medium. This agrees with the presence of high velocity lines in the spectrum. If there are indeed two high velocity lines instead of one, this might be explained by a two-stage Wolf-Rayet wind (a fast wind, followed by a slower wind as the star expands due to He-shell burning), by the presence of clumps in the Wolf-Rayet

wind, or by acceleration of part of the Wolf-Rayet wind by radiation from the Gamma-ray burst itself.

VLT spectra of GRB 021004 were presented by Fiore et al. [19]. These observations show a larger number of absorption lines at low velocities, leading to a total of six different lines in both CIV and SiIV. The large number of intermediate velocity components (3) can be explained as the result of multiple clumps of the shell fragments appearing in the line of sight (see Sect. 4.5). The column densities for all these lines are on the order of 10^{14} to 10^{15} particles per cm^2. In order to compare these to our own results, we calculated the total column densities in the intermediate velocity and 2200 km s^{-1} lines. The results in Fig. 4.13 show that total column densities for the Wolf-Rayet wind line are nearly constant throughout the Wolf-Rayet phase. Not surprisingly so, since the mass loss rate and wind velocity remain unchanged. The location of the wind termination shock varies, so the total Wolf-Rayet wind area changes over time, but this takes place at a range where the wind density is extremely low (see Figs. 4.3 to 4.5), therefore the change in column density is minimal. The column density of the intermediate velocity feature is strongly time dependent. After all, this feature is the result of a moving shell which expands into a spherical volume; therefore, the density in the shell will decrease with $\rho \sim r^{-2}$ until the shell remnants hit the outer edge of the bubble. Column densities for the lines in Fig.4.13 are on the order of 10^{-5} to 10^{-7} in g cm^{-2}, which corresponds to 10^{19} to 10^{16} amu per cm^{-2}. As carbon has an average weight of about 12 amu, this amounts to a particle column density of 10^{18} to 10^{15} carbon ions per cm^{-2}, if the gas were pure carbon. Obviously, this is not the case, so the column density of carbon ions would probably be on the order of 0.1 to 10 percent, which corresponds quite well with the figures found by Fiore et al. [19]. We should keep in mind that in Fig. 4.13 the column densities have been averaged over the 200 radial lines. This does not affect the Wolf-Rayet wind line, since the density distribution of the wind is more or less spherically symmetric. However, the shell fragments, which make up the intermediate velocity line do not have such a symmetry, so column densities in the line of sight may vary considerably (see Figs. 4.10 through 4.12).

A pattern of blue-shifted absorption lines similar to those observed in a gamma-ray burst afterglow may be visible in the spectra of Type Ib/c supernovae, since these supernovae also have Wolf-Rayet stars as progenitors. Dopita et al. [15] attributed narrow P Cygni profiles seen in Hα and Hδ in the spectrum of SN 1984E to a Wolf-Rayet wind with a velocity of about 3000 km s^{-1}. Similarly, Bowen at al. [4] and Fassia et al. [18] note the presence of a broad absorption feature covering ~ 350 km s^{-1} in the spectrum of SN 1998S, which may be caused by a moving shell.

4.8 Final remarks

In this paper, we describe a powerful method for constraining the progenitors of GRBs and SNe through narrow circumstellar spectral lines (see also van Marle et al. [73]). While we expect a Type Ib/c supernova from practically all massive stars whose hydrogen-rich envelope is stripped, only a small fraction of these stars — i.e. (0.002 . . . 0.004) (van Putten [76]) — produces a gamma-ray burst. We have shown that the characteristics of the circumstellar line spectrum change significantly during the Wolf-Rayet evolution — in line with the fact that only a fraction of the Galactic Wolf-Rayet stars are still surrounded by a nebula — which means that the circumstellar lines which are observable in a GRB after-

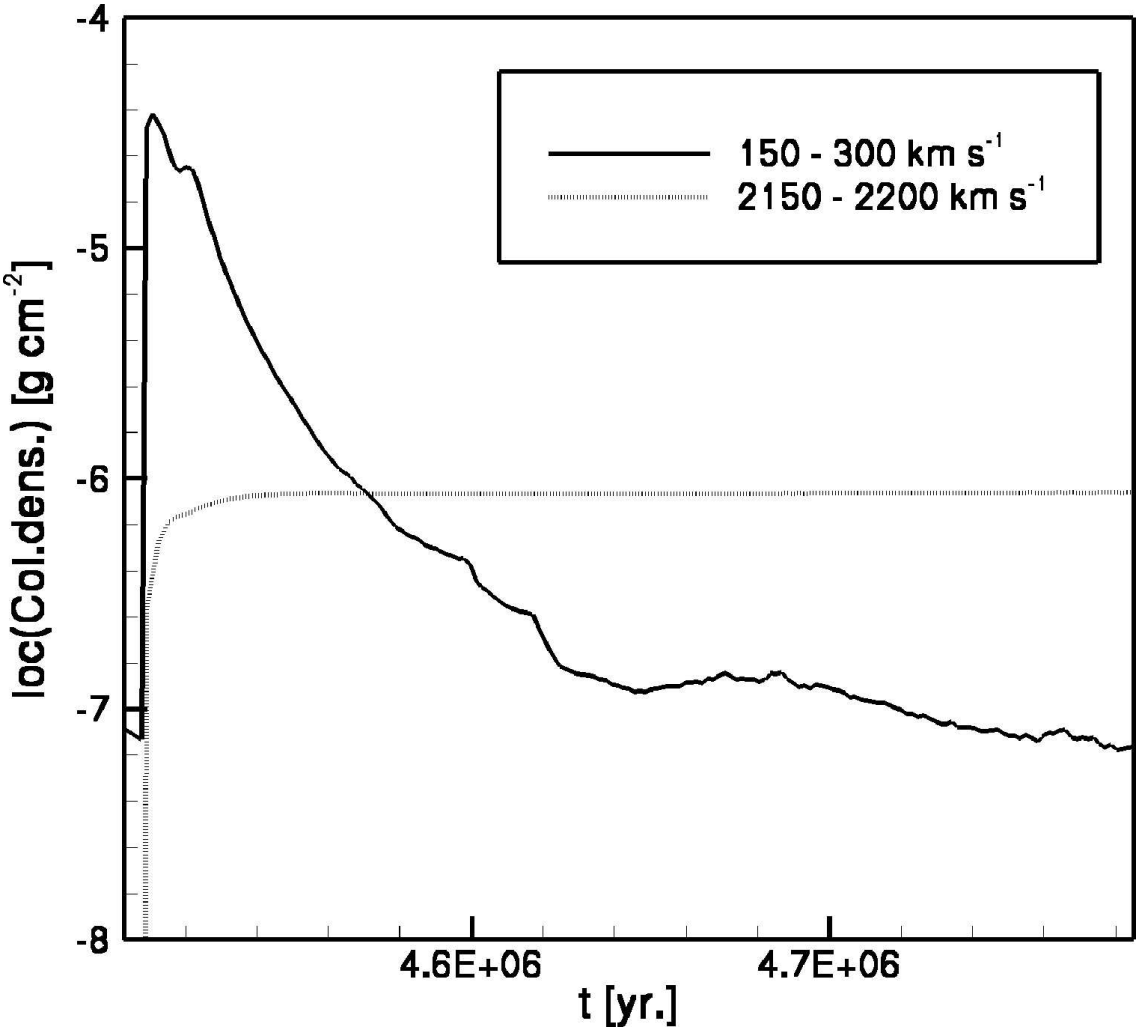

Figure 4.13: The total column density of the intermediate velocity and 2200 km s^{-1} lines, respectively. The column density of all velocity intervals between 150 and 300 km s^{-1} and 2150 and 2200 km s^{-1} has been added up. Clearly, once the Wolf-Rayet wind starts, the total column density within the Wolf-Rayet wind remains more or less constant. The intermediate velocity feature is extremely time dependent, since this line is caused by a moving shell that expands into a spherical volume. Note that these column densities where averaged over 200 radial lines. This makes little difference for the Wolf-Rayet wind line, since the density of the wind is barely angle dependent. The column density in the intermediate velocity line, however, is angle dependent, as is shown in Fig. 4.10.

glow or in a supernova explosion produced by a Wolf-Rayet star are sensitive indicators of the duration of the preceding Wolf-Rayet phase.

According to stellar evolution models, the duration of the Wolf-Rayet phase, which is the final evolutionary phase before its death, can vary between almost zero and 10^6 yr, where it is larger for higher mass and/or metallicity (Meynet & Maeder [45]). The fact that only part of the Galactic Wolf-Rayet stars actually show a nebula means that those tend to disperse on a time scale which is shorter than the mean life time of Wolf-Rayet stars, about 5×10^5yr. Thus, Wolf-Rayet nebulae evolve on the evolutionary time scale of their central star. The corresponding absorption lines at the time the star explodes may be used, to determine whether a Wolf-Rayet star died young or old.

In principle, the evolution of main sequence and Wolf-Rayet bubbles are influenced — although weakly — by various stellar and interstellar medium parameters (Weaver et al. [79]). However, the life time of the Wolf-Rayet shell, or of the intermediate velocity absorption line feature, is on the order of shell radius divided by shell velocity. For shell velocities obtained within our model, this time scale is some 10 000 yr. As the shell velocities coincide well with the values derived for the intermediate velocity absorption components in the afterglow spectra of GRB 021004, the conclusion that the Wolf-Rayet phase of its progenitor lasted a much shorter time than the average Wolf-Rayet life time is in fact independent of the particular choice of stellar and interstellar medium parameters used in our model.

A short Wolf-Rayet phase of the progenitor of GRB 021004 rules out that the underlying Wolf-Rayet star was formed through the LBV-scenario (cf. García-Segura et al. [24]), since in this case the duration of the Wolf-Rayet phase corresponds to the full duration of core helium burning (about 5×10^5yr), and the nebula would be expected to have dispersed by the time the central star dies. Early mass transfer (so called Case A or Case B; cf. Wellstein & Langer [80]), which — just like LBV type mass loss — already produces an early Wolf-Rayet phase during core helium burning, can also be ruled out.

The presence of an intermediate velocity component in the afterglow spectrum of GRB 021004 indicates that the Wolf-Rayet shell was still intact when the star exploded, i.e. that the Wolf-Rayet phase was relatively short. This could imply a progenitor zero age main sequence (ZAMS) mass close to the lower ZAMS mass limit for Wolf-Rayet star formation, which is at about 25 $M_\odot$ for solar metallicity (Meynet & Maeder [45]) and larger for smaller Z. Alternatively, the progenitor of GRB 021004 could have evolved into the Wolf-Rayet phase through so-called Case C mass transfer, which occurs at the end of core helium burning, and which is assumed to give rise to a common envelope phase (cf. Podsiadlowski et al. [56]). In that case, the ZAMS mass of the progenitor would have to be smaller than the lower ZAMS mass limit for Wolf-Rayet star formation.

A short duration of the Wolf-Rayet phase might also avoid the strong angular momentum loss of the stellar core that is associated with the strong Wolf-Rayet mass loss (Langer [36], Petrovic et al. [53]), which otherwise might reduce the core angular momentum below the critical value required within the collapsar model (MacFadyen & Woosley [39]). A late common envelope phase, on the other hand, might even lead to a spin-up of the Wolf-Rayet star, either through tidal interaction in a tight post-common envelope binary system (e.g. van Putten [76]) or through angular momentum gain in the course of a merger event (e.g., Fryer & Heger [21]).

Observed circumstellar spectral lines for a larger number of SNe Ib/c or GRB afterglows might enable us to empirically constrain the subsample of Wolf-Rayet stars that are capable of producing a gamma-ray burst. Since prototype observations exist for both cases, we may be able to reach this aim within a certain period of time. However, more models of the circumstellar medium of massive supernova progenitors at various metallicities, both for single stars and binary systems, are also needed before more general conclusions can be drawn.

Acknowledgements

We would like to thank Alexander van der Horst, Rhaana Starling, Klaas Wiersema and Ralph Wijers for their information on the spectrum of the afterglow of GRB 021004. This work was sponsored by the Stichting Nationale Computerfaciliteiten (NCF), with financial support from the Nederlandse Organisatie voor Wetenschappelijk Onderzoek (NWO). This research was done as part of the AstroHydro3D project:
(http://www.strw.leidenuniv.nl/AstroHydro3D/)

5

Constraints on gamma-ray burst and supernova progenitors through circumstellar absorption lines. (II)

A. J. van Marle, N. Langer and G. García-Segura
To be submitted to Astronomy & Astrophysics

Abstract

Based on a 2-dimensional hydrodynamic simulation for the interaction of the various winds of a 60 $M_\odot$ star during its evolution, we compute the time evolution of the velocity dependent column density of the circumstellar medium in the luminous blue variable (LBV) and Wolf-Rayet phase. The wind interactions in the circumstellar medium result in moving shells which, together with the stellar wind itself, create a series of discrete blue-shifted absorption features that vary over time, as old features dissipate into the circumstellar medium and new features are created. The absorption lines created by the stellar wind are narrow, constant features. The moving shells, on the other hand, create broad absorption features, which may last only for a short period of time as they dissipate into the circumstellar medium or are destroyed by collisions with each other. A comparison with the afterglow absorption spectrum of gamma-ray burst GRB 021004 shows that a 60 $M_\odot$ star is not a likely progenitor for this gamma-ray burst, as the Wolf-Rayet period of such a star would last too long. However, a close binary with a late common-envelope phase may produce a circumstellar medium closely resembling the LBV to Wolf-Rayet evolution, but with a much shorter Wolf-Rayet period. This scenario can not be ruled out for GRB 021004.

5.1 Introduction

Circumstellar nebulae are created by the interactions of stellar winds with the surrounding medium. Typically, a fast wind sweeps up the interstellar gas or a preceding slower wind and forms a shell that travels outward. This is the case for planetary nebulae, where the fast post-AGB wind sweeps up the slow AGB wind (Kwok [34]). Massive stars ($\geq$ 25 $M_\odot$) undergo a red to blue evolution in the Hertzsprung-Russell diagram (Meynet & Maeder [44]). In this evolutionary phase, the radius of the star decreases, and as a result the escape velocity at the surface and therefore the wind velocity increase. A star in the 25...40 $M_\odot$ range evolves from a red supergiant to a Wolf-Rayet star. The red supergiant has a slow, dense wind, whereas the Wolf-Rayet star has a fast, less dense wind. In the case of a 60 $M_\odot$ star the main sequence is followed by a luminous blue variable (LBV) stage, which lasts only for a very short while ($\sim$ 10 000 years). During the LBV stage the mass loss rate is extremely high ($\sim 10^{-3}$ $M_\odot$ yr^{-1}), while wind velocities are in the order of a 100...1000 $km\,s^{-1}$. After the LBV stage the star becomes a Wolf-Rayet star. Such interactions create circumstellar nebulae around Wolf-Rayet stars. These nebulae are temporary features, which will eventually dissipate into the surrounding medium. This explains why circumstellar nebulae can only be observed around a fraction of all Wolf-Rayet stars.

Massive stars are thought to end their evolution in violent explosions, which are visible as Type Ib/c supernovae and (in some cases) as long gamma-ray bursts. These events produce a massive output of radiation in the UV...IR spectrum, either in the supernova photosphere or in the interaction between a relativistic jet and the surrounding medium. This radiation surge has to pass through the circumstellar medium, which was shaped by the stellar wind during the evolution of the star. Part of the radiation is absorbed, creating an absorption spectrum, which can be used to analyze the contents of the circumstellar bubble as to density, composition and velocity structure. So far the best absorption spec-

Table 5.1: Mass-loss history of a 60 $M_\odot$ star (Z=0.02).

Phase	End of phase [yr]	$\dot{m}$ [$M_\odot$ yr^{-1}]	V [km s^{-1}]	n_{photon} [s^{-1}]
Main Sequence	0.34499×10^{7}	0.351×10^{-5}	0.242×10^{4}	0.712×10^{48}
LBV	0.34796×10^{7}	0.471×10^{-3}	0.492×10^{3}	0.665×10^{48}
Wolf-Rayet	0.38861×10^{7}	0.641×10^{-4}	0.225×10^{4}	0.622×10^{50}

trum of the circumstellar medium has been found in the afterglow of gamma-ray burst GRB 021004. It was proposed that the large number of absorption lines for CIV and SiIV visible in this spectrum can be explained as the result of circumstellar wind and shells (Schaefer et al. [62]; Mirabal et al. [47]; Fiore et al. [19] and Starling et al. [65]). In van Marle et al. [73], [74], the evolution of the circumstellar medium around a 40 $M_\odot$ star is described, and a method to predict the absorption spectrum, produced by the circumstellar medium, is developed and applied to compare with observations of GRB 021004. We will now follow a similar procedure for the circumstellar medium around a 60 $M_\odot$ star. While the 40 $M_\odot$ star passed through the red supergiant phase, before becoming a Wolf-Rayet star, the 60 $M_\odot$ star evolves from the main sequence to the LBV stage and then moves on to become a Wolf-Rayet Star. This increases the number of temporary features, since the LBV wind and the shell it pushes outward are fast enough to show up as independent features rather than become part of the zero velocity component, as is the case with similar phenomena around a red supergiant star (García-Segura et al. [24], [25]; van Marle et al. [73], [74]).

Blue-shifted absorption lines caused by the circumstellar medium could also be visible in the spectrum of Type Ib/c and Type II supernovae. However, a supernova spectrum contains many lines from the supernova material itself, which makes it difficult to identify circumstellar medium components. Dopita et al. [15] found narrow P Cygni profiles seen in Hα and Hδ in the spectrum of the Type IIL SN 1984E indicating a Wolf-Rayet wind with a velocity of about 3000 km s^{-1}. A 350 km s^{-1} absorption line in the spectrum of Type IIL SN 1998S can be attributed to a moving shell (Bowen et al. [4]; Fassia et al. [18]).

5.2 Simulating the circumstellar bubble

The evolution of the circumstellar medium around a massive star can be divided into three stages; the result of the evolutionary track of the star. A 60 $M_\odot$ star begins as a main sequence star, develops into a luminous blue variable and finally becomes a Wolf-Rayet star. This means that in the circumstellar medium three interactions take place:

1. First: an interaction between the fast, low density main-sequence wind and the interstellar medium. This interaction creates a moving shell, driven outward by the high thermal pressure of the shocked wind material. Such an interaction can be described analytically. (Weaver et al. [79])

2. In the next phase the slow, dense LBV wind hits the bubble created by the main-sequence wind, creating a new shell (the LBV shell), which moves into the main

sequence bubble.

3. Finally, the massive, high velocity Wolf-Rayet wind sweeps up the remnants of its predecessors. The Wolf-Rayet wind drives a third shell outward, which overtakes the LBV shell. Both shells are destroyed by the collision. The remnants continue to move outward.

In order to construct a model of the circumstellar medium we use the same method as described in van Marle et al. [74], from here on referred to as Paper I. We have divided the evolution of the star into three stages (main sequence, LBV and Wolf-Rayet), each with a constant wind velocity, mass loss rate and ionizing photon flux. The average mass loss rate follows from the evolution of the total mass of the star for each of these periods. The average wind velocity is chosen so that the total kinetic energy output of the star remains the same. The number of ionizing photons is calculated from the surface temperature of the star, using a Planck emission curve. As input model we used the 60 $M_\odot$ star model with metallicity 0.02 that was calculated by Schaller et al. [63]. The resulting parameters for the stellar wind and photon count are given in table 5.1. The density of the interstellar medium is set at $10^{-22.5}$ g cm^{-3}. The effect of photo-ionization was included in the simulation by calculating the Strömgren radius along each radial gridline and correcting the temperature and mean particle weight within this radius, as was described by García-Segura & Franco [23] and García-Segura et al. [26].

The hydrodynamical simulations were done with the ZEUS 3D hydrodynamics code by Stone and Norman [67].

We simulate the main sequence only in 1D. Because they are highly unstable the LBV and Wolf-Rayet wind interactions have to be done in 2D, so we have taken the end result of the 1D simulation and mapped this onto a 2D grid, as was described in García-Segura et al. [24]; [25]. The transition from 1D to 2D has to be made before the start of the LBV phase in order to include the instabilities in the LBV shell. This is different from the 40 $M_\odot$ case described in Paper I, where we could simulate most of the red supergiant phase in 1D. Since we want to follow the evolution of the circumstellar medium to the moment of supernova, we have calculated the whole circumstellar bubble in 2D, instead of using only the inner part as was done by García-Segura et al. [24]; [25]. This method is similar to the one used in van Marle et al. [72] and was also described in Paper I. A similar calculation for a 60 $M_\odot$ star was done completely in 2D by Freyer et al. [20].

5.3 The circumstellar bubble during main sequence and LBV phase

5.3.1 Main sequence phase

At the beginning of the main sequence the HII region, created by radiation from a massive star, pushes a shell into the interstellar gas. At the same time the kinetic energy of the wind is converted into thermal energy by collision with the surrounding matter. This creates a hot bubble, which pushes a shell into the HII region. Unlike the case for the 40 $M_\odot$ star we have set the main sequence wind velocity at three times the escape velocity. This,

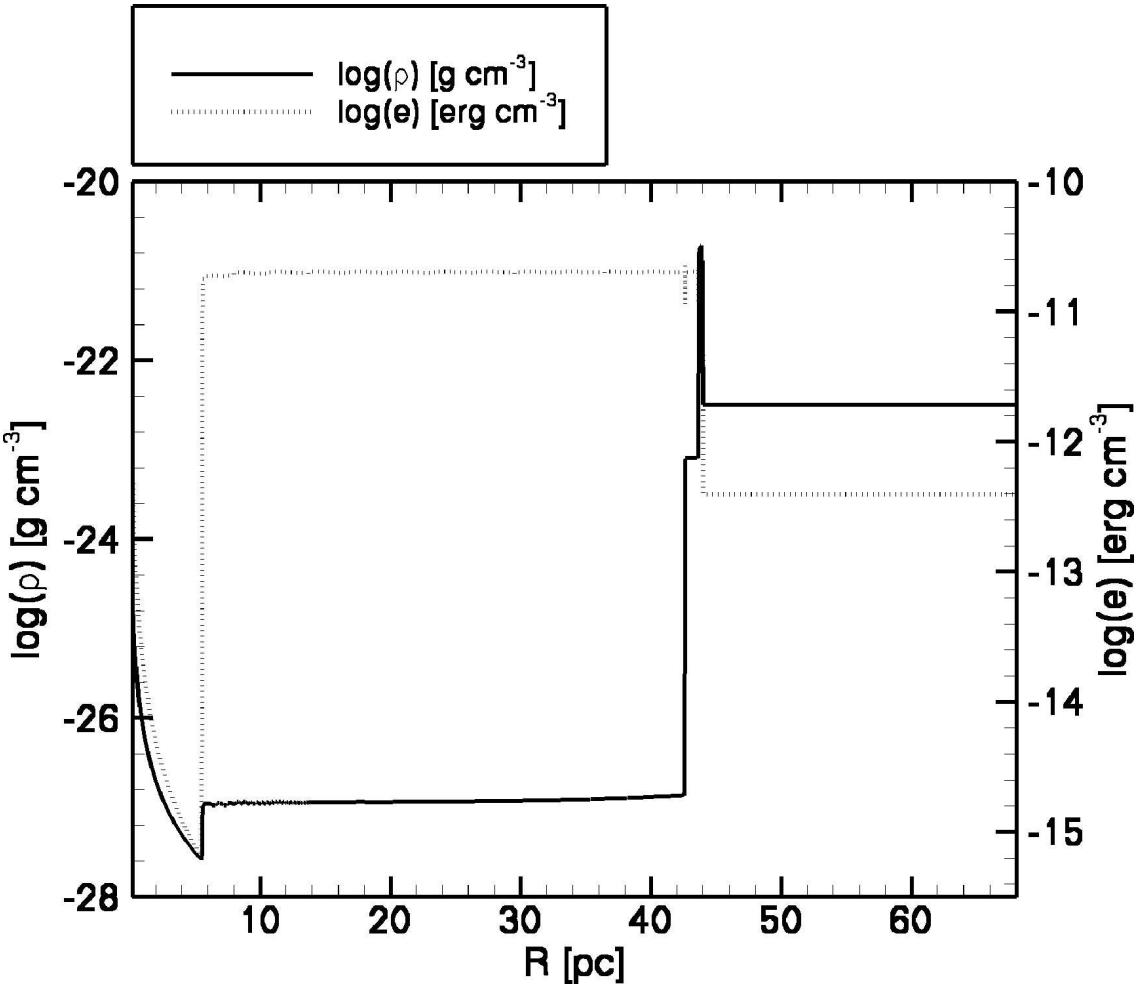

Figure 5.1: Structure of the circumstellar bubble around our 60 $M_\odot$ star at the end of the main sequence phase (t = 3.448 Myr). This figure gives mass density (continuous line) and internal energy density(dotted line) as a function of the radius. From left to right we have: The freely expanding main sequence wind, the wind termination shock, the hot bubble with the small HII region, the shell driven by the thermal pressure of the bubble and the interstellar medium.

combined with the higher mass loss rate of the 60 $M_\odot$ star, raises the thermal pressure in the bubble to the point where the shell driven into the HII region moves supersonically. Therefore, no pressure equilibrium can be reached between wind bubble and HII region and the wind driven shell sweeps up the entire HII region. (In the case of the 40 $M_\odot$ model an HII region can exist outside the wind bubble, even if the wind velocity is set at three times the escape velocity.) The end result is a hot bubble with nearly constant density, which drives a shell into the cold interstellar medium. This can be seen in Fig. 5.1, which shows the circumstellar bubble at the end of the main sequence. Close to the star is the free streaming wind, where the density and internal energy decrease with the square of the radius. At a radius of ca. 6 pc the wind hits the termination shock where it slows down abruptly. Its kinetic energy is converted to heat, causing a sudden increase in internal energy. At 45 pc this hot bubble ends. Here the internal energy is converted back into kinetic energy as the thermal pressure drives a shell outward. The small density jump, observed just before the shell, is caused by the radiation from the star, which ionizes

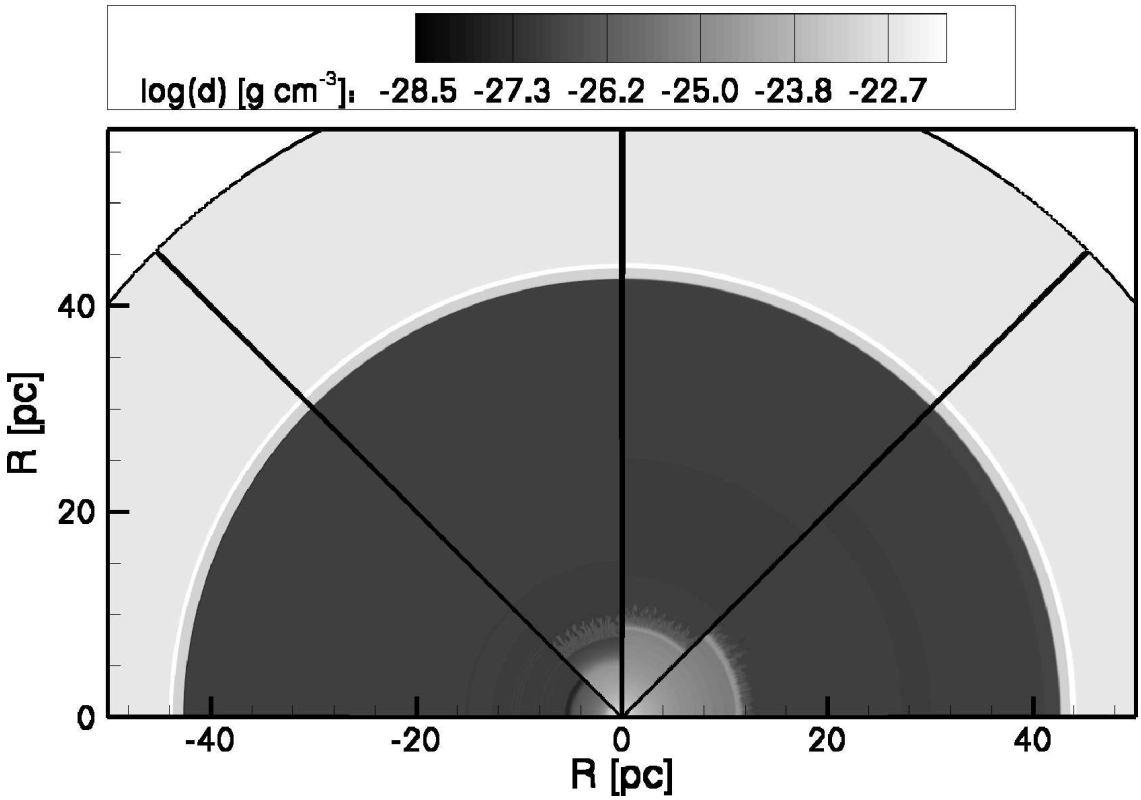

Figure 5.2: The logarithm of the density [g cm^{-3}] of the circumstellar medium, during the LBV phase. Each segment shows a moment in time starting on the left at t = 3.4516 Myr. Each following segment is taken 7.927×10^3 years later. The slow, dense LBV wind pushes a shell outward into the hot bubble. The hot bubble itself pushes a second shell out into the interstellar medium.

a small HII region beyond the wind bubble. This HII region is very small, especially compared to a similar region around a 25...40 $M_\odot$ star (van Marle et al. [72], [73] and Paper I). If the main sequence is modeled in two dimensions, the ionizing radiation will break through the wind driven shell, creating local 'fingers' of photo-ionized gas, which reach out from the wind driven bubble. This can be seen in the results from Freyer et al. [20].

5.3.2 LBV phase

During the LBV phase the mass loss rate increases dramatically while the wind velocity decreases. As a result, a new shell is created once the LBV wind reaches the termination shock. This shell, driven by the LBV wind, moves outward into the main sequence bubble. By the end of the LBV phase, the circumstellar medium is built up as follows (See also Fig: 5.2). Closest to the star is the freely expanding LBV wind. This region ends at ca. 12 pc in the wind termination shock. The shock itself is marked by a thin shell of shocked LBV wind material, which is driven outward by the wind. Unlike the similar shell during the red supergiant phase of a 40 $M_\odot$ star (García-Segura et al. [25]; van Marle et al. [72], [73], Paper I), the LBV wind-driven shell has a significant radial velocity. This is the result of the ram pressure of the LBV wind, which is much higher than the ram pressure of the red supergiant wind. Next comes the hot bubble, which in turn pushes a

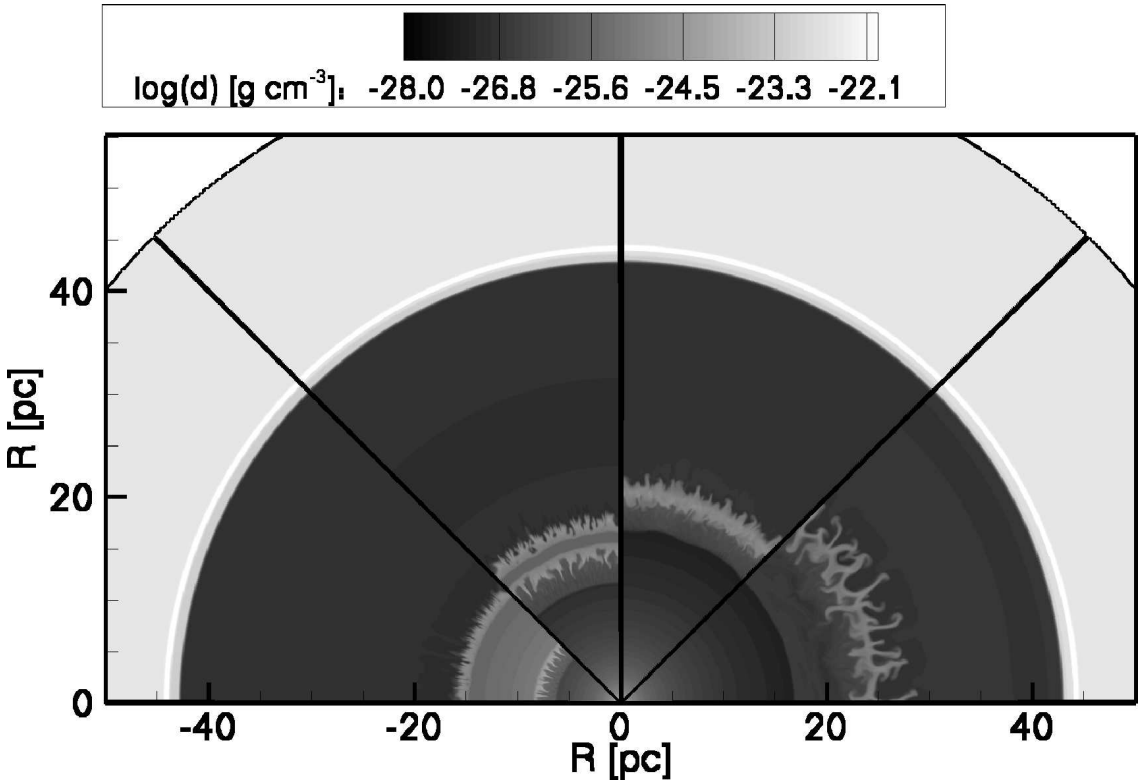

Figure 5.3: Similar to Fig. 5.2 but during the early WR phase (transition from WR1 to WR2 in section 5.4). Each segment shows a moment in time starting on the left at t = 3.4881 Myr. Each following segment is taken 7.927×10^3 years later. The fast Wolf-Rayet wind sweeps up the LBV wind in a shell, which overtakes the earlier LBV shell. Both shells are fragmented during the collision and the fragments continue to travel outward. Eventually, they will collide with the main sequence shell and dissipate into the surrounding medium.

shell (r ~ 45 pc. in Fig. 5.2) into the interstellar medium.

5.4 The circumstellar bubble during the Wolf-Rayet phase

The Wolf-Rayet phase can be divided into three separate parts (based on the evolution of the circumstellar medium, not the evolution of the star).

During the first phase (WR1), starting at t ≃ 3.48 Myr, the fast, high-density WR wind drives a shell into the surrounding medium (The LBV wind remnant). This shell moves rapidly outward, much faster than the shell driven by the LBV wind.

The second phase (WR2) starts as the two shells collide (t ≃ 3.5 Myr). Both shells are highly unstable already and will break up during the collision. This process can be seen in Fig. 5.3. Here we see the Wolf-Rayet wind driven shell overtake the LBV shell. Unlike the collision between red supergiant shell and Wolf-Rayet shell as described in Paper I, the remnants of the two shells are not fragmented completely and there is less independent movement of the individual fragments. They remain more or less together while they travel into the main sequence bubble. The difference is the result of both the relative densities and velocities of the two shells upon collision. The Wolf-Rayet shell is approximately ten times as dense as the LBV shell. In contrast, the red supergiant shell

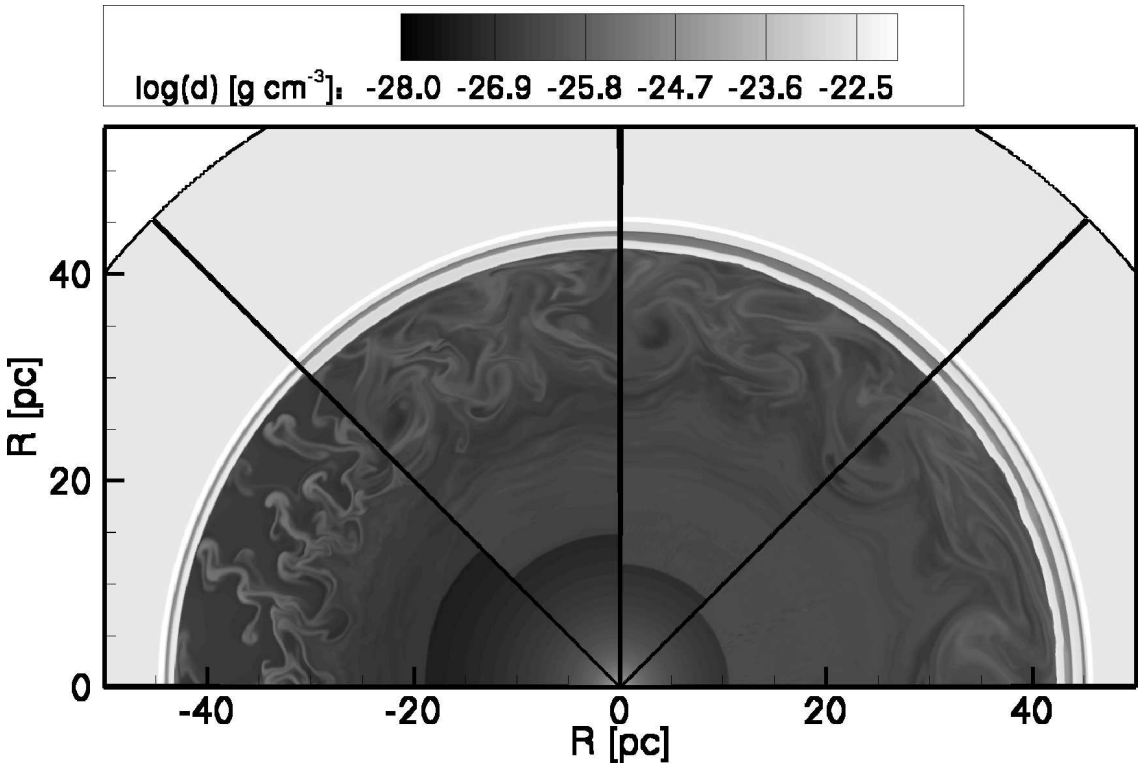

Figure 5.4: Similar to Fig. 5.2 and 5.3 this figure shows the collision of the shell fragments with the outer edge of the hot bubble (transition from WR2 to WR3 in section 5.4). The first segment (left) shows the density of the circumstellar medium at t = 3.5436 Myr. Since this process takes more time than the ones shown before, the time difference between segments has been increased to 4.7565×10^4 years The shell fragments travel outwards in the bubble and collide with the outer edge. Afterwards, they dissipate into surrounding medium. The region between the low density bubble and the thin shell at r ≃ 47 pc is the HII region, created by high energy photons from the Wolf-Rayet star.

has about the same density as the Wolf-Rayet shell (Paper I). The velocity difference is also much greater: The Wolf-Rayet shell overtakes the LBV shell with a relative velocity of ca. 400 $\mathrm{km\,s^{-1}}$, twice as much as the relative velocity of the Wolf-Rayet shell with respect to the red supergiant shell in Paper I. This phase may last only for a short while, depending on the location of the collision point relative to the outer limit of the main sequence bubble. If the two are located closely together, the shell fragments can only travel a short distance, until they hit the edge of the bubble.

The final part of the Wolf-Rayet phase (WR3) occurs after t ≃ 3.53 Myr, when the shell fragments collide with the edge of the main sequence bubble (Fig. 5.4). This phase lasts much longer than WR1 and WR2. During this phase there is only one hot bubble, which is heated by the kinetic energy of the Wolf-Rayet wind and drives a shell into the interstellar medium. The kinetic energy of the wind is high, which causes an increase in the temperature of the wind bubble, which in turn accelerates the movement of the shell. Also, during the Wolf-Rayet phase the flux of high energy photons increases, which results in a photo ionized HII region outside the wind bubble. This means, that the hot bubble starts to show a density discontinuity, like the one we found for the 40 $M_\odot$ star (van Marle et al. [72], [73] and Paper I). However, for the 60 $M_\odot$ star the HII region is

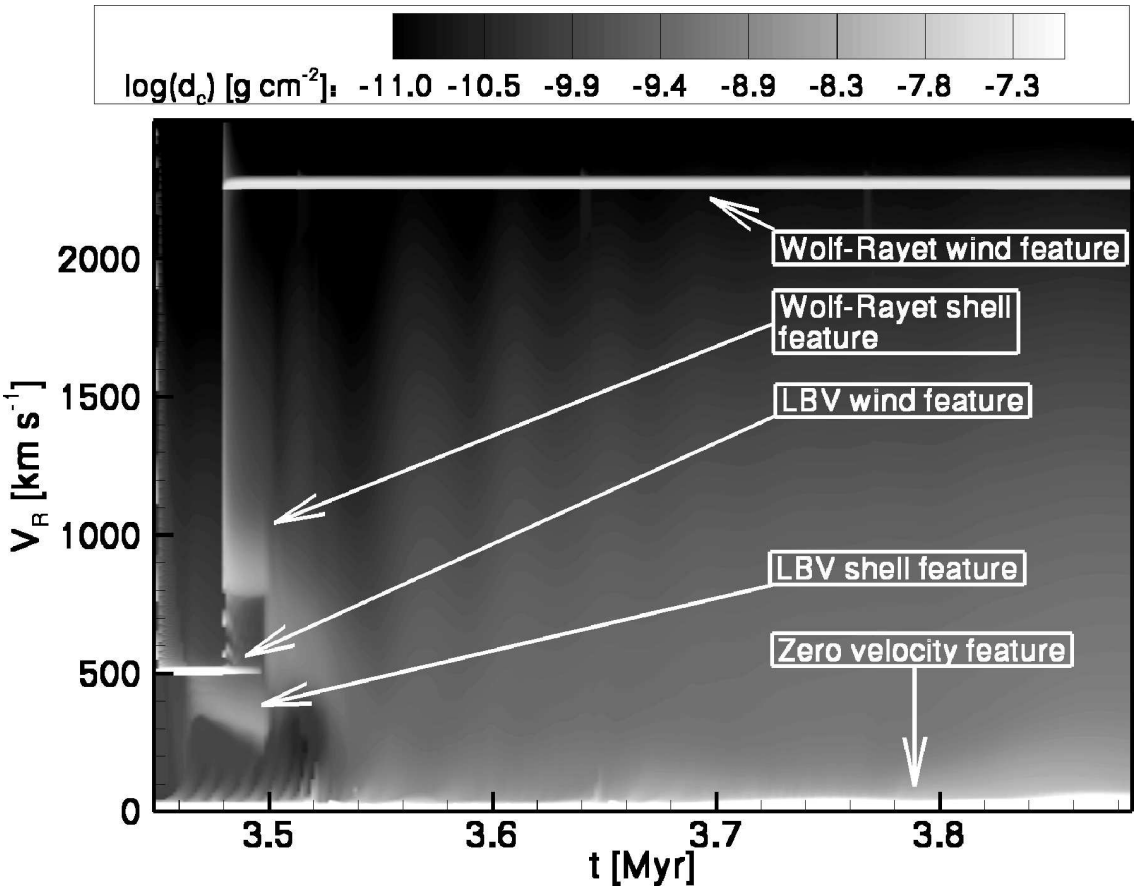

Figure 5.5: Column density $d_c(v, \Delta v)$ with $\Delta v = 1$ km s^{-1} of the circumstellar medium during the LBV and Wolf-Rayet period as a function of radial velocity and time, averaged over 200 radial grid lines. On the horizontal axis the time since the birth of the star in years. On the vertical axis the radial velocity in km s^{-1}. The plot starts at the end of the main sequence phase when there is only matter moving at low velocity. As the LBV phase starts a narrow feature appears for the LBV wind and a broader feature for the LBV wind driven shell. When the star becomes a Wolf-Rayet shell, the Wolf-Rayet wind and the shell driven by this wind both form independent features as well. Once the Wolf-Rayet shell overtakes the LBV shell, both shells and the LBV wind disappear and a new shell is formed. The fragments of this shell eventually collide with the outer edge of the bubble and dissipate. Afterwards, only two independent features remain: the Wolf-Rayet wind and the zero velocity component.

very small ($\leqslant 5$ pc) compared to the total size of the hot bubble (Fig. 5.4).

5.5 Calculating the absorption spectrum

We use the same method as described in Paper I to calculate the absorption spectrum of the circumstellar medium. From our simulations of the circumstellar medium we calculate the column density as a function of the radial velocity. For each radial grid line we move outward from the star and take at each gridpoint the local column density (density multiplied with the radial length of the grid cell), the radial velocity (rounded to 1 km s^{-1} intervals), and the temperature. This procedure gives us the column density as a function of radial velocity. We take thermal broadening into account by spreading the column

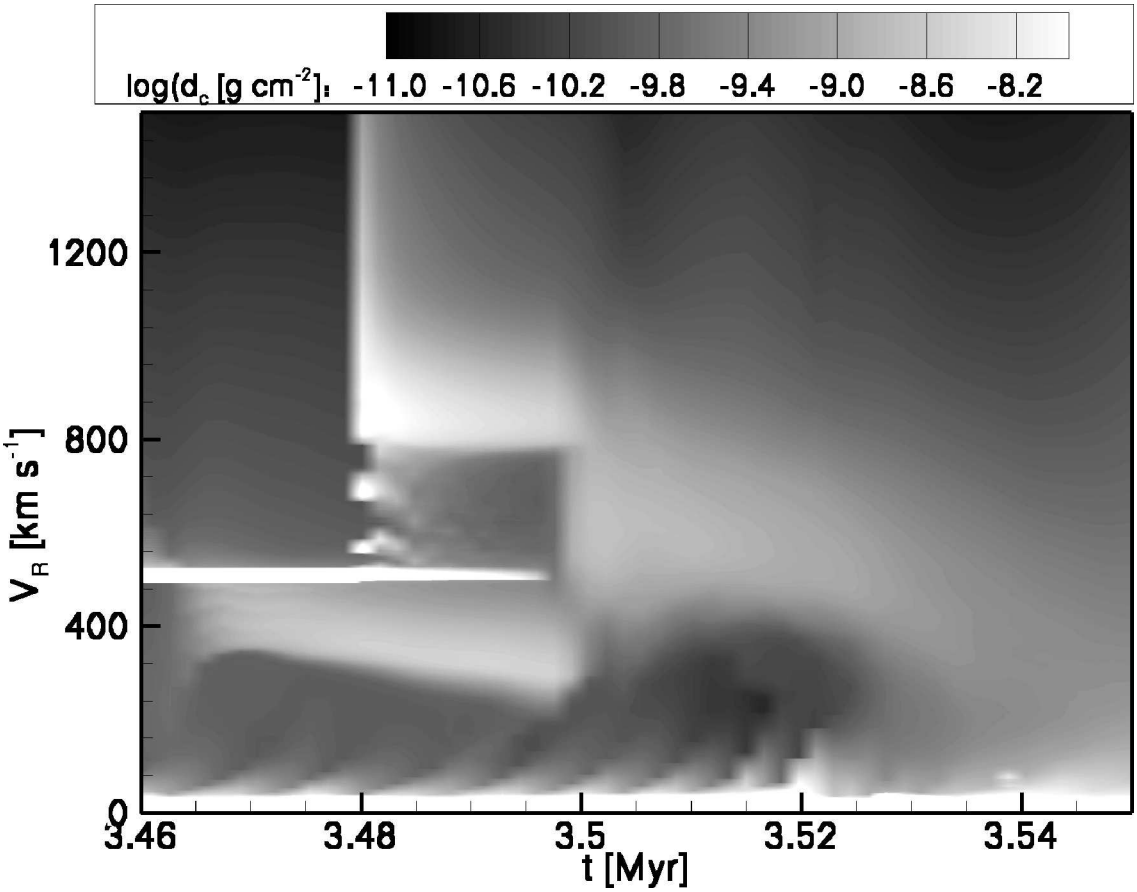

Figure 5.6: This figure shows the most interesting part of Fig. 5.5. This is the time period between the start of the LBV phase and the end of WR2. The first absorption feature to appear is the thin line at 490 $\mathrm{km\,s^{-1}}$ created by the LBV wind. Once this wind has reached the termination shock it forms a shell, which causes the broad, low velocity component. Once the Wolf-Rayet wind starts a new shell at ca. 800 $\mathrm{km\,s^{-1}}$ is created (immediately, since this shell is created by sweeping up the preceding wind, rather than by collision with the wind termination shock). This shell sweeps up the LBV wind, so the LBV wind feature disappears. Once the Wolf-Rayet shell reaches the LBV shell, both shells disappear. A new shell is created where the Wolf-Rayet wind meets the hot bubble. This shell shows up as a new broad feature at ca. 600 $\mathrm{km\,s^{-1}}$, which will last until its fragments hit the edge of the bubble and dissipate.

density of each grid cell over a velocity interval that is calculated from the Maxwell-Boltzmann distribution for particle velocities in the local rest frame. This gives us the following quantity:

$$\mathrm{d_c(v, \Delta v)} = \int_{\mathrm{r=0}}^{\mathrm{r=R}} \rho(\mathrm{r})\mathrm{P}(\mathrm{v_r}, T)\Delta \mathrm{v_r dr} \tag{5.1}$$

with: v_r the radial velocity, ρ the mass density and P the probability function for a particle to have a velocity in a given velocity interval along a single axis. For the interval Δv we use 1 $\mathrm{km\,s^{-1}}$. Since the circumstellar medium is optically thin, the quantity d_c is equivalent to the absorption as a function of blue-shift, that photons coming from the central star would encounter.

This method does not account for the composition of the circumstellar medium, which depends both on the chemical composition of the stellar wind and the degree of ionization.

5.6 Composition of the circumstellar bubble

In our simulation we do not consider the composition of the gas. In order to get a quantitative analysis of the blue-shifted absorption features, one would need to know both the metallicity of the gas and the ionization state. Although we do not simulate these quantities we can say a few things about them. The metallicity of the circumstellar bubble is of course a direct result of the composition of the stellar wind, which in turn depends on the evolutionary phase of the star. Typically, line-driven winds like the main-sequence and Wolf-Rayet wind will consist of the ions with the lowest mass in the outer layers of the star. This means that during the main sequence the wind will be almost purely hydrogen. The composition of the Wolf-Rayet wind changes over time, from mostly helium with some hydrogen during the early Wolf-Rayet phase, to helium and carbon during the later stages.

The LBV wind, which is produced by an unstable star, will have a considerably larger abundance of heavier ions. The shell driven by the main sequence wind consists solely of interstellar matter. The shell driven by the LBV wind into this bubble will be composed mostly of LBV wind material, and of some matter from the hot bubble itself. The third shell, driven by the Wolf-Rayet wind into the LBV wind, will at first consist only of LBV wind material that has been swept up. After the collision with the LBV shell, the Wolf-Rayet shell will have direct contact with the hot bubble and sweep up some of the material in this bubble. The composition of the material in the bubble varies over time, depending on which winds have fed material into the bubble up to that moment.

The ionization of the material depends on both the temperature and the number of ionizing photons. Unlike in the 40 $M_\odot$ case (See Paper I), the 60 $M_\odot$ star always produces a large number of highly energetic photons, which means that photo-ionization will always play an important role. The hot bubbles that drive shells, have a very high temperature ($T \geq 10^6$ K). The shells are less hot, since their high density causes them to cool down effectively through radiative energy loss. After a supernova, and especially after a gamma-ray burst, the degree of ionization will be even higher, since such events produce a massive amount of high energy radiation, which will pass through and ionize the circumstellar bubble.

5.7 The absorption features during the LBV and Wolf-Rayet phase

The result of the calculations described in section 5.5 can be seen in Fig. 5.5. Compared to the absorption spectrum of a 40 $M_\odot$ star it is clear that a 60 $M_\odot$ star produces more time-dependent features.

5.7.1 The number of visible absorption features

The number of absorption lines that are visible changes with time. For the moment we shall ignore the dependence on the viewing angle of many absorption features, and look only at the general evolution. During the main sequence only the zero velocity component and the main sequence wind are visible. Although the main sequence shell has a distinct radial velocity, this is too small to be observed independently. Once the LBV phase starts,

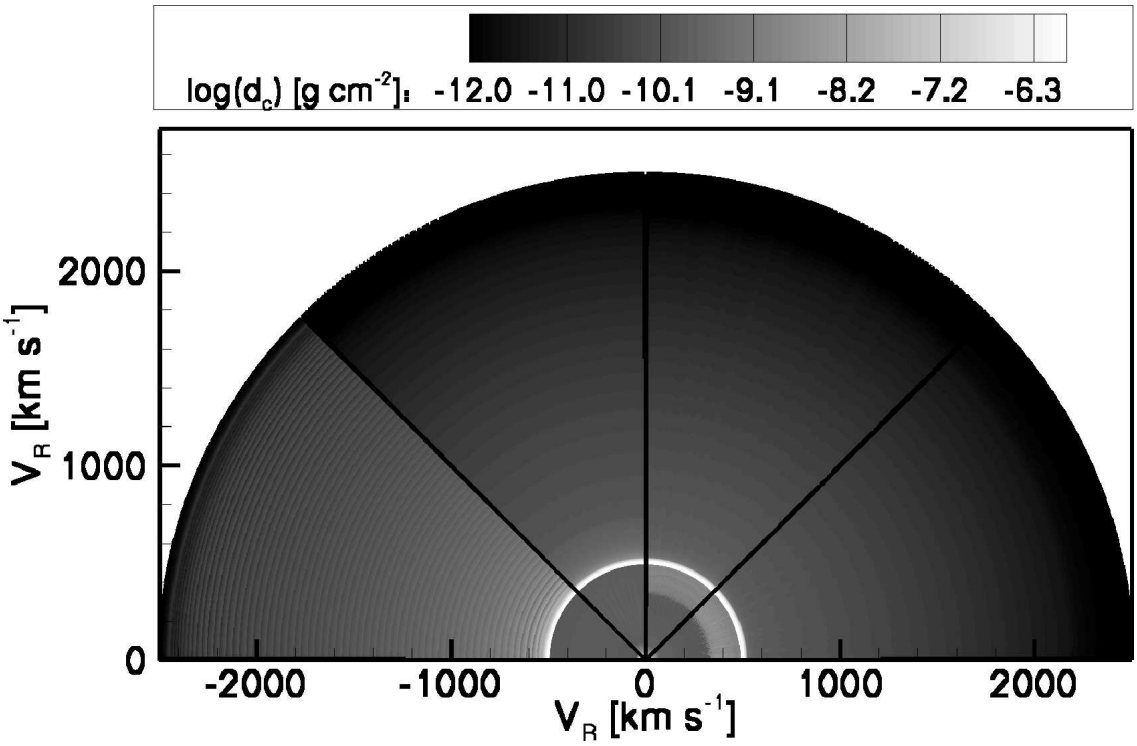

Figure 5.7: The column density as a function of radial velocity at the same moments in time as the density plot in figure 5.2. The LBV wind (490 km s^{-1}) is clearly visible at all times. The LBV shell ($\sim$ 350 – 450 km s^{-1}) appears later. Once it appears it can be observed at any angle.

two new features are created. The LBV wind itself, which moves outward at a velocity of 490 km s^{-1} and the shell driven by the LBV wind, moving at ca. 400 km s^{-1}. It takes some time to create this shell, since the slow LBV wind has to travel outward to the wind termination shock

As the star enters the Wolf-Rayet phase, two more features are added. The Wolf-Rayet wind, moving at 2250 km s^{-1} and the Wolf-Rayet wind driven shell, which moves at ca. 800 km s^{-1}. This means, that during the WR1 (see section 5.4), a total number of five independent absorption features is visible (Wolf-Rayet wind, the remnant of the LBV wind, two shells and the zero velocity component), even if we ignore the effects of instabilities in the shell. As the Wolf-Rayet shell expands outward, the size of the free streaming LBV wind region decreases, so the LBV wind absorption component starts to disappear. Once the Wolf-Rayet shell reaches the LBV shell, the two shells collide and both disappear as independent features. The remnants of the shell are fragmented and together with the interaction between the Wolf-Rayet wind and the hot bubble create a new shell, with a velocity of ca. 600 km s^{-1}. This will last throughout WR2, which consequently shows three absorption components. The Wolf-Rayet wind, the shell and the zero velocity component. The period from the beginning of the LBV phase to the end of WR2, which shows the greatest time dependence can be seen in more detail in Fig. 5.6.

Once the shell fragments collide with the edge of the bubble, they dissipate and disappear as absorption features. The circumstellar medium now enters the final phase: WR3. Only two absorption features remain, the Wolf-Rayet wind and the zero velocity component.

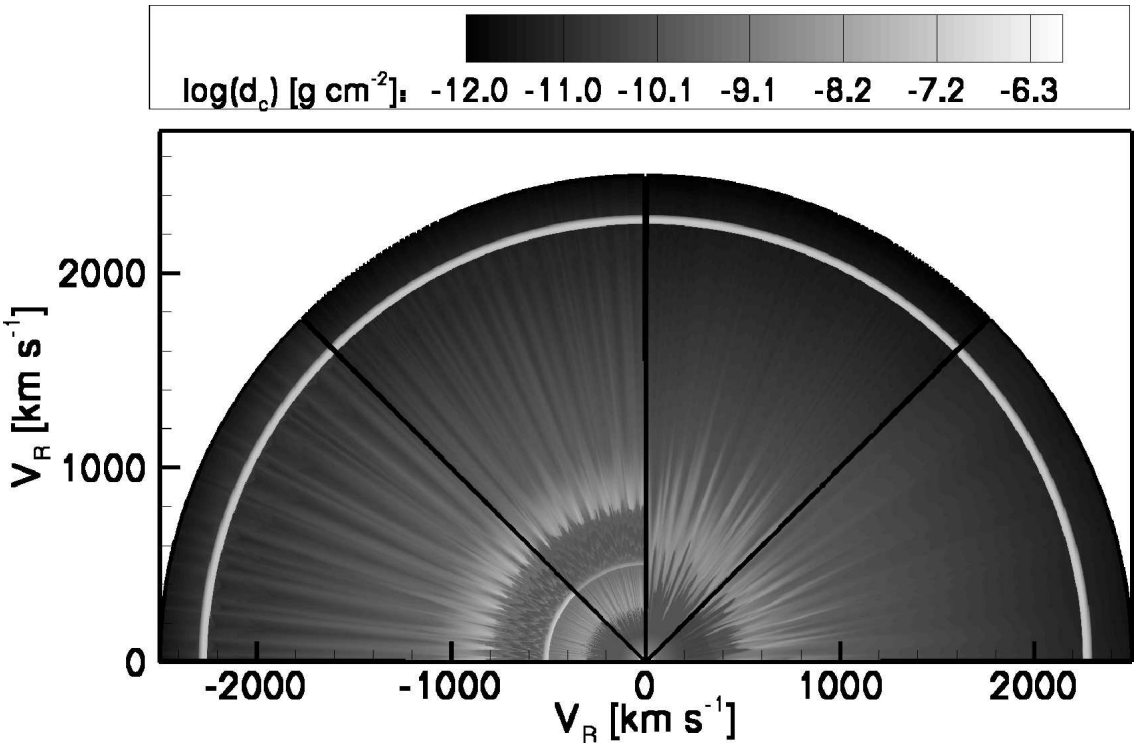

Figure 5.8: Similar to Fig. 5.7, this shows the column densities at the same moments in time as the density plot in figure 5.3. The Wolf-Rayet wind (2250 $\mathrm{km\,s^{-1}}$) and the Wolf-Rayet shell (800 $\mathrm{km\,s^{-1}}$)can be clearly observed in the first two frames. The third and forth frame show the column densities after the collision of the two shells. The LBV wind and shell are gone, as is the Wolf-Rayet shell. A new shell at ca. 600 $\mathrm{km\,s^{-1}}$ is formed from the fragments of the two shells.

5.7.2 Absorption features in the line of sight

Which and how many independent absorption features are visible within the line of sight depends on angle as well as time. The narrow lines resulting from free-streaming winds are visible at any angle. The broader lines that result from the shells and shell fragments are angle-dependent since the density of the shell is not constant.

In Fig. 5.7, 5.8 and 5.9 we show the angle dependence of the absorption features during the LBV and Wolf-Rayet phase. The segments shown correspond to the segments in Fig. 5.2, 5.3 and 5.4. During the very early stages of the LBV phase, only the LBV wind itself is visible. Once the LBV wind reaches the wind termination shock, it will form the LBV shell, which then becomes visible as an absorption feature (Fig. 5.7). The LBV shell ($\sim 350 - 400\,\mathrm{km\,s^{-1}}$), though unstable, is not fragmented too severely and can usually be observed at most angles.

The start of the Wolf-Rayet phase can be seen in Fig. 5.8, which shows the column density during the transition from WR1 to WR2 (section 5.4). The Wolf-Rayet shell ($\sim 800\,\mathrm{km\,s^{-1}}$) becomes visible as an absorption feature as soon as the Wolf-Rayet wind ($2250\,\mathrm{km\,s^{-1}}$) starts. The WR shell is somewhat more fragmented, so the likelihood of observing this shell is smaller, but still quite large. After the collision the fragments of the two shells form a new shell at ca. 600 $\mathrm{km\,s^{-1}}$. Angle dependence increases considerably after the collision of the two shells, as the fragments tend to shrink. (The higher the local density, the more effective the radiative cooling. Therefore, the high density fragments

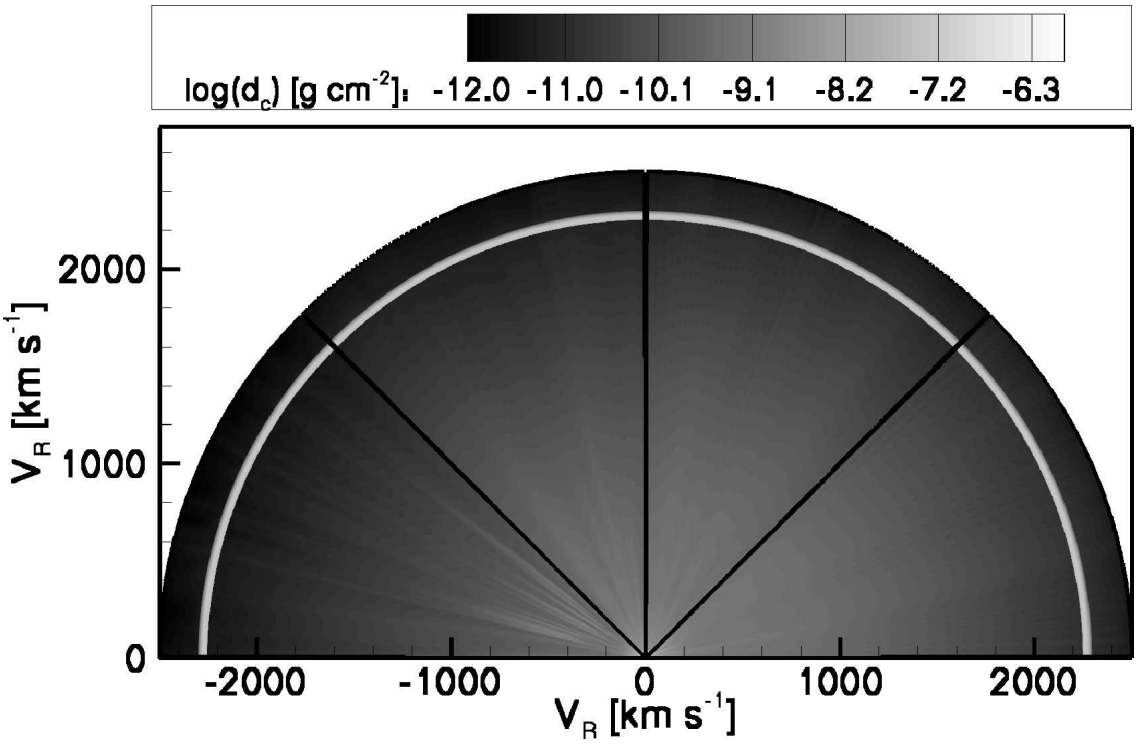

Figure 5.9: The column density of the circumstellar medium at the same time as Fig. 5.4. In the first frame, the remnants of the shells can still be seen as independent blobs (the column density varies considerably with the angle). Once they have collided with the edge of the bubble, they slow down and spread out in angular direction. They will no longer show up as independent absorption features.

will have a low thermal pressure, which causes them to shrink even further.) As we saw in Paper I, fragmentation of a shell can both decrease and increase the number of independent velocity features seen in a single line of sight. If no shell fragment is present along that line, no absorption line is visible. However, it is also possible that several fragments, with different individual velocities, are present along the same line, causing multiple absorption features to appear. Generally speaking, angle dependence plays a smaller role in the case of a 60 $M_\odot$ star than in the case of a 40 $M_\odot$ star, since the shells around the more massive star are less fragmented.

Once the shell fragments collide with the edge of the hot bubble, they cannot travel further outward and will instead spread out in the angular direction as can be seen in Fig. 5.9. Since their radial velocity decreases, they will no longer show up an independent line. During the final stages of the Wolf-Rayet phase (WR3) only the Wolf-Rayet wind itself and the zero velocity component remain visible.

5.8 Discussion and conclusions

We have computed the column density evolution created by the circumstellar medium around a 60 $M_\odot$ star, which was found to be highly time-dependent. In comparison with the absorption lines observed in the afterglow spectrum of GRB 021004, the predicted radial velocities of the absorption features seem rather large. However, there is a consid-

erable uncertainty in our model, since the velocity of the LBV wind is difficult to predict. We have adopted the escape velocity at the surface of the star as the LBV wind speed, which is reasonable for a line-driven wind. However, the mechanism that drives the LBV wind is not entirely clear and it is quite possible that the wind velocity is considerably lower (García-Segura et al. [24] found velocities as low as 200 $\mathrm{km\,s^{-1}}$ for the LBV wind). If the LBV wind has a lower velocity, so does the LBV shell, which is driven by this wind. The Wolf-Rayet shell, which has to sweep up the LBV wind, will be similarly affected. The intermediate velocity (300...1000 $\mathrm{km\,s^{-1}}$) absorption features only appear during the early Wolf-Rayet period and disappear approximately 50 000 years after the start of the Wolf-Rayet phase. the appearance of absorption lines at these velocities in the afterglow spectrum of GRB 021004 may indicate that the explosion took place during the early Wolf-Rayet stage.

However, such an early explosion is unlikely for a 60 $\mathrm{M_\odot}$ star, as high mass stars, which pass through an LBV period, typically have a Wolf-Rayet phase of at least 200 000 years. A lower mass ($\sim 30\,\mathrm{M_\odot}$) star, as described in Paper I, would seem to be a more likely candidate. The large number of absorption features at intermediate velocities would then be explained by the presence of several shell fragments in the line of sight. A second possibility is that the progenitor of GRB 021004 was in fact part of a close binary, which went through a late mass-transfer phase. During mass transfer, which lasts approximately 10 000 years, the stellar wind parameters resemble those of the wind of an LBV star. The mass donor star is stripped of its outer layers, so that only a Wolf-Rayet star remains (Petrovic et al. [52]). This star will only have a short Wolf-Rayet phase left. It may even be so short, that the LBV wind and LBV shell are still visible when the supernova occurs, which can account for the presence of a large number of intermediate velocity absorption lines without the need of multiple fragments of the same shell within the line of sight.

In paper I, we presented a scenario for the formation of the absorption lines in the spectrum of the afterglow of GRB 021004 based on the evolution of a 40 $\mathrm{M_\odot}$ star. The large number of absorption lines at intermediate velocities was explained in that case by the presence of multiple shell fragments in a line of sight. While possible, the occurrence of such a situation is not very likely. Nevertheless, the necessity of a short Wolf-Rayet period makes it a better progenitor candidate for GRB 021004 than the 60 $\mathrm{M_\odot}$ star that we present here. The assumption that stars of 40 $\mathrm{M_\odot}$ or less can be gamma-ray burst progenitors is confirmed by observations of those gamma-ray bursts that can be linked to supernova explosions. For SN 1998bw, which is identified as the supernova corresponding to GRB 980425 the initial mass of the star is considered to be ≤ 40 $\mathrm{M_\odot}$ (Iwamoto et al. [32]; Woosley et al. [85] and Nakamura et al. [48]). Since GRB 980425 is not a typical gamma-ray burst, this can not serve as a general example, but Mazzali et al. [42] give a similar result (30...40 $\mathrm{M_\odot}$) for SN 2003dh, which corresponds to GRB 030329. Finally, SN 2003lw, which is linked to GRB 031203, is thought to have a progenitor mass on the main sequence of 40...50 $\mathrm{M_\odot}$ (Mazzali et al. [43]). This would make the stars somewhat larger than we expect, but it would still follow an evolutionary path similar to our 40 $\mathrm{M_\odot}$ star model, rather than become an LBV star. In other words, all gamma-ray bursts that have been linked to supernova explosions so far seem to have a progenitor mass on the main sequence of less than 50 $\mathrm{M_\odot}$ (see also della Valle [14]).

If the progenitor mass of GRB 021004 is larger, the presence of the intermediate velocity lines in the afterglow spectrum can only be explained as the result of binary evolution.

Acknowledgements

We would like to thank Ralph Wijers, Rhaana Starling, Klaas Wiersema and Alexander van der Horst of the Astronomical Institute Anton Pannekoek of the University of Amsterdam for their information on the spectrum of the afterglow of GRB 021004.
This work was sponsored by the Stichting Nationale Computerfaciliteiten (National Computing Facilities Foundation, NCF), with financial support from the Nederlandse Organisatie voor Wetenschappelijk Onderzoek (Netherlands Organization for Scientific research, NWO). This research was done as part of the AstroHydro3D project:
(http://www.strw.leidenuniv.nl/AstroHydro3D/)

6

On the formation of a constant density medium close to the progenitor of a Gamma-Ray Burst

A. J. van Marle, N. Langer, A.Achterberg and G. García-Segura
To be submitted toAstronomy & Astrophysics

Abstract

We explore various possible ways to form a constant density medium close to a Wolf-Rayet star by the time it explodes and may give rise to a Gamma-Ray Burst, (GRB). An analysis of the light curves of Gamma-Ray Burst afterglows shows that this is a common occurrence ($\geq$ 25 percent). The favoured explanation is that the wind termination shock of these stars lies very close to the star. This being the case, the relativistic jet of the GRB expands into the shocked wind material, which has a nearly constant density, rather than into the free-streaming wind in which the density falls off with increasing distance. However, for a typical Wolf-Rayet star the distance between the progenitor star and the wind termination shock is much too large. We have investigated a number of scenarios that may lead to a smaller distance between the Wolf-Rayet star and the wind termination shock: A high density or a high pressure in the surrounding interstellar medium (ISM), a weak Wolf-Rayet star wind, the presence of a binary companion, or fast motion of the Wolf-Rayet star relative to the ISM. While none of these scenarios is likely to explain all the occurrences of constant density in GRB afterglows, a high ISM density, stellar motion, or both, especially when combined with a relatively low ram pressure of the Wolf-Rayet wind seem to be the most likely explanations. A low ram pressure of the Wolf-Rayet wind is helpful in all cases. Therefore we conclude, that the progenitors of GRBs that show a constant density medium in the afterglow are most likely low metallicity stars. As low metallicity stars typically have weak winds.

6.1 Introduction

During their evolution, massive stars lose a major fraction of their mass in the form of a stellar wind. The interaction between this stellar wind and the surrounding interstellar medium creates a circumstellar bubble. Within approximations, the morphology and evolution of such bubbles can be predicted using an analytical approximation (Castor et al. [7]; Weaver et al. [79]; Ostriker & McKee [49]), or by numerical simulations (García-Segura et al. [24], [25]; Freyer et al. [20]; van Marle et al. [72], [73], [74]). In Fig. 6.1 we show the typical morphology of a spherically symmetric circumstellar bubble. Closest to the star we find the free-streaming stellar wind. The free-streaming wind material hits the wind termination shock, where the directed kinetic energy of the the wind material thermalizes, creating a 'hot bubble' of shocked wind material. Outside the hot bubble lies a shell of shocked interstellar gas that has passed through the outer shock that bounds the bubble as long as it expands supersonically with respect to the interstellar medium (ISM). The material forming this shell is swept up as the extremely high-pressure gas of the hot bubble expands. Finally, there is the ambient medium, which has not yet been overrun by the expanding circumstellar bubble.

Wolf-Rayet stars, which form the final evolutionary stage of massive stars, are thought to be the progenitors of long Gamma-Ray Bursts (GRBs). Long GRBs are thought to occur when a jet, formed near the collapsed core of such a massive star, breaks out of the (still infalling) stellar envelope. This relativistic jet will expand info the circumstellar medium (CSM). On its way it should first encounter the free-streaming wind of the Wolf-Rayet star, followed by the shocked wind material and the shocked interstellar matter. Finally the jet propagates into the ISM.

It is possible to derive the density profile of the CSM from the light curve of the GRB afterglow. The medium close to a Wolf-Rayet star has a density profile of a free-streaming wind with a total mass flux $\dot{M}$ and velocity $V_{\rm w}$:

$$\rho_{\rm w}(r) \sim \frac{\dot{M}_{\rm w}}{4\pi r^2 V_{\rm w}(r)} \,. \tag{6.1}$$

The wind density decays as $\rho_{\rm w} \propto r^{-2}$ sufficiently far from the star, when the wind has reached its terminal velocity. Both analytical and numerical calculations suggest that the free wind of a Wolf-Rayet star extends over a radius of the order of 10 pc. However, from the analysis of many GRB afterglows one infers a *constant* density rather than relation (6.1) (See: Chevalier & Li [9]; Panaitescu & Kumar [50]; Panaitescu & Kumar, [51]; Chevalier et al. [10]; Zeh et al. [89]).

The percentage of GRBs that show a constant density profile varies, depending on the afterglow model, but it can be estimated as ≥ 25 percent. Moreover, all studies mentioned so far are limited to GRBs detected before the launch of the SWIFT satellite. They are primarily concerned with GRBs at low redshift. In this paper we explore various possibilities for the occurrence of a constant-density medium close to a Gamma-Ray Burst progenitor.

The density of the CSM and its radial dependence is also of importance for the use of Gamma-Ray Bursts as standard candles in cosmological studies. For these calculations, the correlation between peak energy and corrected collimated energy has to be calculated, and the relationship between these quantities depends on the nature of the circumstellar and interstellar medium. (See: Ghirlanda et al. [27])

This article is organized as follows:
In Sect. 6.2 we use an analytic approximation to determine at what radius the constant density medium needs to occur in order to show up in the GRB afterglow light curve. In Sects. 6.3 and 6.4 we explore a number of possible explanations for the location of a constant density medium at such a small radius, using both analytical and numerical techniques to model the circumstellar medium. Finally, in Sect. 6.5 we discuss which explanations are most likely.

6.2 The location of a constant density medium

While the region closest to the Wolf-Rayet star has a density that decreases with the radius squared, the next layer of the circumstellar bubble (region B in Fig. 6.1) does indeed have a nearly constant density, essentially since the high sound speed inside this material precludes the occurrence of large pressure- and density-gradients. This hot bubble of shocked wind gas drives a shell into the CSM (Weaver et al. [79]). It has been proposed (Wijers et al. [81]; Chevalier et al. [10]) that the GRB afterglows are created while the jet moves through this medium. This would require the Gamma-Ray Burst jet to cross the wind termination shock at a very early stage. In their models, Chevalier et al. [10] find that the start of a constant-density medium occurs at less than 1 pc from the GRB progenitor. Unfortunately, the wind termination shock that separates this bubble from the free-streaming wind is located typically at a distance of 10 pc or more from the star, which would make this scenario impossible. The location of this shock is at the radius where the ram pressure of the wind matches the thermal pressure in the hot bubble. Since

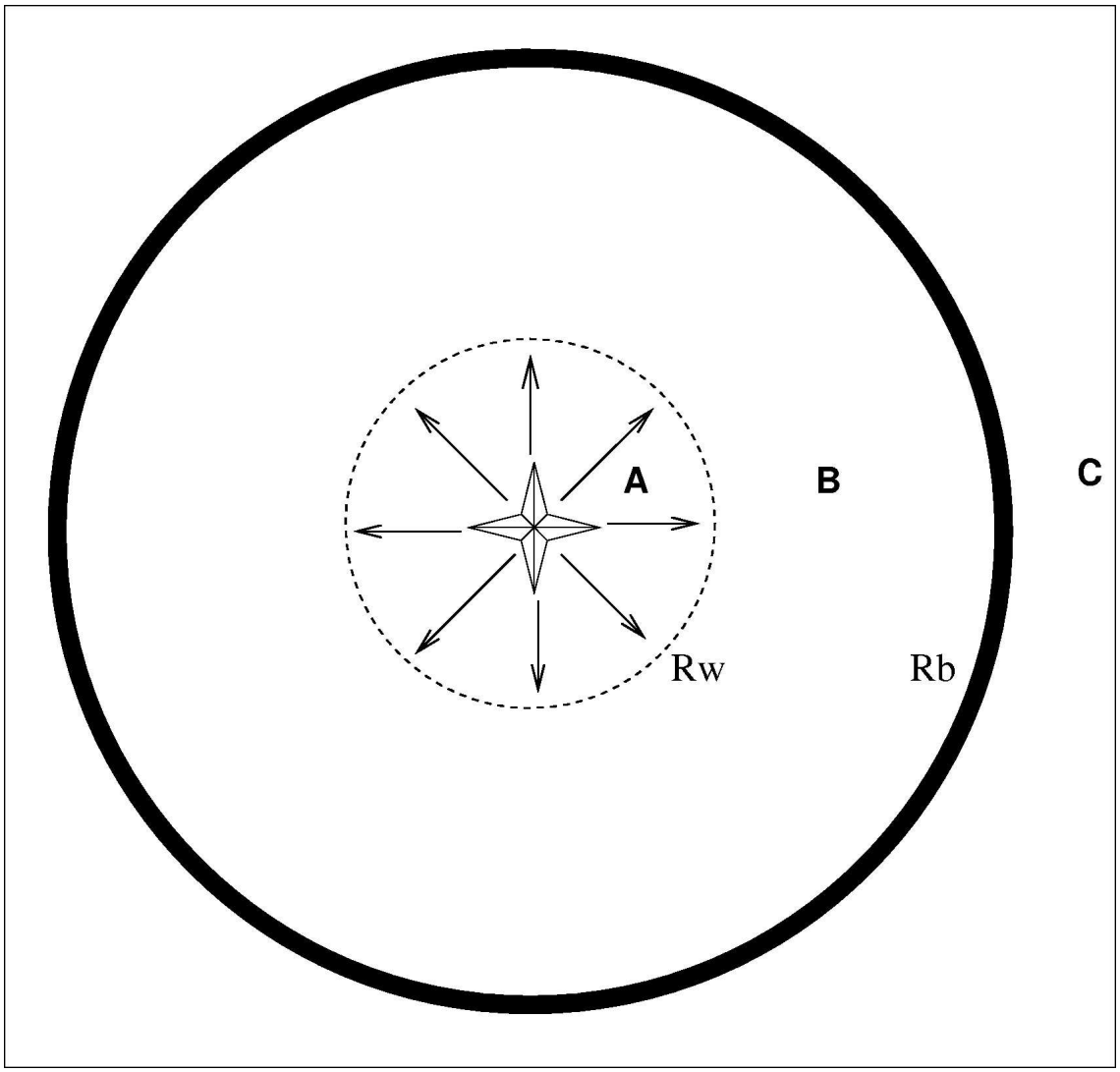

Figure 6.1: Schematic view of a circumstellar bubble (not to scale). The free-streaming stellar wind (region A) passes through the wind termination shock R_w (dashed line) to enter the hot bubble of shocked wind material (region B). The high thermal pressure in the hot bubble sweeps up a shell (thick, continuous line) of radius R_b, which expands into the ISM (region C).

Wolf-Rayet stars have a strong wind, with both a high mass loss rate and a high terminal velocity, the ram pressure of the wind is considerable. Typically, this places the wind termination shock at a large distance from the star.

6.2.1 The location of the wind termination shock

The location of the wind termination shock can be calculated analytically, using the so-called thin-shell approximation (Castor et al. [7]; Weaver et al. [79]; Ostriker & McKee [49]). This does not take the effect of radiative cooling into account, but it serves as a good first approximation. The mechanical luminosity of the star,

$$L_w = \frac{1}{2} \dot{M}_w V_w^2 , \tag{6.2}$$

is a measure for the mechanical energy that the star puts into the CSM. For a given mechanical luminosity, it is possible to calculate the thermal pressure in the bubble as a function of time, by balancing the pressure in the hot, shocked wind with the ram pressure $\rho_0(\mathrm{d}R_\mathrm{b}/\mathrm{d}t)^2$ due to the expansion into a constant-density ISM with mass density ρ_0 (Weaver et al. [79]):

$$P_\mathrm{b} = \frac{7}{(3850\pi)^{2/5}} L_\mathrm{w}^{2/5} \rho_0^{3/5} t^{-4/5}. \tag{6.3}$$

This calculation assumes that the ISM is cold, so that it has no significant thermal pressure. Since the mechanical luminosity of the star can change considerably over time, we have to take the average value for the mechanical luminosity.

The wind termination shock is located at the radius R_w such that the thermal pressure in the shocked wind material is equal to P_b. The post-termination shock pressure is roughly equal to the ram pressure in the wind,

$$P_\mathrm{ram} = \rho_\mathrm{w} V_\mathrm{w}^2 = \left(\frac{\dot{M}_\mathrm{w} V_\mathrm{w}}{4\pi r^2}\right). \tag{6.4}$$

Combining Eqs. 6.3 and 6.4 gives the radius of the wind termination shock:

$$\begin{aligned} R_\mathrm{w} &= \left(\frac{\dot{M}_\mathrm{w} V_\mathrm{w}}{4\pi P_\mathrm{b}}\right)^{1/2} \\ &= \left(\frac{\dot{M}_\mathrm{w} V_\mathrm{w}}{28}\right)^{1/2} \left(\frac{3850}{\overline{L_\mathrm{w}}}\right)^{1/5} \frac{t^{2/5}}{(\pi\rho_0)^{3/10}}. \end{aligned} \tag{6.5}$$

Here the mass loss rate ($\dot{M}_\mathrm{w}$) and wind velocity (V_w) are time dependent, while $\overline{L_\mathrm{w}}$ is the average mechanical luminosity over the entire evolution of the star up to that moment.

If the ram pressure of the wind changes, then the radius of the wind termination shock will change on a time scale that is equal to the hydrodynamical time scale of the hot bubble. Since the temperature in the hot bubble is of the order of 10^7 K, and since the radius of the bubble is approximately 20..50 pc, (García-Segura et al. [24], [25]; Freyer et al. [20]; van Marle et al. [74]), this gives us a hydrodynamical timescale of the order of $1...4\times10^4$ years. This means that the wind termination shock will generally closely follow the changes in the wind parameters due to stellar evolution. The time dependence of the thermal pressure in the bubble is not very important, since we only consider the Wolf-Rayet period, which in the case of most massive stars is less than 10 percent of the total lifespan of the star.

6.2.2 Afterglow production in a free wind

In order to establish a maximum radius for the wind termination shock in those cases where a constant-density circumstellar medium is inferred, we must first calculate the typical distance of the jet from the progenitor star when the afterglow is produced. The afterglow of a GRB is believed to be synchrotron radiation, produced when the jet produces a relativistic shock in the surrounding medium. For a constant-density medium to show up in the afterglow light curve, the jet must still be relativistic when it passes through the wind termination shock.

We consider an extremely powerful fireball with an explosion energy $E_{\rm GRB} \simeq 10^{52}...10^{54}$ erg, and with a small mass loading in the form of baryons: $M_{\rm GRB}({\rm baryonic}) \leq 10^{-4}...10^{-5}$ $M_\odot$. Note that $E_{\rm GRB}$ is the energy of the fireball for a spherical explosion. The actual energy of the jet can be much lower, depending on the opening angle. A jet confined to a solid angle $\Omega_{\rm j}$ carries an energy $E_{\rm j} \sim E_{\rm GRB} \times (\Omega_{\rm j}/4\pi)$ and a mass $M_{\rm j} \sim M_{\rm GRB} \times (\Omega_{\rm j}/4\pi)$.

As the total explosion energy is significantly larger than the rest energy of the ejected mass,

$$E_{\rm GRB} \gg M_{\rm GRB}c^2, \tag{6.6}$$

the material in the blast wave (or jet) will expand rapidly, moving with a speed $v_{\rm s} \approx c$ and with a corresponding bulk Lorentz-factor:

$$\Gamma_{\rm s} \equiv \frac{1}{\sqrt{1 - v_{\rm s}^2/c^2}} \gg 1. \tag{6.7}$$

During the initial phase of the expansion, the explosion energy $E_{\rm GRB}$ is converted by pressure forces into the bulk motion of the material. Once the initial energy released by the GRB has been converted into bulk kinetic energy, the Lorentz-factor is determined solely by the ratio between the explosion energy and the rest-mass energy (see the review by Piran, [54], and references therein):

$$\Gamma_{\rm s} \approx \eta \equiv \frac{E_{\rm GRB}}{M_{\rm GRB}c^2}. \tag{6.8}$$

This relation will hold until the jet has swept up a sufficient amount of mass (see below), or until (in the case of a jet) sideways expansion becomes important. In order to explain the observations, we need $\eta \simeq 100...1000$ (Thompson [69]).

During the expansion, the blast wave sweeps up material which passes through a relativistic shock. The total energy of the system, consisting of the original mass and radiation liberated at the GRB and the swept-up mass, approximately equals

$$E_{\rm GRB} \approx \Gamma_{\rm s}\, M_{\rm GRB}c^2 + (\Gamma_{\rm s}^2 - 1)\, M_{\rm sw}c^2. \tag{6.9}$$

The second term is the total (internal) energy of the shocked, swept-up mass. For $\Gamma_{\rm s} \gg 1$ this term follows from the jump conditions for an ultra-relativistic shock (Blandford & McKee, [2]) which give the post-shock energy density as $e_2 \sim \Gamma_{\rm s}^2 \rho_1 c^2$ where the subscript 1 (2) refers to the pre-shock (post-shock) state, and where ρ_1 is the rest mass density in front of the shock. For a non-relativistic shock with velocity $V_{\rm s}$ the classical Rankine-Hugoniot relations give $e_2 \approx \rho_1 V_{\rm s}^2$. The second term in expression (6.9) correctly interpolates between these two limiting cases, up to factors of order unity. $E_{\rm GRB}$ is conserved as long as radiation losses can be neglected.

In the limit $\Gamma_{\rm s} \gg 1$ one can write:

$$E_{\rm GRB} = \Gamma_{\rm s}\, M_{\rm GRB}c^2 + \Gamma_{\rm s}^2\, M_{\rm sw}c^2. \tag{6.10}$$

The free expansion phase, where $\Gamma_{\rm s} \sim E_{\rm GRB}/\, M_{\rm GRB}\, c^2 \sim$ constant, ends when the energy contained in the shocked, swept-up mass becomes comparable with the energy of the original explosion:

$$\Gamma_{\rm s}\, M_{\rm GRB}c^2 \simeq \Gamma_{\rm s}^2\, M_{\rm sw}c^2, \tag{6.11}$$

which is satisfied when:

$$M_{\rm sw} \simeq \frac{M_{\rm GRB}}{\Gamma_{\rm s}} \simeq \frac{M_{\rm GRB}}{\eta} = \frac{E_{\rm GRB}}{\eta^2 c^2} \equiv M_{\rm d}, \tag{6.12}$$

which defines the deceleration mass $M_{\rm d}$. The blast wave or jet will decelerate when $M_{\rm sw} > M_{\rm d}$. Taking the simple case of a spherical blast wave expanding into a freely expanding stellar wind, with density profile (6.1) and constant $V_{\rm w}$, the swept-up mass when the fireball has expanded to a radius $R_{\rm s}$ equals

$$M_{\rm sw} = \frac{\dot{M}_{\rm w}\, R_{\rm s}}{V_{\rm w}}. \tag{6.13}$$

Combining relations (6.12) and (6.13) one finds the *deceleration radius*, the radius where the free expansion of the blast wave stops, provided this occurs while still in the free-wind region:

$$R_{\rm d} = \frac{M_d\, V_{\rm w}}{\dot{M}_{\rm w}} \simeq \frac{E_{\rm GRB}\, V_{\rm w}}{\eta^2\ \dot{M}_{\rm w} c^2}. \tag{6.14}$$

The blast wave now enters the relativistic equivalent of the well-known decelerating Sedov-Taylor expansion, until the expansion speed becomes sub-relativistic. After that, it enters the ordinary Sedov-Taylor expansion phase until radiation losses become important, invalidating the assumption of the conservation of the total energy (6.9). During the Sedov-Taylor phase, the swept-up mass dominates the energy equation, so that:

$$E_{\rm GRB} = \Gamma_{\rm s}^2 M_{\rm sw}\, c^2\ . \tag{6.15}$$

As long as the blast wave stays in the free wind, relation (6.13) remains valid, and one has:

$$\Gamma_{\rm s} \approx \sqrt{\frac{E_{\rm GRB}\, V_{\rm w}}{\dot{M}_{\rm w} c^2\, R_{\rm s}}} = \left(\frac{R_{\rm s}}{R_{\rm d}}\right)^{-1/2}\ , \tag{6.16}$$

where we have used Eqn. 6.14. We can take the point where $\Gamma_{\rm s} \approx 1$ as the point where the blast wave becomes non-relativistic, This happens at the so-called *Sedov-Taylor radius* $R_{\rm ST}$, which in a free wind equals:

$$R_{\rm ST} \equiv \eta^2\, R_{\rm d} = \frac{E_{\rm GRB}\, V_{\rm w}}{\dot{M}_{\rm w} c^2}\ . \tag{6.17}$$

For $R_{\rm s} > Rst$ one has from (6.9) with $\Gamma_{\rm s}^2 - 1 \approx V_{\rm s}^2/c^2$:

$$\frac{V_{\rm s}}{c} \sim \left(\frac{R_{\rm s}}{R_{\rm ST}}\right)^{-1/2} \tag{6.18}$$

for as long as the expansion proceeds in the free-wind region ($R_{\rm s} < R_{\rm w}$).

For a typical Wolf-Rayet wind one has: $E_{\rm GRB} = 5.0 \times 10^{52}$ erg, $V_{\rm w} = 2000$ km s^{-1} and $\dot{M}_{\rm w} = 3.0 \times 10^{-5}$ M$_\odot$ yr^{-1}. This gives us $Rst \sim 1.9$ pc, well within the free-wind region of the circumstellar bubble. This is the radius at which the production of the afterglow radiation is expected to end. In order to get a constant density medium during afterglow

production, the wind termination shock has to lie much closer to the star, typically at ~ 0.1 pc (Chevalier et al. [10]). If the entire afterglow shows a constant density medium, the jet has to pass the wind termination shock before it starts to decelerate. In other words, before the end of the free expansion phase. The transition from free expansion to the relativistic Sedov-Taylor phase takes place at radius $R_{\rm d}$ (Eqn. 6.14). With the values quoted above, and for $\eta = 100$, the deceleration radius equals $R_{\rm d} = R_{\rm ST}/\eta^2 \sim 2 \times 10^{-4}$ pc. In Section 3 we will consider various possibilities for placing the wind termination shock this close to the star.

6.2.3 Confining pressure

The critical factor in bringing the wind termination shock closer to the star is the confining pressure of the surrounding medium. The pressure force constrains the expansion and size of the free-streaming wind region. The nature of this confining pressure depends on the circumstances. For instance, in the scenario described in Sect. 6.2.1 it is the thermal pressure in the bubble of shocked wind material, which in turn equals the ram pressure of the ISM associated with the overall expansion of the circumstellar bubble. For a rapidly moving star, it equals the ram pressure of the ISM associated with the stellar motion. One can generalize Eq. 6.5 to:

$$R_{\rm w} = \left(\frac{\dot{M}_{\rm w} V_{\rm w}}{4\pi P_{\rm cf}} \right)^{1/2}, \tag{6.19}$$

with $P_{\rm cf}$ the confining pressure.

If we stipulate that the GRB jet has to pass the wind termination shock before it enters the non-relativistic Sedov-Taylor expansion phase, this means that $R_{\rm ST} \geq R_{\rm w}$. Combining Eqs. 6.17 and 6.19 yields:

$$E_{\rm GRB} \geq \frac{\dot{M}_{\rm w} c^2}{V_{\rm w}} \left(\frac{\dot{M}_{\rm w} V_{\rm w}}{4\pi P_{\rm cf}} \right)^{1/2}. \tag{6.20}$$

Therefore, the confining pressure must satisfy:

$$P_{\rm cf} \geq \frac{c^4 \dot{M}_{\rm w}^3}{4\pi E_{\rm GRB}^2 V_{\rm w}}. \tag{6.21}$$

For the typical Wolf-Rayet wind values given in Sect. 6.2.2 and for $E_{\rm GRB} = 2 \times 10^{52}$ erg, this gives a confining pressure equal to: $P_{\rm cf} \simeq 1.8 \times 10^{-9}$ dyne cm^{-2}.

If, on the other hand, we demand that the jet has to pass through the wind termination shock even before it has started to decelerate, we get $R_{\rm d} \geq R_{\rm w}$. This would have the advantage that the entire afterglow is generated in the constant density medium, but this situation is much more difficult to bring about. From the relationship between $R_{\rm ST}$ and $R_{\rm d}$ (Eq. 6.17) we find that the confining pressure now must satisfy:

$$P_{\rm cf} \geq \frac{\eta^4 c^4 \dot{M}_{\rm w}^3}{4\pi E_{\rm GRB}^2 V_{\rm w}}. \tag{6.22}$$

Since $\eta > 100$, the confining pressure becomes extremely large: $P_{\rm cf} \simeq 1$ dyne cm^{-2} for typical parameters. Such a large confining pressure is almost impossible to create. For instance, the thermal pressure of a static gas is equal to:

$$P = 1.38 \times 10^{-16}\, n\, T, \tag{6.23}$$

GRB name	redshift	E_{iso} ($\times 10^{52}$ erg)	density profile
GRB 970228	0.695	$2.68^{(5)}$	$w^{(1)}$
GRB 970508	0.835	$0.985^{(5)}$	$w^{(1,3,4)}$
GRB 980703	0.966	$8.09^{(5)}$	$u^{(2)}$
GRB 990123	1.60	$232^{(5)}$	$c^{(1,2,3,4)}$
GRB 990510	1.619	$21.9^{(5)}$	$c^{(1,2,3,4)}$
GRB 991208	0.706	$18.6^{(5)}$	$u^{(2)}$, $w^{(3,4)}$
GRB 991216	1.02	$7.83^{(5)}$	$w^{(3)}$
GRB 000301C	2.03	$6.35^{(5)}$	$u^{(3,4)}$
GRB 000418	1.118	$11.6^{(5)}$	$w^{(3,4)}$
GRB 000926	2.066	$45.6^{(5)}$	$c^{(3,4)}$
GRB 010222	1.477	$154^{(6)}$	$w^{(3)}$, $u^{(4)}$
GRB 011121	0.36	$11^{(6)}$	$w^{(4)}$
GRB 020405	0.69	$7.37^{(7)}$	$w^{(4)}$
GRB 021004	2.3	$2.2^{(8)}$	$w^{(4)}$
GRB 021211	1.01	$0.61^{(6)}$	$w^{(4)}$

Table 6.1: This table gives the redshift end isotropic energy for a number of GRBs as well as the density profile (w=wind, c=constant, u=undecided) of the circumstellar medium. If the density profile is marked as undecided, this means, that both a wind and constant density profile are possible. Clearly, the number of GRB afterglows which show a constant density medium are a minority. Sources for the density profiles are:(1) Chevalier & Li[9], (2) Panaitescu & Kumar [50], (3) Panaitescu & Kumar [51] and (4) Chevalier et al [10]. The redshifts were taken from the table at: http://www.mpe.mpg.de/~jcg/ maintained by J. Greiner. The values for the isotropic energy come from (5) Bloom et al. [3]; (6) Amati [1], (7) Price et al. [57] and (8) Holland et al. [29].

with n the particle density. So, for a particle density of 100 000 particles cm^{-}2, which is already extremely high, we would need a temperature of approximately 10^{12} K. It is clearly not realistic to demand that the wind termination shock lies within the deceleration radius. In a similar fashion, if the confining pressure is a ram pressure,

$$P = \rho V^2 = 1.67 \times 10^{-8}\, n \left(\frac{V}{1000\,\mathrm{km/s}}\right)^2 , \tag{6.24}$$

it would require a large density in combination with a large velocity in order to achieve such a large value. Therefore, we will limit our discussion to the weaker condition (6.21), placing the termination shock radius well within the radius for non-relativistic Sedov-Taylor expansion.

6.2.4 Results from afterglow models

The distance a GRB blast wave or jet will travel before it starts to decelerate depends on its initial energy E_{GRB}, and on the density of the surrounding matter. This means that a progenitor stars that leaves a low-density wind, and which produces a high-energy GRB,

should show the GRB afterglow light curve for a constant density medium, since the jet can travel far before it starts to decelerate (Eqn. 6.14). We have compiled a list of those GRBs for which the density profile of the CSM has been calculated (Table 6.1). This table shows the redshift, the isotropic energy and the inferred density profile according to several authors (see the caption of Table 6.1). Fig. 6.2 shows how the form of the afterglow lightcurve (constant density, wind) is distributed as a function of the isotropic energy of the GRB and the redshift of the host galaxy. Since stars with a low metallicity have low-density winds, we expect that the GRBs, which show the light curve of a constant-density medium, cluster in the high-energy, high-redshift part of the diagram. Of course this is not a very solid prediction, since it fails to take into account the condition of the local ISM, which will vary from source to source. Nevertheless, it can serve as a general indication whether our theory is correct. This Figure shows that afterglow models seem to follow the trend we predicted. There are several exceptions, but on average the GRBs, for which one infers a constant density medium during afterglow production, tend to have a higher isotropic energy and a higher redshift than those GRBs for which one infers a free-wind density profile from the afterglow lightcurve. It is also clear that there are more afterglows that show a wind-like CSM than afterglows with a constant-density environment. However, if afterglows with a constant density profile indeed occur on average at higher redshifts, the relative numbers of the two groups may change with the advent of new data from the SWIFT satellite. Also, in many individual cases, which are not considered here, a constant density profile is preferred (Piro et al. [55]).

6.3 Possible explanations for having the wind termination shock close to the star

The results derived in Sect. 6.2.1 provide us with a variety of ways in which the wind termination shock can be brought closer to the star. We have tested several scenarios, either analytically, numerically or both. For the hydrodynamical simulations we have used the ZEUS 3D code of Stone & Norman [67].

6.3.1 Metallicity dependence of the wind

The mass loss rate of stars depends on their metallicity. For Gamma-Ray Burst progenitors the mass loss rates are probably lower than for most galactic Wolf-Rayet stars, since these progenitors are most likely low-metallicity stars (Wijers [81]). Such stars tend to have lower mass loss rates during their Wolf-Rayet phase (Crowther et al. [13], Yoon & Langer [87]). Since the ram pressure of the wind depends linearly on the mass loss rate, this helps to bring the wind termination shock closer to the star. The problem with this scenario is that the variation in mass loss rate is simply not enough. From Eq. 6.5 we know that a change in mass loss rate of two orders of magnitude brings the wind termination shock only one order of magnitude closer to the star. In other words, in order to go from 10 pc to 0.1 pc, the mass loss rate would have to be **four** orders of magnitude lower. Yoon & Langer give the metallicity dependence of the mass loss rate as either:

$$\log\left(\frac{\dot{M}_{\rm w}}{\rm M_\odot yr^{-1}}\right) \propto 0.5\log\left(\frac{Z}{Z_\odot}\right), \tag{6.25}$$

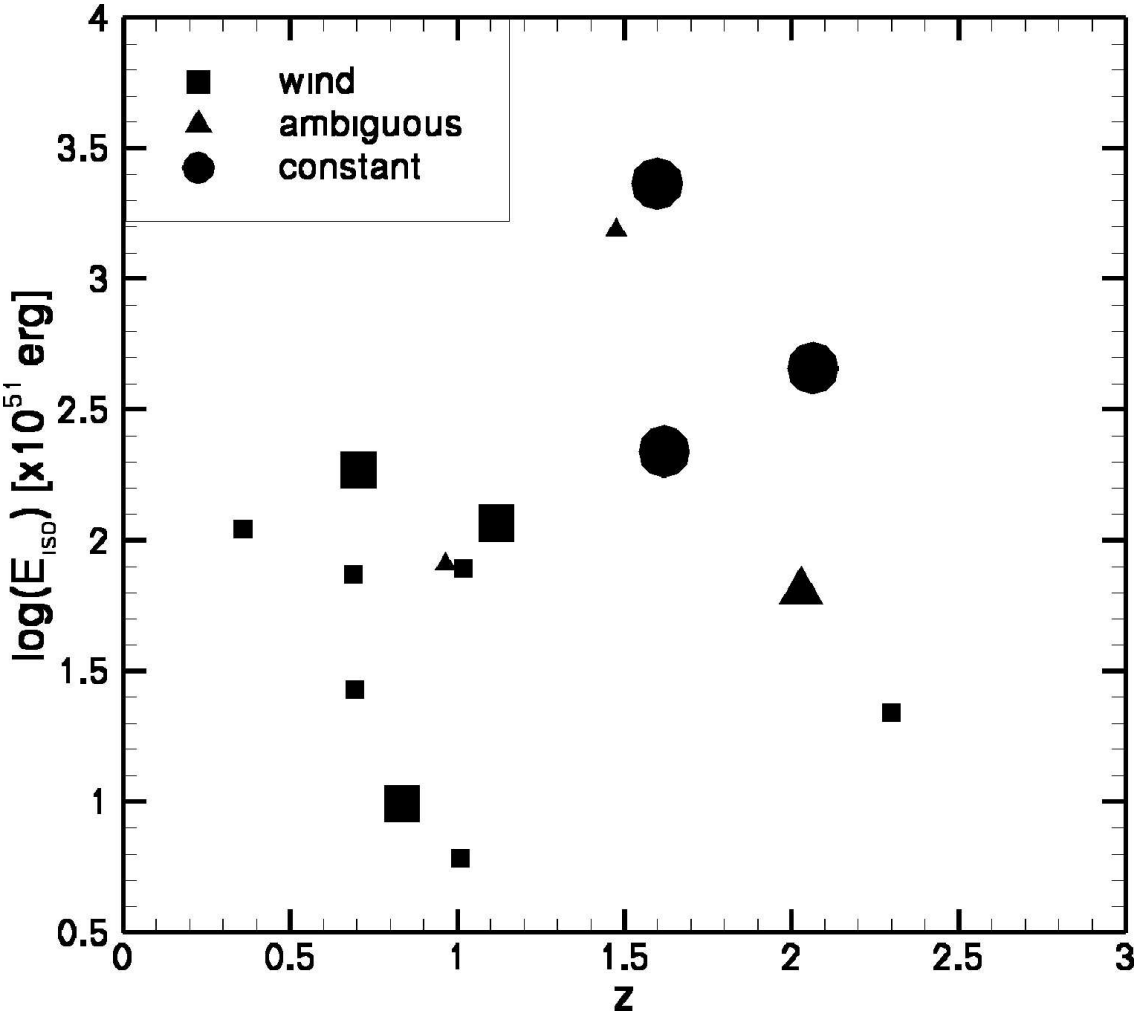

Figure 6.2: Distribution of GRBs over the redshift-isotropic energy space. The GRBs in this plot have been taken from Table 6.1. Those GRBs, whose afterglow shows a constant density profile (circle) tend to have high energy and occur at larger redshifts than the afterglows which are formed in a free-streaming wind (square). The ones marked as triangles are ambiguous, which means that either different groups disagree on the nature of its afterglow, or no group has decided on its nature. If the symbol is large, several groups have reached the same conclusion. References for these afterglow models are: Chevalier & Li [9], Panaitescu & Kumar [50], Panaitescu & Kumar [51] and Chevalier et al. [10].

or

$$\log\left(\frac{\dot{M}_{\rm w}}{\rm M_\odot yr^{-1}}\right) \propto 0.86 \log\left(\frac{Z}{Z_\odot}\right), \tag{6.26}$$

depending on the stellar model and the type of Wolf-Rayet star. At low metallicity, Wolf-Rayet progenitors could have a lower luminosity, which would decrease the mass loss rate by about one order of magnitude (Yoon & Langer [87]). Therefore, even for the relationship in Eq. 6.26 the metallicity would have to be reduced by more than three orders of magnitude to bring the wind termination shock to 0.1 pc.

Both the mass loss rate and the wind velocity of Wolf-Rayet stars vary considerably from one star to another (Woo [83]; Hamann et al. [28]; Koesterke & Hamann [31]),

Table 6.2: Assumed parameters for the three evolutionary stages of our 35 $M_\odot$ model (Z=0.20).

Phase	End of phase [yr]	$\dot{M}_w$ [$M_\odot$ yr^{-1}]	V_w [km s^{-1}]	n_{photon} [s^{-1}]
Main Sequence	4.745×10^6	6.6×10^{-7}	2 671	3.4×10^{47}
Red supergiant	5.098×10^6	5.5×10^{-5}	15	3.3×10^{41}
Wolf-Rayet	5.295×10^6	2.8×10^{-5}	2 140	3.3×10^{47}

as well as during the lifetime of a single Wolf-Rayet star. Even so, in order to reduce the termination shock radius to $R_w \sim 0.1$ pc one must assume the lowest possible wind velocity, combined with the lowest possible mass loss rate for a given star. While this situation might occur on occasion, it is too extreme to account for the moderately large percentage of GRBs afterglows for which one infers a constant-density medium.

Another problem with the metallicity dependence of the mass loss rate is the fact that it holds for main sequence stars as well as Wolf-Rayet stars. Therefore, a star with a weak Wolf-Rayet wind most likely has a weak main sequence wind as well. This means that the thermal pressure in the hot bubble will be low (Eq. 6.3, which puts the wind termination shock further away from the star. This effect is not as strong as the direct influence of the weak Wolf-Rayet wind, but it decreases the overall effect of the weak wind.

A benefit of low mass loss rates is that the density of the wind will be low, which conforms to many of the afterglow lightcurve models (Chevalier et al. [10]). This allows the GRB jet to penetrate further into the CSM before it decelerates. This can explain why a signature of the wind termination shock does not show up in most GRB afterglow lightcurves: the jet is already past this point when the afterglow starts.

6.3.2 A high-density ISM

If the density of the ISM is increased, the whole wind-blown bubble becomes smaller, including the radius of the wind termination shock. A large range of densities in the ISM surrounding GRB progenitors is to be expected. Stars are formed inside molecular clouds, which means that the star may find itself in a high density region. Unfortunately, the dependence of the wind termination shock radius on the ISM density ρ_0 is not strong, $R_w \propto \rho_0^{-3/10}$ (c.f. Eqn. 6.5). This means that the density has to be very large in order to bring the wind termination shock as close to the star as we need, see for instance Eldridge et al. [16].

Figures 6.3 and 6.4 show the effect of a massive increase in the density of the ISM. Both segments of the figure show the density around a 35 $M_\odot$ star based on the star models calculated by Schaller et al. [63]. In one segment, the density has been set at $10^{-22.5}$ g cm^{-3}; in the other it is $10^{-19.5}$ g cm^{-3}. Both simulations were done using the method described in van Marle et al. ([72], [73], [74]). For the simulation with the low-density ISM the resolution is equal to 1000 radial grid points by 200 angular grid points. The high-density ISM simulation has a grid of 500 radial grid points by 200 angular grid points. The main-sequence and the start of the red supergiant phase are simulated in 1D, and the results are mapped onto the 2D grid. The end of the red supergiant phase, as well as the Wolf-Rayet phase, are simulated in two dimensions.

The wind parameters for the three phases of the stars evolution can be found in Table 6.2. As can be expected from Eqn. 6.5, a change in the ISM density by three orders of

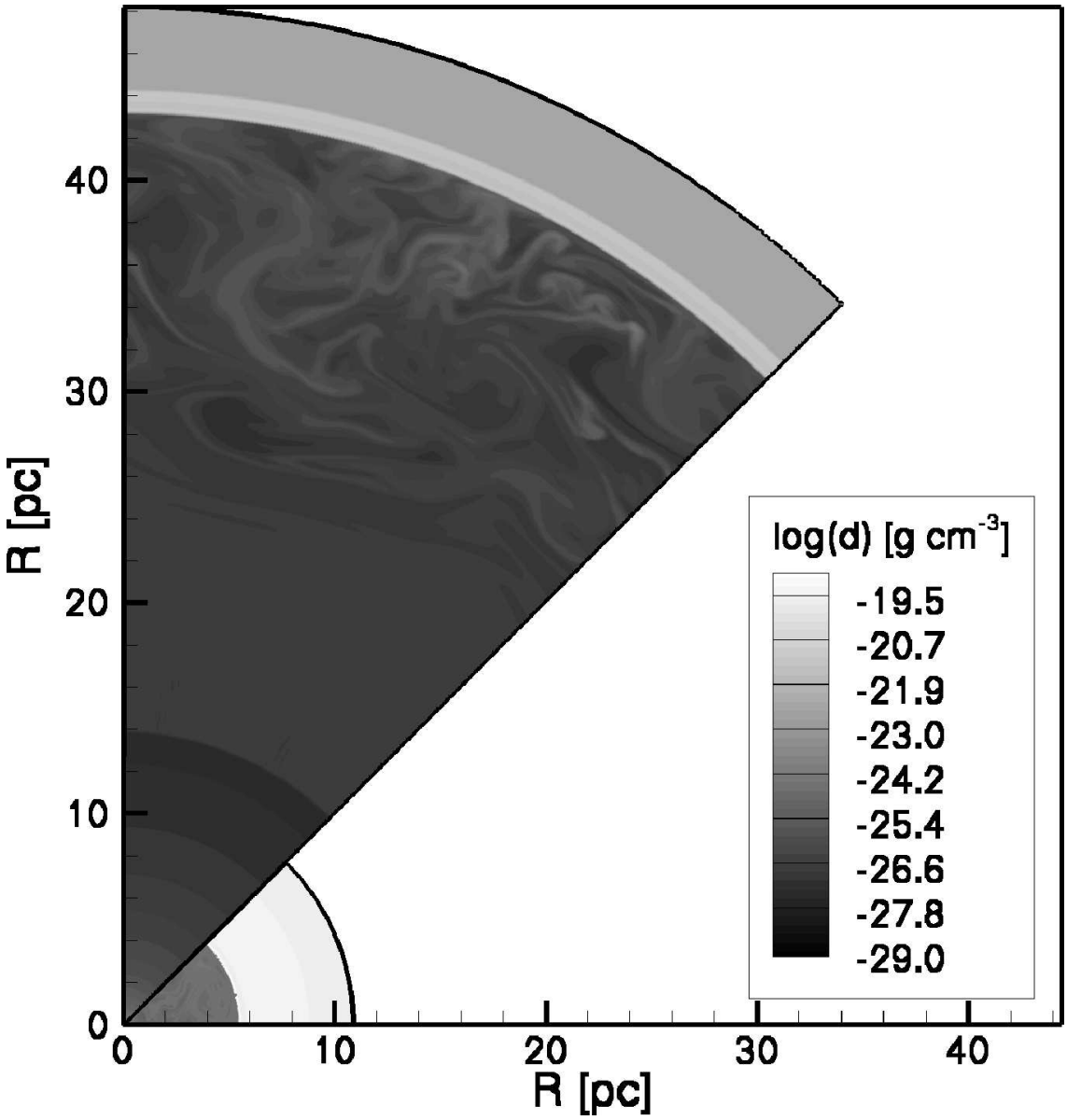

Figure 6.3: The density of the gas around a 35 $M_\odot$ star with the density of the ISM set to $\rho_0 = 10^{-22.5}$ g cm^{-3} (upper segment) and $\rho_0 = 10^{-19.5}$ g cm^{-3} (lower segment). The high density of the ISM in the second segment limits the size of the bubble considerably, which increases the density in the bubble. Both segments show the same epoch, just before the star explodes as a supernova.

magnitude changes the location of the wind termination shock by approximately a factor 10. To bring the wind termination shock even closer to the star would be difficult. To get a termination shock distance $R_w \sim 0.1$ pc one needs an ISM with a density of about $\rho_0 \sim 10^{-16}$ g cm^{-3}, which is rather unlikely. Again, as in Sect. 6.3.1, this scenario can only account for a few GRB progenitors.

6.3.3 A high-pressure ISM

The analytical solution described in Sect. 6.2.1 is only valid if the ISM is cold so that the circumstellar bubble expands supersonically with respect to the surrounding ISM. For a

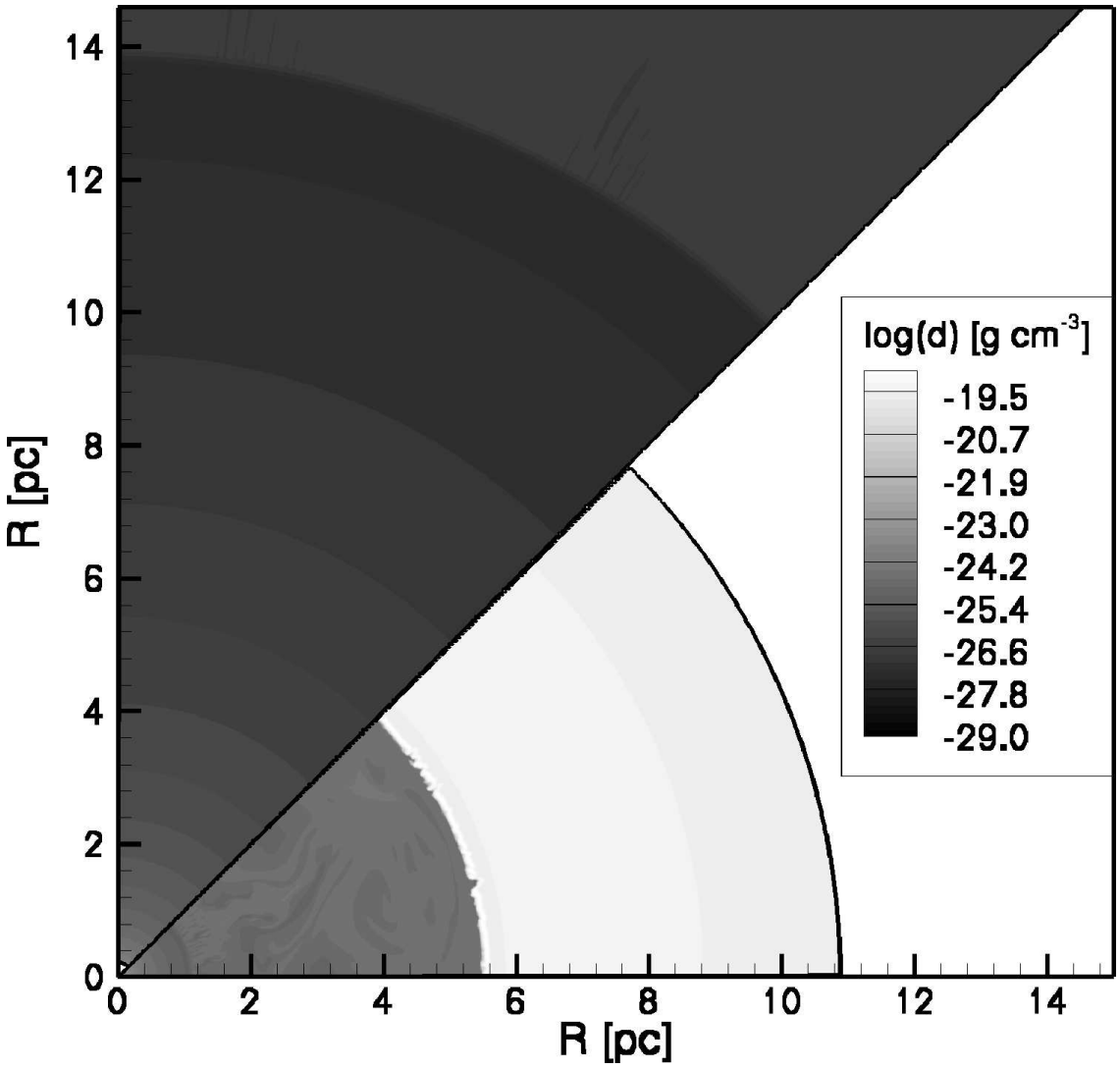

Figure 6.4: A blow-up of the central portion of Fig. 6.3. In the upper segment the wind termination shock can be seen at $R \sim 14$ pc. In the lower segment the termination shock is located at $R \sim 1$ pc.

sufficiently high ISM temperature, the thermal pressure of the ISM will act as an extra confining force on the expanding shell. An example of such a situation is a circumstellar HII region. If the star photo-ionizes the surrounding gas, the shell will expand more slowly. The expansion speed may even become subsonic. In that case the shell dissipates, and the circumstellar bubble will have a density discontinuity at the location where the shocked wind material meets the photo-ionized ISM. This effect has been described in van Marle et al. ([72], [73], [74]).

A hot ISM is the explanation offered by Chevalier et al. [10] for the presence of matter with constant density close to the progenitor star. They describe the structure of a circumstellar bubble that has expanded into a low-density, extremely hot medium. In such a situation, the main sequence wind can never create a supersonically expanding shell. The expansion of the bubble remains subsonic, which means that the thermal pressure in the hot wind bubble must approximately equal to the thermal pressure in the ISM. Pressure balance between the wind ram pressure and the pressure in the ISM, $\rho_w V_w^2 \sim P_0$,

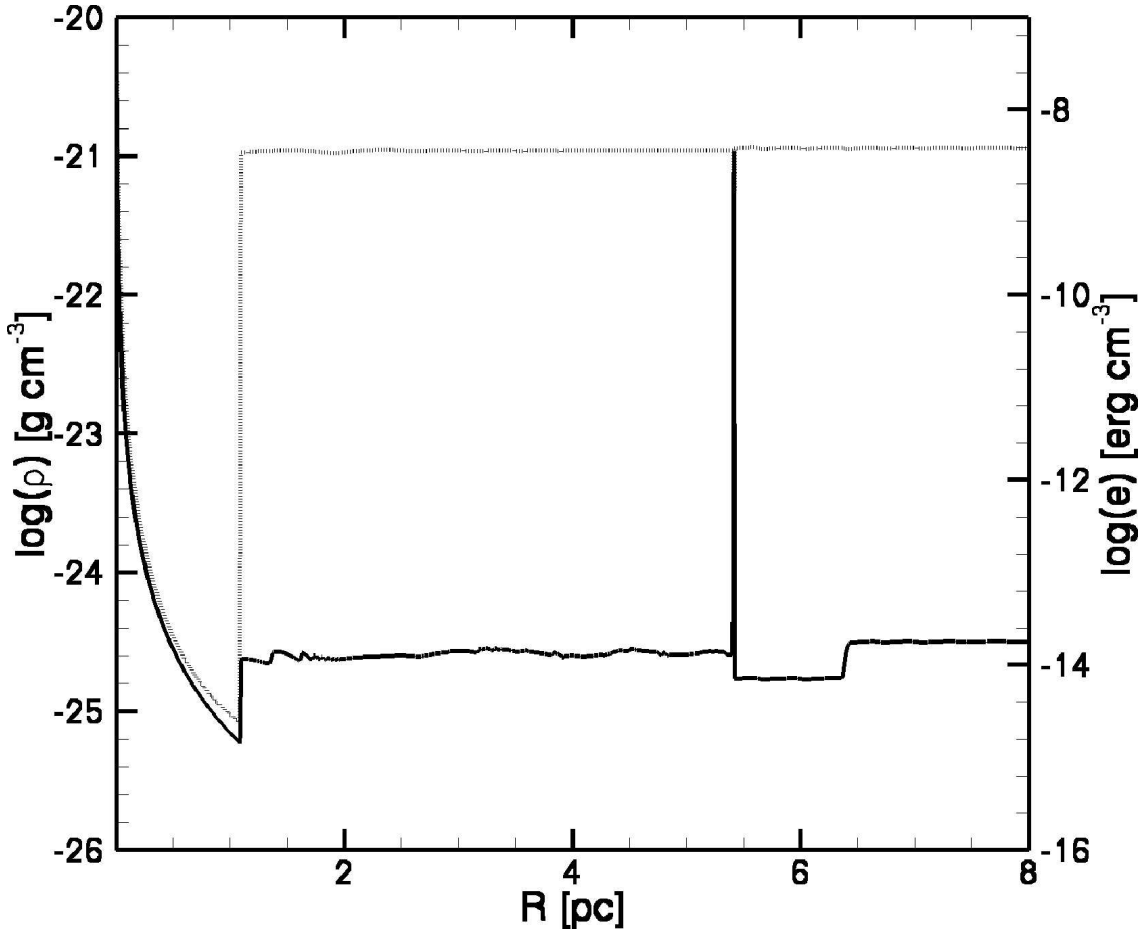

Figure 6.5: The mass density (solid curve) and the internal energy density (dotted curve) of a circumstellar bubble that is expanding into a high-pressure ISM. Shown is the situation at a moment just before the star explodes as a supernova. Moving outward from the star (from left to right) we see the free-streaming Wolf-Rayet wind, the wind termination shock (at $R_w \sim 1$ pc), the hot bubble filled with the shocked Wolf-Rayet wind material, the Wolf-Rayet wind driven shell (at $R \sim 5$ pc), the bubble of shocked main sequence wind material, and the ISM ($R \geq 6.5$ pc).

gives the radius of the wind termination shock as:

$$R_w \approx \left(\frac{\dot{M}_w V_w}{4\pi P_0} \right)^{1/2} . \tag{6.27}$$

We have performed a simulation of a similar situation, the results of which are shown in Fig. 6.5. We used the same 35 $M_\odot$ star model that was used for the high-density simulation that was described in Sect. 6.3.2. The temperature of the ISM was set to 10^8 K. The 1D radial grid has 10 000 grid points. In Fig. 6.5 the wind termination shock lies quite close to the star, once again at $R_w \sim 1$ pc. The Wolf-Rayet wind-driven shell is still visible, even at the moment of supernova explosion. The reason is the high density and pressure of the main-sequence bubble. The pressure inside the shocked wind is high, since it has to be equal to the ISM pressure. The density in this region is high because the whole bubble is very small: $\rho_b \approx 10^{-25}$ g cm^{-3}, which corresponds to a particle density $n_b \sim 0.1$ cm^{-3}, close to the value quoted by Chevalier et al. [10]. This situation results in a slow expansion speed of the Wolf-Rayet shell. In a 2D or 3D simulation, the Wolf-Rayet

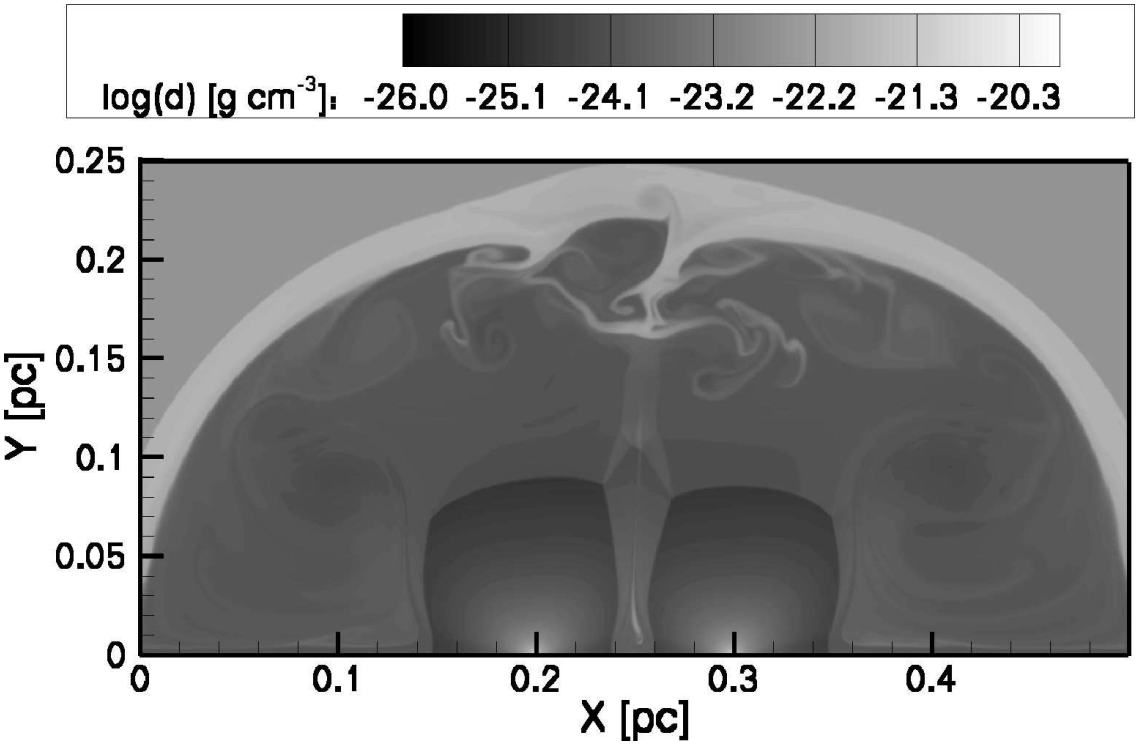

Figure 6.6: The density of the gas around two massive stars during the main sequence. The CSM bubbles of the two stars have merged, creating a superbubble. The image corresponds to the situation approximately 800 years after the start of the evolution of the bubble.

shell would have been fractured by its collision with the Red Supergiant shell (García-Segura et al. [24], [25]; van Marle et al. [73], [74]) left by the progenitor in an earlier evolutionary phase.

However, a circumstellar environment such as described here is difficult to create. Even if we consider a large association of massive stars that creates a *superbubble*, basically the merged wind-blown bubbles of a number of stars, it is virtually impossible to increase the pressure to the level required to push the wind termination shock back to $R_w \sim 0.1$ pc. Equation 6.27 shows the problem quite clearly. If the wind termination shock has to be ~ 10 times closer to the star, the pressure in the surrounding ISM as to be a factor ~ 100 larger. This means that the total mechanical luminosity of the association that feeds the bubble has to be $\sim 10^5$ times larger than the typical mechanical luminosity of a single star, as the pressure in the bubble scales with the total mechanical luminosity as $P_b \propto L_{tot}^{2/5}$, c.f. Eqn. 6.3. Effectively, this means that 100,000 massive stars have to dump the kinetic energy of their wind into the bubble simultaneously. These rather excessive demands make this scenario a less than effective solution.

6.3.4 Colliding winds

In reality the problem shown in Sect. 6.3.3 may not be insurmountable provided two stars are sufficiently close together, for instance in a binary. In that case, the winds of the two stars collide directly, rather than simply feed energy into the same superbubble. In the combined wind bubble the temperatures will rise very rapidly in regions where the winds collide. We will consider the binary scenario, in the following paragraph. In

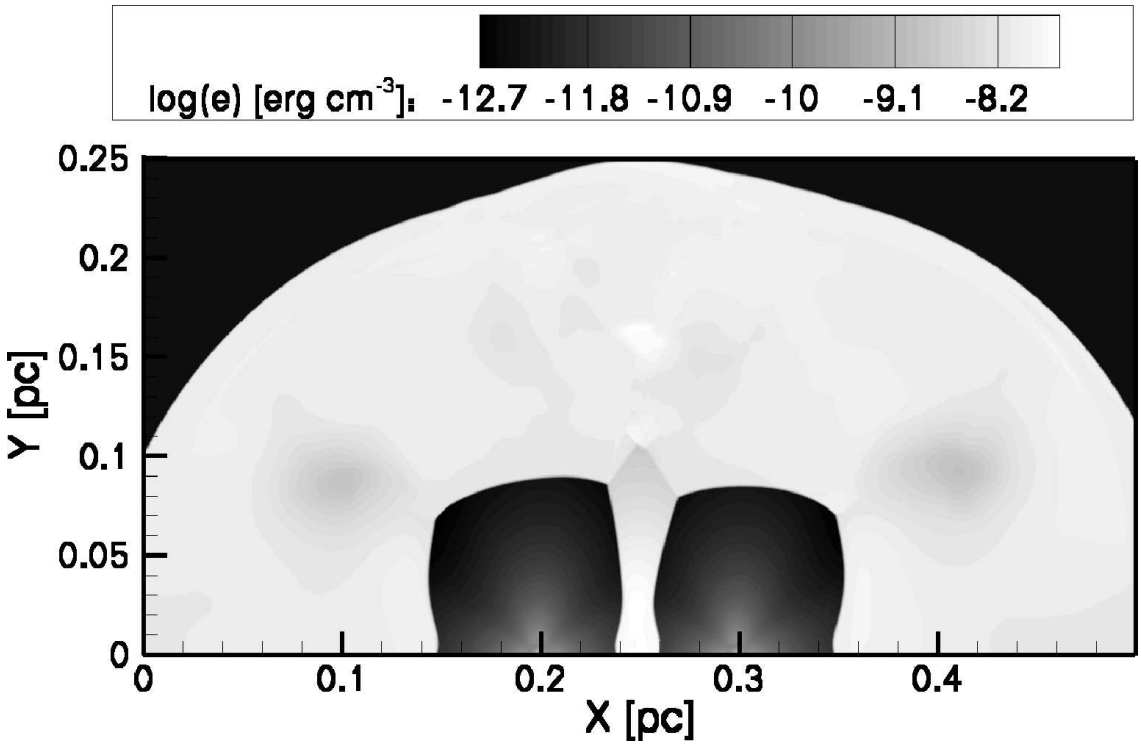

Figure 6.7: The internal energy density of the CSM surrounding the two stars at the same epoch as in Fig. 6.6. The internal energy density is highest between the stars, where the stellar winds from both stars contribute to the heating of the gas.

Table 6.3: Wind parameters for the binary stars simulation shown in Fig. 6.8.

	$\dot{M}_{\rm w}$ [$M_\odot\,{\rm yr}^{-1}$]	$V_{\rm w}$ [$\rm km\,s^{-1}$]
Star 1	1.0×10^{-5}	1 000
Star 2	1.0×10^{-4}	10

this paragraph we will consider the simpler case of two stationary stars, which are not gravitationally bound.

Figs. 6.6 and 6.7 show what happens when two stars independently feed mechanical energy into the same bubble. The simulation was done in 2D on a cylindrical grid of 1000×500 grid points. The two stars both have the same mass loss rate ($\dot{M} = 4 \times 10^{-6}$ $M_\odot\,{\rm yr}^{-1}$) and wind velocity ($V_{\rm w} = 2000$ $\rm km\,s^{-1}$). The two stellar winds have been simulated by filling two half spheres on the Z-axis with gas, moving away from central points (the stars) with a stellar wind density distribution (decreasing with the radius squared). The simulation includes radiative cooling, but the effect of photo-ionization is not considered. The winds never collide directly. Instead, each star creates its own bubble. When their respective main sequence shells hit each other, the bubbles merge. The region directly between the two stars is a-typical for the rest of the region, since the pressure is higher.

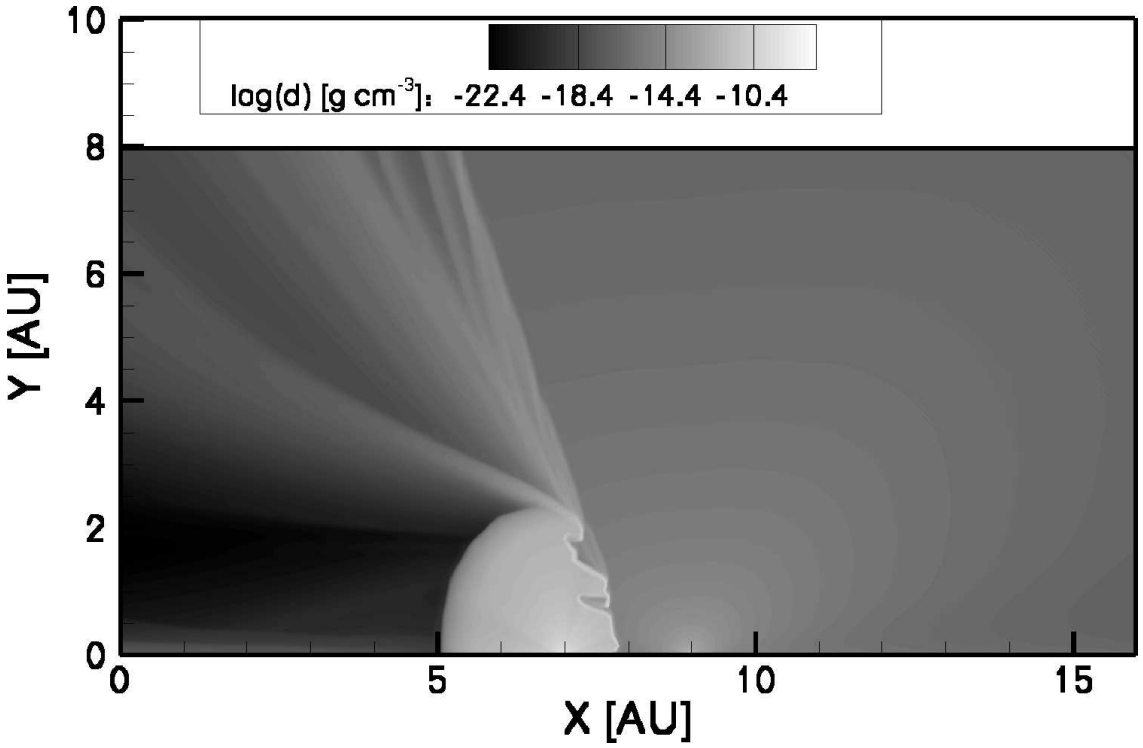

Figure 6.8: The density of the gas around two stars with different wind parameters. The left star has a high mass loss rate and a low wind velocity, while the right star has a low mass loss rate but a high wind velocity, so that its ram pressure is the largest. The stronger wind (from the star on the right) dominates the CSM, while the weaker wind (on the left) is folded back, away from the companion star.

6.3.5 A binary companion

The presence of a binary companion can bring the wind termination shock closer to the star (Eldridge et al. [16]). For instance, in a Wolf-Rayet/O star binary system, the Wolf-Rayet star, which has the smaller mass, will orbit the O-star. The Wolf-Rayet wind will be distributed over a larger volume, which decreases the density of the wind and its ram pressure. However, this effect is probably not very significant. If we are dealing with a close binary, the radius of the orbit is smaller than R_w and the increase in volume is small. If we are dealing with a wide binary, the orbital motion will be so slow, that the effect on the wind is no longer significant: to lowest order the Wolf-Rayet star can be treated as motionless.

The wind emanating from the companion star is unlikely to be of any substantial influence: the ram pressure of a Wolf-Rayet star wind is much larger than that of the wind from nearly any other star. The wind from the companion will be pushed back in a bowshock, and its material will be constrained to a narrow layer in the orbital plane. This is demonstrated in Fig. 6.8. This is a simplified model of two stars in a binary system. The star on the left has a high mass loss rate, and a low wind velocity, like a red supergiant or luminous blue variable; the star on the left has a lower mass loss rate, but a high wind velocity, like a Wolf-Rayet star (Table 6.3). The simulation is done in two dimensions, assuming a cylindrically symmetric situation. At the beginning of the simulation the grid is filled with ambient material at a constant density. The simulation includes radiative

Table 6.4: Assumed parameters for the stellar wind in our bowshock model (Figs. 6.9, to 6.11).

phase	$\dot{M}_w$ [$M_\odot\,yr^{-1}$]	V_w [$km\,s^{-1}$]
Red Supergiant	1.0×10^{-4}	10
Wolf-Rayet	1.0×10^{-5}	1 000

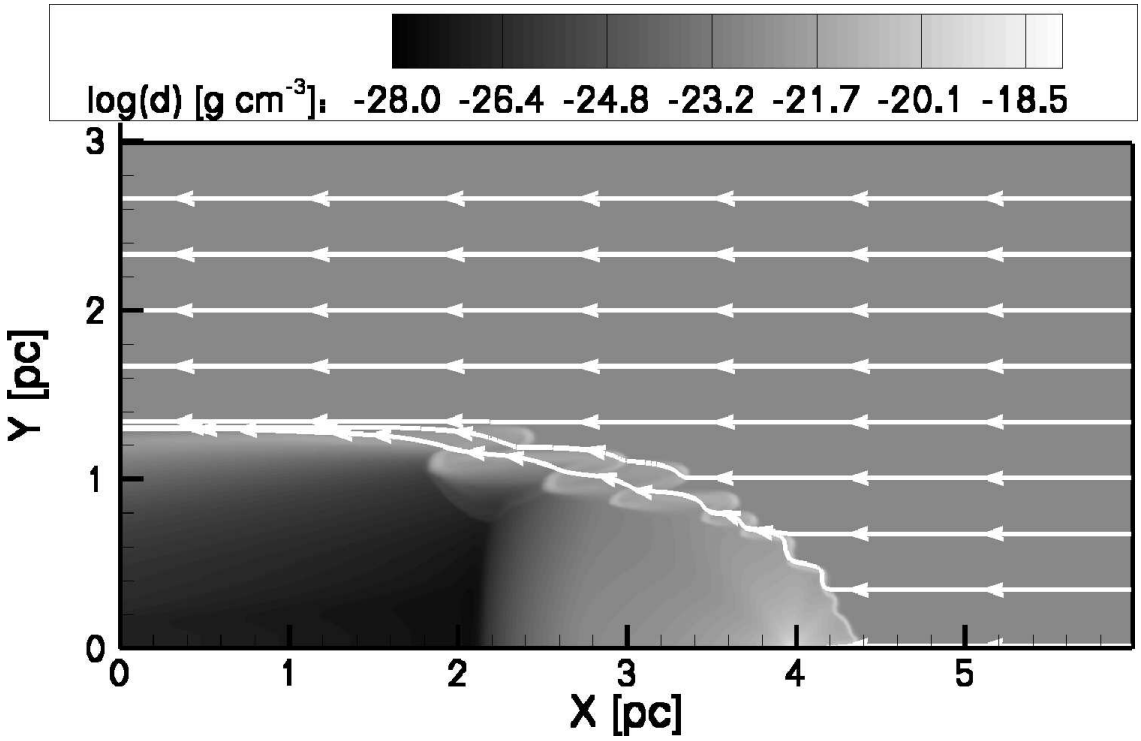

Figure 6.9: The density of the gas around a moving red supergiant star. The velocity field in the ambient medium is shown as stream traces. The bowshock shell shows Kevin-Helmholtz instabilities.

cooling, but the effect of photo-ionization is not considered. This simulation does not take the orbital motion of the stars into account. It shows quite clearly how the weaker wind is being folded back by the strong Wolf-Rayet wind. An analytical solution pertaining to this situation was given by Canto et al. [6], while numerical simulations have been presented by Stevens et al. [66].

The jet associated with the GRB is expected to move along the rotation axis of the progenitor star, which should be perpendicular to the orbital plane. Therefore, the companion star and its wind would have little or no influence on the GRB jet and the afterglow light curve. Of course, it is possible that a jet propagates through the wind of another star, which happens to be nearby. In that case, the density profile encountered by the GRB would depend entirely on the angle at which the jet hits the free-streaming wind. If it would meet the companion wind head-on, it would actually encounter a density that **increases** as the jet penetrates deeper into the wind.

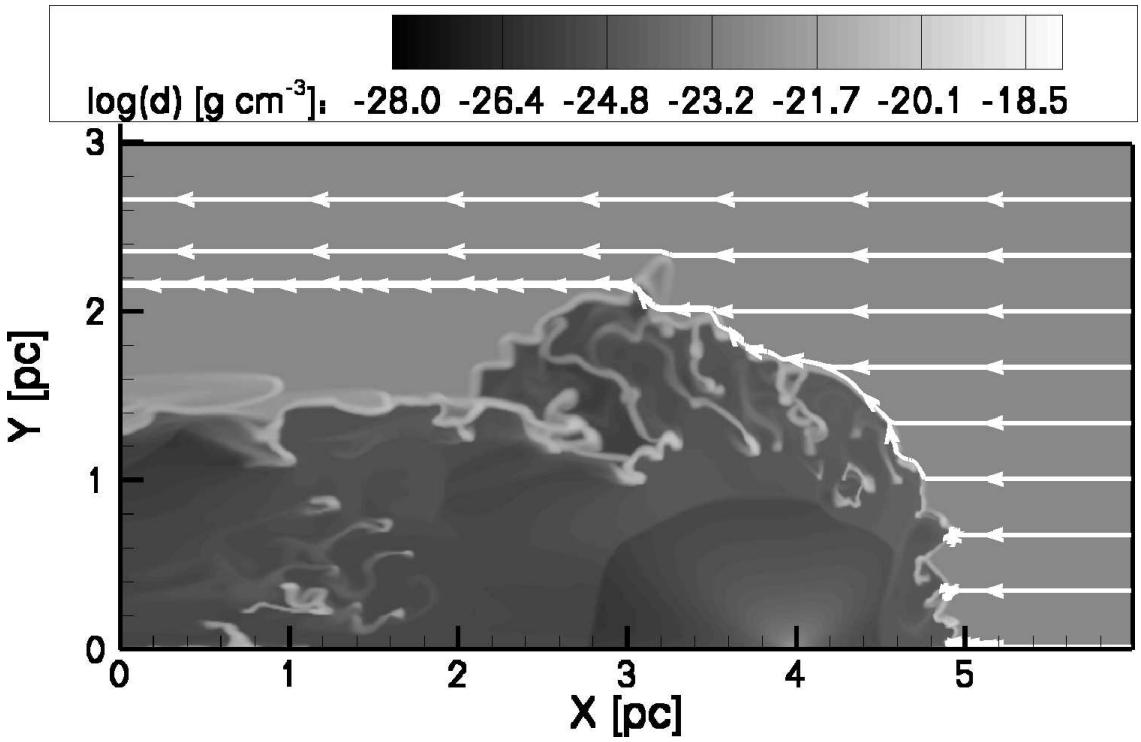

Figure 6.10: Similar to Fig. 6.9, but after the star has become a Wolf-Rayet star. The newly formed bowshock-shell system, which is sweeping up its predecessor, is highly unstable.

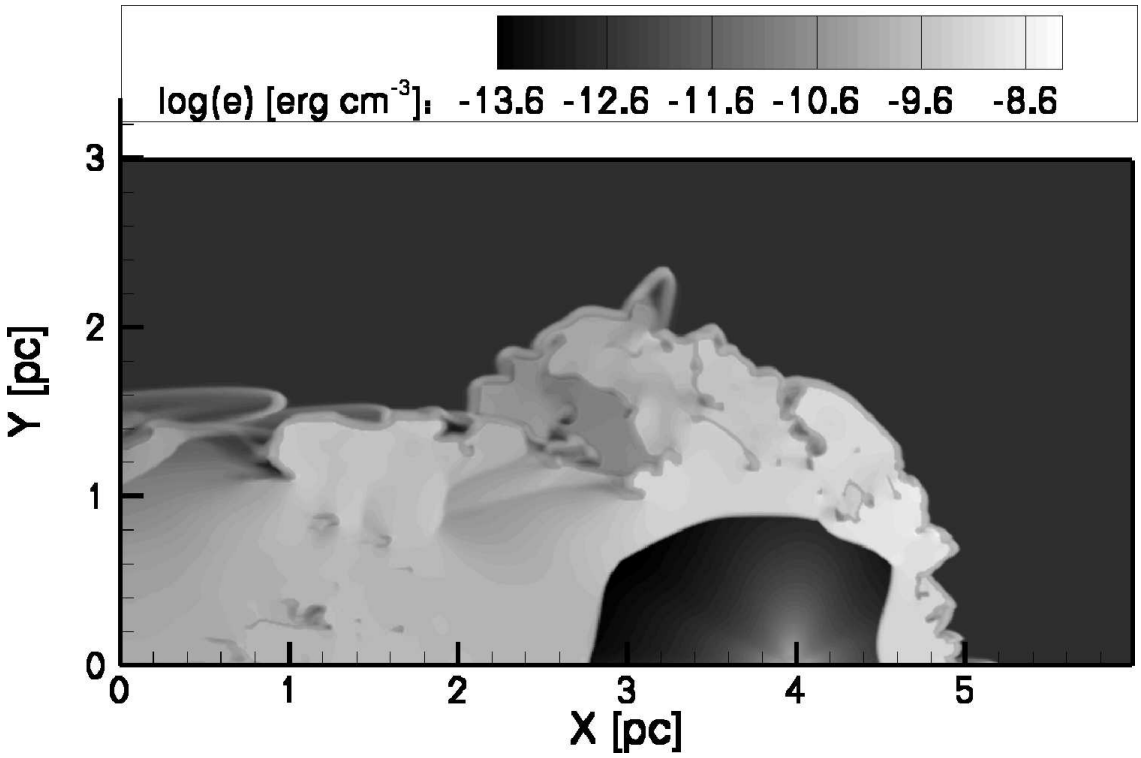

Figure 6.11: The internal energy density at the same moment in time as in Fig. 6.10. The wind termination shock is clearly visible, 0.5...1.25 pc away from the star, depending on the angle.

6.3.6 Stellar motion

If the progenitor star is moving rapidly through the interstellar medium, the situation becomes completely different. The equations in Sect. 6.2.1 apply when the star is motionless relative to the surrounding gas. However, if the star is moving at supersonic velocity with respect to the ISM, the collision between stellar wind and ISM will create a bowshock. This bowshock forms at the distance from the star $R_{\rm bs}$, where the ram pressure of the wind equals the ram pressure of the ISM in the frame where the star is at rest. The stand-off distance of the bowshock equals

$$R_{\rm bs} = \sqrt{\frac{\dot{M}_{\rm w}\, V_{\rm w}}{4\pi\rho_0\, v_\star^2}}, \tag{6.28}$$

where $v_\star$ is the velocity of the star (Wilkin [82]). For a Wolf-Rayet wind, with a velocity of 2 000 km s^{-1} and mass loss rate 3×10^{-5} M$_\odot$ yr^{-1}, from a star that moves with a velocity of 80 km s^{-1} through an ambient medium with a density of $10^{-22.5}$ g cm^{-3}, this gives us a radius of the bowshock directly in front of the star of $R_{\rm bs} \simeq 1.25$ pc. Generally, the radius of the bowshock depends on the angle between the position vector and the direction of motion. Similarly, the radius of the reverse shock is angle dependent, since the hot bubble of shocked wind material is not isobaric. The thermal pressure will be highest directly in front of the star, where the wind collides head-on with the ambient medium.

Such a rapidly moving star can be the survivor of a close binary, where the companion has exploded as a supernova. The force of the supernova explosion broke up the binary, and the surviving star has moved away at approximately its original orbital velocity. Such runaway stars are not uncommon, but they do not always form a bowshock. If the star moves through a hot region of space (such as an HII region, or the circumstellar bubble of another stars), its motion is subsonic and no bowshock is formed (Huthoff & Kaper [30]). In fact, during the early stages of its runaway phase, the star can not possibly form a bowshock, since it is moving through its own main-sequence wind bubble, where the temperature will be on the order of 10^7 K, and the speed of sound is of order 300 km/s. How much time the star needs to get clear of its own bubble is extremely difficult to predict, as both the velocity of the star and the radius of the bubble can vary by at least an order of magnitude. Typically, this will be on the order of 10^5...10^6 years. Several Wolf-Rayet stars with bowshocks have been observed, such as M1-67 around WR 124 (van der Sluys & Lamers [70]).

To get a better idea of the morphology of the circumstellar medium around a fast moving star, we have performed a two-dimensional hydrodynamical simulation. Since the stellar wind is assumed to be equally strong in all directions, it is possible to use a cylindrical grid, using the Φ axis as symmetry axis. The Z-axis coincides with the direction of motion. This is similar to the approach used by Brighenti & D'Ercole [5] and Comerón & Kaper [12]. Initially, the grid is filled with an ambient medium ($\rho_0 = 10^{-22.5}$ g cm^{-3}), which travels along the Z-axis at a constant velocity ($v_\star = 80\,{\rm km\,s^{-1}}$). Matter flows in at one end of the grid, and out at the other. The wind from the star is simulated by filling half a sphere on the Z-axis with material, which moves outward from a central point, and which has the density distribution of a stellar wind (like we did to model the binary system in Sect. 6.3.5). Grid resolution has to be rather high, in order to resolve the Kevin-Helmholtz instabilities in the shell (Brighenti & D'Ercole [5]). The stellar wind in our models follows two separate evolutionary phases: first the red supergiant phase,

followed by a Wolf-Rayet phase. The wind parameters for these two phases can be found in Table 6.4. Photo-ionization is not included in this simulation.

In Figs. 6.9 through Fig. 6.11 we show the results. Figure 6.9 displays the density of the circumstellar medium during the red supergiant phase. The bowshock shell is clearly visible: it shows a series of so-called 'Cat's eyes', which are the result of a fully-developed Kevin-Helmholtz instability. These instabilities only occur if the ambient medium is cold. If the star moves through an HII region, the instabilities disappear. In Figs. 6.10 and 6.11 the star and wind are in the Wolf-Rayet phase. The fast Wolf-Rayet wind has created a new shell, which sweeps up the old shell. It is extremely unstable. In Fig. 6.11, which shows the internal energy density of the CSM, we can see the location of the wind termination shock. The pressure in the CSM is highest in front of the moving star, where the collision between wind and ambient medium is the most violent. The radius of the wind termination shock varies between 0.5 and 1.25 pc.

Typically, one would expect the star to move in what was originally the orbital plane. This means, that the GRB would be directed about 90^o away from the direction of motion, since the jets should move along the stellar rotation axis. The radius of the wind termination shock at that position angle is ca. 1 pc.

6.4 Combining different scenarios in order to decrease the wind termination shock radius

It is possible, that several of the mechanisms considered in Sect. 6.3 act together. However, not all combinations are possible.

6.4.1 Combining stellar wind parameters and ISM density

A low ram pressure of the wind can be combined with every other mechanism, since it depends purely on the internal structure of the star, while the other mechanisms rely on special external conditions such as the density or pressure in the ISM. The effect of combining different wind parameters and variations in the density of the ISM is shown in Fig. 6.12. Here we have taken a massive star, and varied the wind velocity and mass loss rate during the Wolf-Rayet phase. As a basis we use the 35 $M_\odot$ star model from Table 6.2. The evolutionary time, and the parameters for main-sequence and red supergiant wind are kept constant, but the parameters for the Wolf-Rayet wind are varied. The wind velocity of Wolf-Rayet stars varies between 500 and 5000 $\mathrm{km\,s^{-1}}$, while the mass loss rate varies between 1.0^{-7} and 1.0^{-4} $M_\odot\,\mathrm{yr^{-1}}$ (c.f. Hamann et al. [28] and Koesterke & Hamann [31]). We have plotted the mass loss rate, the wind velocity and the density of the ambient medium in Fig. 6.12. The density of the surrounding ISM was varied between 5×10^{-4} and 5×10^4 particles per $\mathrm{cm^{-3}}$. The results show a considerable variation in the location of the wind termination shock. As discussed at length above, the constant density inferred from some GRB afterglows is thought to be a signature of the shocked wind material. The quantitative value of this density can be calculated analytically, by dividing the total mass loss of the star over the spherical volume of the bubble. The outer edge of the bubble has a radius (Weaver et al. [79])

$$R = \left(\frac{250\,L_\mathrm{w}}{308\pi\rho_0}\right)^{1/5} t^{3/5}\ . \tag{6.29}$$

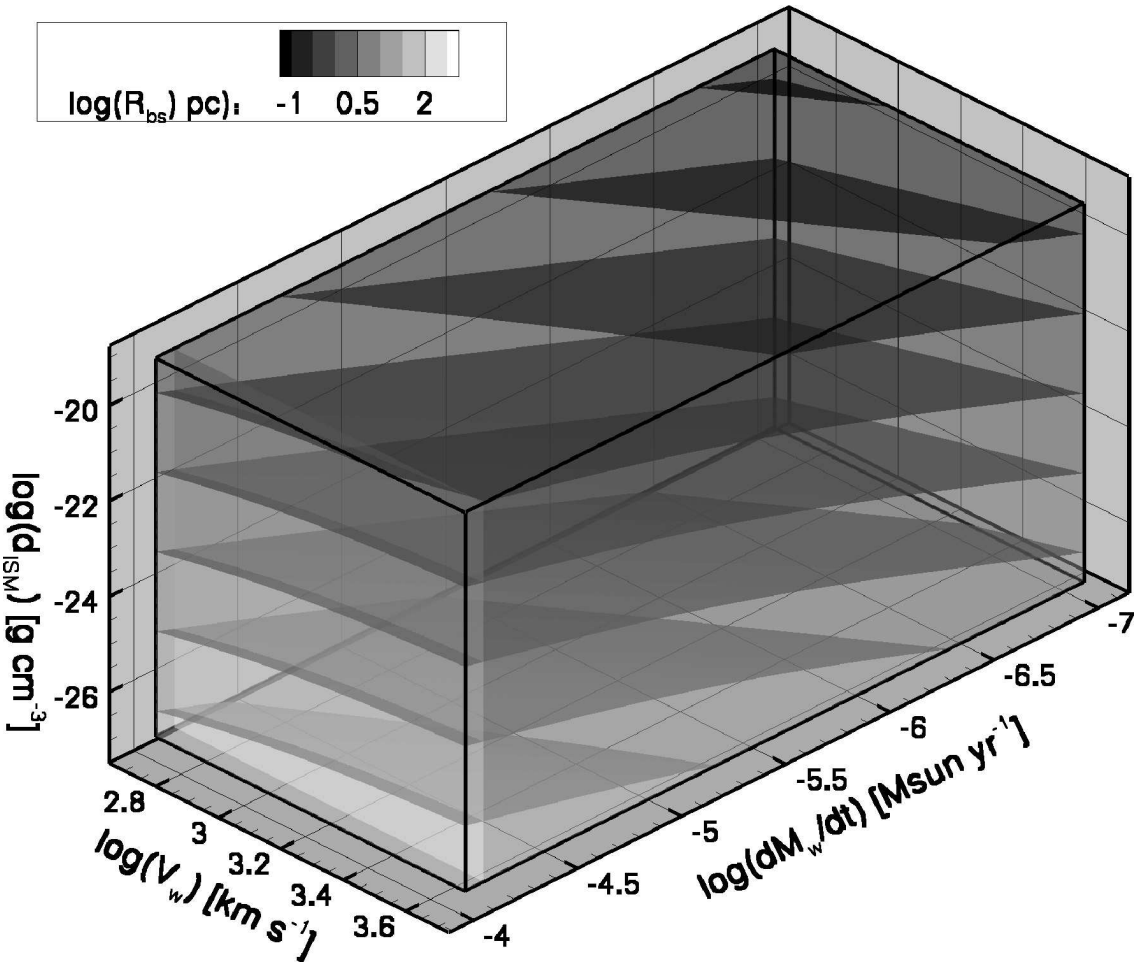

Figure 6.12: The analytical solution for the radius of the reverse shock around a Wolf-Rayet star, depending on the parameters of the Wolf-Rayet wind and the density of the ISM. The radius of the reverse shock was calculated with Eqn. 6.5. The Wolf-Rayet lifetime has been taken constant and the wind parameters for the main sequence and red supergiant phase come from Table 6.2. The parameter space in this figure covers Wolf-Rayet wind velocities between 500 and 5000 $\mathrm{km\,s^{-1}}$, mass loss rates between 10^{-7} and 1.0^{-4} $\mathrm{M_\odot\,yr^{-1}}$ and ISM densities ranging from 5×10^{-4} to 5×10^{4} particles per $\mathrm{cm^{-3}}$. The iso-surfaces in the plot show the planes with a constant radius of the wind termination shock.

Typically, the resulting particle density is less than 10 $\mathrm{cm^{-3}}$ (see also Sect. 6.3.2, and the Figs. 6.3, and 6.4), which is acceptable according to the observations (Stratta et al. [68]).

6.4.2 Combining stellar motion with ISM density and stellar wind parameters

In Fig. 6.13 we show how the radius of the bowshock varies with the stellar velocity $v_\star$ and the density of the interstellar medium ρ_0 in the combination $\rho_0 v_\star^2$ (the ISM ram pressure), and the wind parameters of the star in the combination $\dot{M} V_\mathrm{w}$, the absolute momentum discharge of the wind. The radius of the bowshock follows from Eqn. 6.28. This parameter study is simpler than the case of the stationary star, since the wind velocity and mass loss rate do not have to be plotted independently. The variations in wind parame-

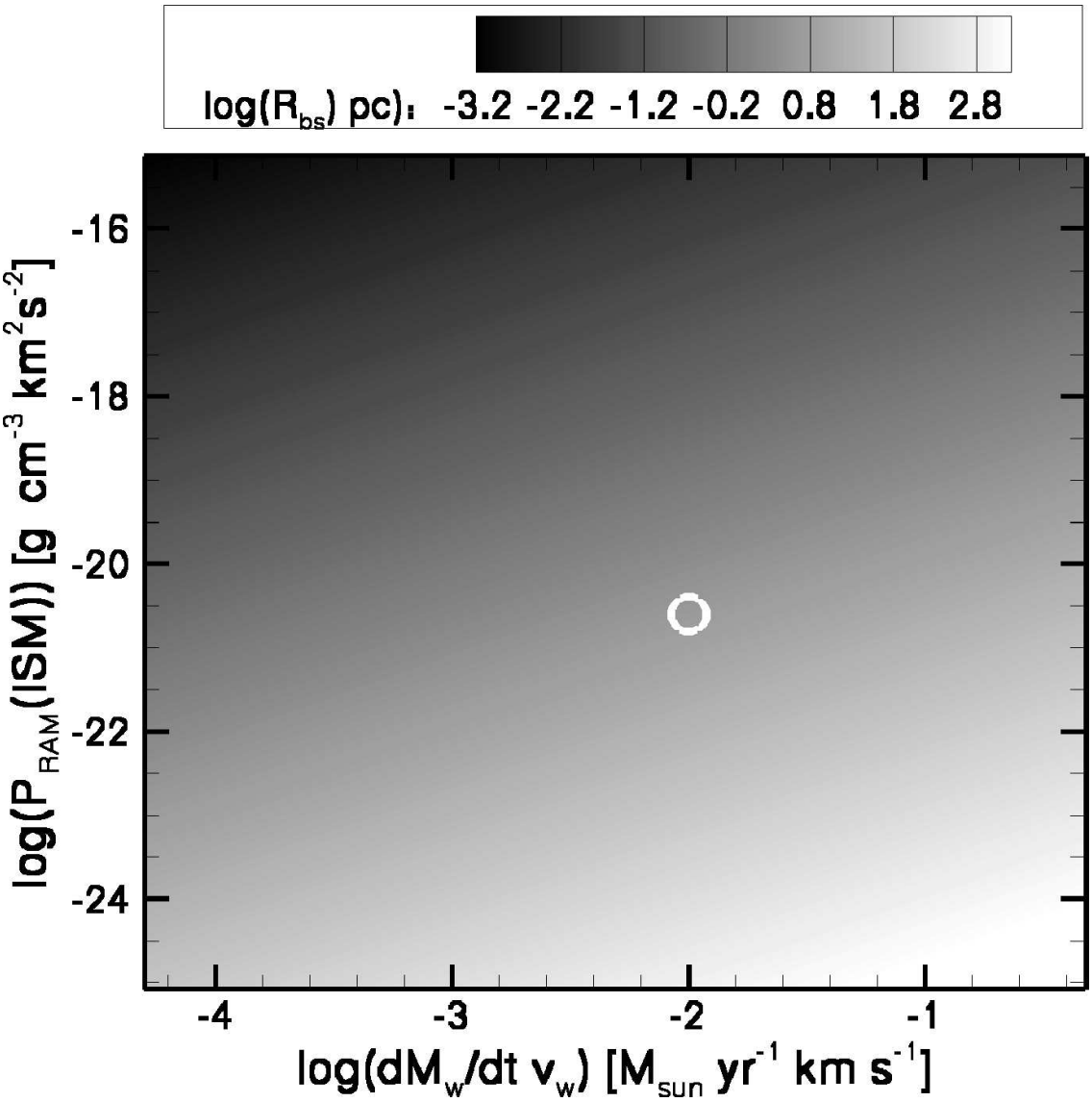

Figure 6.13: The analytical solution for the radius of the bowshock in front of a Wolf-Rayet star, depending on the stellar wind parameters, the velocity of the star and the density of the ISM. On the horizontal axis, the parameters of the stellar wind, on the vertical axis, the ram pressure of the ISM. The radius of the bowshock was calculated with Eqn. 6.28. The wind velocity, mass loss rate and ISM density cover the same intervals as in Fig. 6.12. The stellar velocity varies between 10 and 100 $\mathrm{km\,s^{-1}}$. The circle shows the location of the numerically calculated model from Figs. 6.9 to 6.11.

ters and ISM density are the same as those used to produce Fig. 6.12, while the stellar velocity varies between 10 $\mathrm{km\,s^{-1}}$ and 100 $\mathrm{km\,s^{-1}}$. Fig. 6.13 shows that the radius of the bowshock changes considerably, depending on these parameters. The bowshock can be located closer to the star than the wind termination shock for a stationary star (see Fig. 6.12). In this figure we also show the location of the model that we simulated in the manner described in Sect. 6.3.6. The numerical result from the simulation is quite close to the analytical approximation. The dependence of the bowshock radius on the ISM density ρ_0 is much stronger than the density dependence of the wind termination shock radius for a stationary star, c.f. Eqns. 6.5 and 6.28, which makes this combination particularly

effective. The main problem with the results of Fig. 6.13 is the fact that, for extremely small bow-shock radii, the constant density is provided by the ISM, rather than by the shocked wind material. In those cases the density in the ISM is too high, compared to the observations. These place a limit on the particle density of about 10 cm^{-3} (Stratta et al. [68]). This problem does not occur for GRB afterglows produced in a low-density shocked wind.

6.4.3 Other combinations of scenarios

Combining a high density with a high pressure in the ISM is nearly impossible, since a medium with a high thermal pressure will expand quickly (on its own hydrodynamical timescale), and the density will decrease rapidly. Actually, the high density would have little or no effect. If the pressure is as high as envisioned in Sect. 6.3.3, then the thermal pressure of the gas is much stronger than the ram pressure of a moving shell. This means, that the thermal pressure is the only relevant confining force that acts on the shell, and the actual density of the ISM is no longer relevant.

Binary companions can occur in any environment, irrespective of the density or pressure of the surrounding ISM. However, since the influence of a companion star on the location of the wind termination shock is limited at best, this makes little difference.

Combining stellar motion with a high-pressure environment does not lead to a viable scenario, as the velocity of the star would automatically become subsonic, and the motion of the star would no longer be a relevant factor. In any case, the runaway star would have to live long enough for the star to leave its own circumstellar bubble, since the temperature of the shocked wind material would again make the stellar motion supersonic.

6.5 Conclusions

Of the scenarios discussed, the most likely are: a Wolf-Rayet wind with low ram pressure, a high density ISM, and a moving progenitor star. It is the latter possibility which can bring the wind termination shock extremely close to the star, as shown in Fig. 6.13. Observations show that the wind velocity and mass loss rate vary considerably from one Wolf-Rayet star to another. Since massive stars are thought to form within molecular clouds, a high density ISM appears also possible. Fast moving Wolf-Rayet stars have been observed inside our own galaxy. The combination of a weak Wolf-Rayet wind and a high ISM density can by itself be enough to get the desired result, but the choice of both parameters will have to be rather extreme.

A high pressure ISM can produce the desired result as well, and probably accounts for some of the observed GRB afterglows. However, regions in the ISM with a sufficiently high temperature are rare, especially in or near the dense star-forming regions where the short-lived progenitor stars are located.

While many massive stars have binary companions, this by itself will hardly affect the location of the wind termination shock, since the ram pressure associated with the wind from a Wolf-Rayet is much stronger than that of any possible companion. The Wolf-Rayet wind will therefore dominate the mass flow from the binary system. Only if the binary companion were also a Wolf-Rayet star, its wind might be competitive; Only one such system has ever been found: WR 20a (Rauw et al. [60]), which contains two WN type

stars. However, since these two stars still have most of their hydrogen envelope, they are not yet GRB progenitors.

The orbital motion of a star in a binary system changes the properties of the stellar wind, but its effect is not enough to make a significant difference to the location of the wind termination shock.

There is one possibility, which has not been discussed so far: the constant density medium may not be in the hot bubble that drives the main sequence shell, but in the small bubble of shocked Wolf-Rayet wind material, which drives the Wolf-Rayet shell into the earlier Red Supergiant or Luminous Blue variable wind. For this to be true, the GRB would have to occur extremely early during the Wolf-Rayet phase. (Typically, a Wolf-Rayet wind driven shell moves at velocities in the order of 100 $\mathrm{km\,s^{-1}}$, so it reaches 1 pc within 10 000 years.) Apart from the extremely narrow time frame, there are several other problems with this scenario: First of all, during the early stages of its development, the layer of shocked Wolf-Rayet wind material is extremely thin ($\lesssim$ 1 pc), so any afterglow generated in this medium would almost certainly show sings of either the transition between unshocked and shocked Wolf-Rayet wind, the Wolf-Rayet wind driven shell, or both. Second, the layer of shocked Wolf-Rayet wind, due to its thinness, rarely has a truly constant density, since both Rayleigh-Taylor instabilities of the Wolf-Rayet shell as well as internal turbulence in the shocked wind contribute to local density changes.

The main problem of all discussed scenarios to bring the wind termination shock close to the star is that the parameters of stellar mass loss or the conditions in the ISM have to be pushed to extremes. Therefore, none of the mechanisms described here seems viable to, by itself, account for the high percentage ($\sim$ 25 %) of the observed characteristics of GRB afterglows. However, the large number of possibilities and, in particular, possible combinations of the scenarios presented here, may explain why a significant fraction of GRB afterglows seem to occur in a constant-density medium.

Generally speaking, outside influences like the motion of the star and the condition of the ISM can bring the termination shock to about 1 pc. In order to bring it any closer, the Wolf-Rayet wind has to be weak, which means that the progenitor star most likely had low metallicity. From our models of the circumstellar medium and the GRB afterglow models discussed in Sect. 6.2.4 we can conclude that the GRB afterglows generated in a constant density medium come from low metallicity stars with relatively strong GRBs (although it is an open question, whether the GRB itself was strong or the GRB jet had a narrow opening angle).

Acknowledgements

This work was sponsored by the Stichting Nationale Computerfaciliteiten (National Computing Facilities Foundation, NCF), with financial support from the Nederlandse Organisatie voor Wetenschappelijk Onderzoek (Netherlands Organization for Scientific research, NWO). This research was done as part of the AstroHydro3D project:
(http://www.strw.leidenuniv.nl/AstroHydro3D/)

References

[1] Amati, L. 2003, ChJAA, 3S,455 79

[2] Blandford ,R.D. & McKee, C.F. 1976, PhFl, 19.1130 76

[3] Bloom, J. A., Frail, D. A. & Sari, R. 2001, AJ, 121,2879 79

[4] Bowen, D.V., Roth, K.C., Meyer, D.M. & Blades, J.C. 2000, ApJ, 536,225 33, 51, 57

[5] Brighenti, F.& D'Ercole, A. 1997, MNRAS, 285,387 91

[6] Canto, J., Raga, A.C. & Wilkin, F.P. 1996, ApJ, 669,729 89

[7] Castor, J., McCray, R. & Weaver, R. 1975 ApJL, 200,107 7, 14, 72, 74

[8] Chen, Y., Wang, Z.-R. & Qu, Q.-Y. 1995, ApJ, 438, 950

[9] Chevalier, R.A. & Li, Z.-Y. 2000, ApJ, 536,195 9, 73, 79, 81

[10] Chevalier, R.A., Li, Z.-Y. & Fransson, C. 2004, ApJ, 606,369 9, 33, 50, 73, 78, 79, 81, 82, 84, 85

[11] Clocchiatti, A., Wheeler, J.C., Benetti, S. & Frueh, M. 1996, ApJ, 459,547 32

[12] Comerón F. & Kaper, L. 1998, A&A, 338,273 91

[13] Crowther, P. A., Dessart, L., Hillier, D. J., Abbott, J. B.& Fullerton, A. W. 2002, A&A, 392,653 80

[14] Della Valle, M. 2005 astro-ph 0504517 invited review at the 4th Workshop Gamma-Ray Bursts in the Afterglow Era, Rome,18-22 October 2004. Editors: L. Piro, L. Amati, S. Covino, and B. Gendre. Il Nuovo Cimento, in press 69

[15] Dopita, M.A., Cohen, M., Schwartz, R.D. & Evans, R. 1984, ApJL, 287,L69 33, 51, 57

[16] Eldridge, J. J., Genet, F., Daigne, F. & Mochkovitch, R. 2005, MNRAS, submitted, astroph/0509749 82, 88

[17] Eldridge, J.J., & Tout, C.A. 2004, MNRAS, 353,87 3

[18] Fassia, A., et al. 2001, MNRAS, 325,907 33, 51, 57

[19] Fiore , F., et al. 2005, ApJ, 624,853 10, 33, 51, 57

[20] Freyer, T., Hensler, G. & Yorke, H.W. 2003, ApJ, 594,888 2, 34, 58, 60, 72, 75

[21] Fryer, C.L., Heger, A. 2005, ApJ, 623,302 53

[22] Galama, T.J. et al. 1998, Nature, 395,670 33

[23] García-Segura, G. & Franco, J. 1996, ApJ, 469,171 34, 36, 58

[24] García-Segura, G., Mac-Low, M.-M. & Langer, N. 1996a, A&A, 305,229 4, 9, 22, 32, 33, 49, 53, 57, 58, 69, 72, 75, 86

[25] García-Segura, G., Langer, N. & Mac-Low, M.-M. 1996b, A&A, 316,133 4, 5, 9, 15, 22, 32, 33, 34, 35, 36, 57, 58, 60, 72, 75, 86

[26] García-Segura, G., Langer, N., Różyczka, M. & Franco, J. 1999, ApJ, 517,767 8, 17, 22, 34, 36, 37, 58

[27] Ghirlanda et al. 2005, A&A, submitted, astroph/0511559 73

[28] Hamann, W,-R., Koesterke, L. & Wessolowski, U. 1995, A&A, 299,151 81, 92

[29] Holland, S.T. et al. 2003, AJ, 125,2291 79

[30] Huthoff, F. & Kaper, L. 2002, A&A, 383,999 91

[31] Koesterke, L. & Hamann, W.-R. 1995, A&A, 299,503 81, 92

[32] Ikamoto, K. et al. 1998, Nature, 395,672 69

[33] Jaunsen, A. O. et al. 2001, ApJ 546,127

[34] Kwok, S. 2000, The Origin and Evolution of Planetary Nebulae, Cambridge Astrophysics Series 31 (Cambridge University Press, Cambridge) 4, 22, 56

[35] Langer, N. 1991, in *Supernovae*, proc. 10th Santa-Cruz workshop in Astronomy and Astrophysics, ed. S.E. Woosley, Springer-Verlag, p. 549 32

[36] Langer, N. 1998, A&A, 329,551 11, 53

[37] Li, Z.-Y. & Chevalier, R. A. 2003, ApJL, 589,L69 50

[38] MacDonald, J. & Bailey, M.E. 1981, MNRAS, 197,995 8, 23

[39] MacFadyen, A.I. & Woosley, S.E. 1999, ApJ, 524,262 2, 9, 11, 33, 53

[40] Maeder, A. & Meynet, G. 1989, A&A, 210,155 2

[41] Maeder, A. & Meynet, G. 1994, A&A, 287,803 4, 45

[42] Mazzali, P. A., et al. 2003, ApJL, 599,L95 69

[43] Mazzali, P. A. et al. in preparation 69

[44] Meynet, G. & Maeder, A. 2000, A&A, 361,101 32, 56

[45] Meynet, G. & Maeder, A. 2005, A&A, 429,581 52, 53

[46] Miller, G.J. & Chu, Y.-H. 1993, ApJS, 85,137 32

[47] Mirabal, N., et al. 2003, ApJ, 595,935 10, 33, 57

[48] Nakamura, T., Mazzali, P. A., Nomoto, K. & Iwamoto, K. 2001, ApJ, 590,991 69

[49] Ostriker, J.P. & McKee, C.F. 1981, RvPM, 60,10 7, 72, 74

[50] Panaitescu, A. & Kumar, P. 2001, ApJ, 554,667 9, 73, 79, 81

[51] Panaitescu, A. & Kumar, P. 2002, ApJ, 571,779 9, 73, 79, 81

[52] Petrovic, J., Langer, N. & van der Hucht, K.A. 2005 A&A, 435, 1013 11, 69

[53] Petrovic, J., Langer, N., Yoon, S.-C. & Heger, A. 2005, A&A, 435,247 11, 53

[54] Piran, T. 2004, RvMP, 76, 1143 76

[55] Piro, L. et al. 2005, A&A, 623,314 80

[56] Podsiadlowski, P., Joss, P.C. & Hsu, J.J L. 1992, ApJ, 391,246 53

[57] Price, P.A. et a. 2003, ApJ,589,838 79

[58] Rana, N.C.1987 A&A, 184,104 2

[59] Rana, N.C. & Gajria B. 1994 BASI, 22,415 2

[60] Rauw, G. et al. 2004, A&A, 420,L9 95

[61] Rigon, L. et al. 2003, MNRAS, 340,191 9, 33

[62] Schaefer, B.E., et al. 2003, ApJ, 588,387 10, 33, 50, 57

[63] Schaller, G., Schaerer, D., Meynet, G. & Maeder, A. 1992, A&AS, 96,269 3, 11, 34, 58, 82

[64] Stanek, K. Z. et al. 2003, ApJL, 591,L17 33

[65] Starling, R.L.C., Wijers, R.A.M.J., Hughes, M.A., Tanvir, N.R., Vreeswijk, P.M., Rol, E., Salamanca, I. 2005, MNRAS, 360,305 10, 33, 57

[66] Stevens, I. R., Blondin, J. M. & Pollock, A. M. T. 1992, ApJ, 386,265 89

[67] Stone, J.M. & Norman, M. L. 1992, ApJS, 80,753 8, 16, 23, 34, 58, 80

[68] Stratta, G., Fiore, F., Antonelli, L. A., Piro, L. & De Pasquale, M. 2004, ApJ, 608,846 93, 95

[69] Thompson, C. 1994, MNRAS, 270,480 76

[70] van der Sluys, M. & Lamers, H. J. G. L. M. 2003, A&A, 398,181 91

[71] van Dyk, S.D. 1992, AJ, 103,1788 32

[72] van Marle, A.J., Langer, N. & García-Segura, G. 2004, RMXAC, 22,136 (See also Chapter 2 in this thesis) 36, 58, 60, 62, 72, 82, 84

[73] van Marle, A.J., Langer, N. & García-Segura, G. 2005, proceedings of 'Gamma-ray Bursts in the Afterglow Era: 4th workshop' Rome, Eds L. Piro, L. Amati, S. Covino and B. Gendre 22, 51, 57, 60, 62, 72, 82, 84, 86

[74] van Marle, A. J., Langer, N. & García-Segura, G. 2005 A&A 444,837 (See also Chapter 4 in this thesis) 22, 57, 58, 72, 75, 82, 84, 86

[75] van Marle, A. J., Langer, N. & García-Segura, G. 2006a, to appear in the proceedings of 'Workshop: "Stars with the B[e] phenomenon"', Vlieland, the Netherlands, Eds: M. Kraus and A. S. Miroshnichenko,. 6

[76] van Putten, M.H.P.M. 2004, ApJl, 611,L81 51, 53

[77] Villaver, E., Manchado, A. García-Segura, G. 2002, ApJ, 581,1204 32

[78] Wang, L., Baade, D., Höflich, P. & Wheeler, J.C. 2003, ApJ, 592,457 32

[79] Weaver, R., McCray, R., Castor, J., Shapiro, J. & Moore, R. 1977, ApJ, 218,377 4, 7, 14, 34, 53, 57, 72, 73, 74, 75, 92

[80] Wellstein, S. & Langer, N. 1999, A&A, 350,148 53

[81] Wijers, R. A. M. J. 2001, in Second Rome Workshop on GRBs in the Afterglow Era, E. Costa, F. Frontera, & J. Hjorth (Berlin: Springer), 306 73, 80

[82] Wilkin, F.P. 1996, A&A, 459,31 91

[83] Woo, J.O. 1991, PASAu, 9,275 81

[84] Woosley, S.E. 1993, ApJ, 405,273 2, 9, 33

[85] Woosley, S. E., Eastman, R. G. & Schmidt, B. P. 1999, ApJ, 516,788 69

[86] Woosley, S.E, Heger, A. & Weaver, T.A. 2002, RvMP, 74,1015 2

[87] Yoon, S.-C. & Langer, N. 2005, A&A, 435,967 11, 80, 81

[88] Young, Y.-N., Tufo, H., Dubey, A. & Rosner, R. 2001, J. Fluid. Mech. 447,377 22, 24

[89] Zeh, A., Klose, D. & Kann, D. A. 2005, astro-ph/0509299 73

list of some abbreviations

A&A :	Astronomy & Astrophysics
A&AS :	Astronomy & Astrophysics Supplement
AJ :	Astronomical Journal
ApJ :	Astrophysical Journal
ApJL :	Astrophysical Journal Letters
ApJS :	Astrophysical Journal Supplement
BASI :	Astronomical Society of India Bulletin
ChJAA :	Chinese Journal of Astronomy & Astrophysics
J.Fluid.Mech. :	Journal of Fluid Mechanics
MNRAS :	Monthly Notices of the Royal Astronomical Society
PASAu :	Proceedings, Astronomical Society of Australia
RvMP :	Review of Modern Physics
RMXAC :	Revista Mexicana de Astronomía y Astrofísica (Serie de Conferencias)

Nederlandse Samenvatting

Inleiding

Zware sterren ($\gtrsim$ 10 zonsmassa) zijn betrekkelijk zeldzaam. Op elke 100 sterren met een massa vergelijkbaar met de massa van de zon, wordt slechts één ster gevormd met een tien keer zo grote massa. Aangezien zware sterren veel korter bestaan dan lichte, wordt dit verschil in aantal op den duur alleen maar groter. De lichte sterren blijven bestaan, terwijl de zware sterren verdwijnen. Toch zijn zware sterren van grote invloed op de ontwikkeling van een sterrenstelsel, aangezien zij de bron zijn voor zware elementen. Deze worden in de kern van zware sterren gevormd en komen vrij aan het einde van de evolutie van zo'n ster. Ook tijdens hun korte bestaan oefenenen zij een aanzienlijke invloed uit op hun omgeving, door een grote hoeveelheid massa en energie af te stoten. De dood van een zware ster is bijzonder spectaculair, want het zijn deze sterren, die als supernovae exploderen en daarbij gedurende een korte tijd even veel licht geven als een heel melkwegstelsel. Daarbij stoten zij een groot deel van hun resterende massa af en wel met zo'n snelheid, dat de verstoring van het omringende gas een nieuwe ronde van stervorming kan induceren. Tevens wordt verondersteld dat zware sterren de bron zijn van zogenaamde 'gamma flitsen'.

In dit proefschrift beschrijven wij het effect, dat een zware ster heeft op zijn omgeving. Het verband tussen zware sterren en gamma flitsen wordt onderzocht, door onze eigen computermodellen van het circumstellaire medium rond zware sterren te vergelijken met observaties en theoretische modellen voor langdurige gamma flitsen

De omgeving van een zware ster

Een zware ster start zijn evolutie als een bol gas, die in het centrum energie produceert door waterstof fusie. Tegelijkertijd verliest de ster energie aan het oppervlak in de vorm van straling en sterrenwind. Dit laatste is een stroom van gas, die met hoge snelheid het oppervlak van de ster verlaat. Deze sterrenwind komt in botsing met de omringende, interstellaire materie en veegt deze op in een schil, die door de energie van de wind van de ster af wordt geduwd. Op deze wijze blaast de ster een bel om zichzelf heen in het interstellaire gas. Zo'n bel kan bijzonder groot worden (enige tientallen lichtjaren) en blijft bestaan gedurende de volgende interakties.

Zolang de ster voldoende waterstof in de kern heeft om de kernfusie reactie gaande te houden (we spreken in deze periode van een hoofdreeks ster) veranderen de eigenschappen van de ster en de sterrenwind nauwelijks. Pas wanner de waterstof uitgeput raakt (voor een zware ster na enige miljoenen jaren) ontstaat een nieuwe fase. De ster verlaat de hoofdreeks. In de kern wordt nu helium gefuseerd in plaats van watersof, terwijl in een

schil rond de kern waterstof gefuseerd wordt.

De ster zal opzwellen tot een rode superreus of een 'Luminous Blue Variable'. Dergelijke sterren hebben een veel tragere wind dan hoofdreeks sterren, maar tegelijkertijd verliest de ster veel meer massa aan het oppervlak, waardoor de dichtheid van de wind aanzienlijk (100-1000 keer) toeneemt. Als gevolg hiervan wordt in het circumstellaire medium een nieuwe schil gevormd.

Indien de oorspronkelijke ster zwaar genoeg was ($\gtrsim 25$ zonsmassa's aan het begin van de evolutie) volgt na de rode superreus of Luminous Blue Variable periode een 'Wolf-Rayet' fase, waarbij de snelheid van de sterrenwind weer toeneemt, terwijl de dichtheid van de wind betrekkelijk hoog blijft. Deze nieuwe, snelle wind veegt de dichte rode superreus of Luminous Blue Variable wind op in een derde schil, die met de tweede in botsing komt. Beide schillen worden door deze botsing vernietigd en hun overblijfselen zullen mettertijd in het omringende gas opgenomen worden.

Het scenario, hierboven beschreven, wordt nog gecompliceerder als men bedenkt, dat de ster ook een aanzienlijke portie energie afstoot in de vorm van fotonen. Deze zijn in staat om het omringende gas te ioniseren. Dit heeft als gevolg dat de druk en temperatuur van het gas toenemen, en er kan zich een zogenaamd HII gebied (een bel van geïoniseerd waterstof gas om de door de wind gevormde bel heen vormen. Net als de eigenschappen van de sterrenwind is ook het aantal photonen afhankelijk van de fase waarin de ster zich bevindt.

Doordat veranderingen in de eigenschappen van de sterrenwind en straling hun afdruk nalaten op het omringende gas, wordt de circumstellaire bel als het ware een afspiegeling van de evolutie van de ster en kan gebruikt worden om de voorafgaande evolutie van de ster te analyseren. Door de morfologie van het circumstellaire medium te onderzoeken kunnen wij nagaan in welk stadium van de evolutie de centrale ster zich bevindt en welke fasen hieraan vooraf zijn gegaan.

Al deze interacties kunnen met behulp van analytische en numerieke technieken beschreven en gesimuleerd worden. Op deze manier hebben wij computermodellen ontwikkeld voor de evolutie van het circumstellaire medium rond zware sterren.

Het maken van dit soort modellen vereist een krachtige computer en een hoop rekentijd. Om nu de simulaties in een redelijke tijd te kunnen voltooien moest het probleem worden vereenvoudigd. Dit bleek mogelijk door het aantal dimensies van de simulaties terug te brengen. Uiteraard is het circumstellaire medium driedimensionaal, maar we kunnen in veel simulaties volstaan met twee of zelfs één dimensie. De ster zelf is bolvormig, dus is de sterrenwind in alle richtingen min of meer gelijk (deze symmetrie wordt verbroken als de ster roteert, of in geval van een sterk magnetisch veld!). Dit betekent, dat de afstand tot de ster de belangrijkste dimensie is, wat het mogelijk maakt om ééndimensionale simulaties te doen, waarbij lengte- en breedtegraad van de bolvormige structuur achterwege gelaten worden. Het probleem hiermee is dat veel van de hierboven beschreven hydrodynamische interacties instabiel zijn, zodat lokale variaties optreden, die in een ééndimensionale simulatie niet voorkomen. Het is noodzakelijk om meer gedetailleerde simulaties in minimaal twee dimensies uit te voeren, om te onderzoeken of deze instabiliteiten van belang zijn voor de evolutie van het circumstellaire medium. Een driedimensionale simulatie is natuurlijk het beste, maar uit ons onderzoek blijkt, dat het verschil tussen twee- en driedimensionale resultaten in de meeste gevallen niet zo groot is dat het de toename in rekentijd rechtvaardigt.

Gamma flitsen

Van langdurige gamma flitsen wordt verondersteld, dat ze voorkomen aan het einde van de evolutie van sommige zware sterren. Het meest geaccepteerde model hiervoor werkt als volgt. Als een zware ster het einde van zijn leven heeft bereikt, stort hij in. Hierbij vormt zich in het centrum een 'zwart gat', met daaromheen een schijf van materie, die geleidelijk in het zwarte gat verdwijnt. Bij dit proces komt een hoop energie vrij, die zich in de vorm van 'jets' (stralen geconcentreerd gas, dat zich in één bepaalde richting voortbeweegt) vanaf de polen van het zwarte gat naar buiten bewegen. Aangezien deze beweging veel sneller plaatsvindt dan de geluidssnelheid (In feite komt de snelheid van deze jets in de buurt van de lichtsnelheid!) ontstaat een schok front, wat de gamma straling produceert, die wij als een gamma flits waarnemen. Naarmate zo'n jet zich verder van de ster af beweegt veegt hij meer van het omringende (circumstellaire) gas op. Hierbij komt ook energie vrij, die wij zien als de zogenaamde nagloed (afterglow).

Aangezien deze nagloed geproduceerd wordt in het circumstellaire medium, dat in paragraaf 6.5 werd beschreven, kunnen wij de waarnemingen van de nagloed gebruiken om het circumstellaire medium rond een gamma flits te onderzoeken. Via deze weg hopen wij een relatie te kunnen vinden tussen de eigenschappen van gamma flitsen en van het circumstellaire medium om vast te kunnen stellen welke zware sterren de gamma flitsen veroorzaken.

Dit kan op twee manieren:

A: De nagloed wordt geproduceerd doordat de gamma flits jet het omringende gas opveegt. Daarom is de intensiteit van de nagloed afhankelijk van de dichtheid van dit gas. Aangezien de bron van de gamma flits een zware ster is, verwachten wij dat de dichtheid van het omringende gas zal afnemen met het kwadraat van de afstand, want dit is het dichtheidsprofiel van een sterrenwind. Echter, in een aantal gevallen blijkt dit niet zo te zijn. De dichtheid van het gas lijkt constant. Wij trachten hiervoor een verklaring te vinden.

B: De nagloed wordt opgewekt binnen in de circumstellaire bel en dat gedeelte van de bel, dat zich tussen de nagloed en de waarnemer bevindt, zal het licht van de nagloed absorberen, hetgeen resulteert in de waarneming van de circumstellaire bel als absorptie lijnen in het spectrum van de nagloed. In de nagloed van gamma flits GRB 021004 zijn inderdaad een groot aantal absorptie lijnen te zien. Uit het spectrum is afgeleid, dat er zich gas in het circumstellaire medium bevindt, dat zich met een aantal verschillende, discrete snelheden beweegt ten opzichte van de centrale ster. Deze snelheden variëren van nul tot enige duizenden kilometers per seconde. Met behulp van onze modellen voor het circumstellaire medium proberen wij het bestaan van deze absorptie lijnen te verklaren. Vervolgens kunnen wij het resultaat gebruiken als middel om een protocol voor de evolutie van de centrale ster op te stellen.

Conclusies

De resultaten van ons onderzoek leiden ons tot de volgende conclusies:
Wat betreft de aanwezigheid van een medium met constante dichtheid in de buurt van een zware ster, is de verklaring, dat de nagloed van de gamma flits wordt opgewekt in

dat gedeelte van de wind, dat al door de botsing met het omringende gas tot stilstand is gebracht. Deze geschokte materie heeft inderdaad een vrijwel constante dichtheid, maar blijkt in onze simulaties te ver van de ster verwijdert te zijn. Om dit gebied dichter bij de ster te brengen is een combinatie van interne en externe factoren noodzakelijk. Externe factoren, zoals hoge dichtheid of druk in het interstellaire gas of, de eigen beweging van de ster in de ruimte, kunnen verklaren dat de hele circumstellaire bel klein is, waarbij ook het gebied met constante dichtheid dichter bij de ster komt. Een dergelijke verklaring is echter meestal niet voldoende. Maar, voor een relatief zwakke sterrenwind (lage snelheid, weinig materie) is het wel mogelijk om dit gebied dicht genoeg bij de ster te brengen. Zo'n zwakke wind kan in verband worden gebracht met de chemische samenstelling van de ster. Als de ster weinig zware elementen bevat, neemt het massa-verlies namelijk af. Dit, in combinatie met de bovengenoemde externe factoren is voldoende om de aanwezigheid van een gebied met constante dichtheid in de buurt van een groot aantal gamma flitsen te verklaren.

Ter verklaring van de waargenomen absorptie lijnen in het spectrum van de nagloed van gamma flits GRB 021004 analyseren we de hydrodynamische interacties in het circumstellaire medium. Absorptie door materie, die stilstaat ten opzichte van de ster, is niet moeilijk te vinden. Het interstellaire gas staat namelijk min of meer stil ten opzichte van de ster. Bovendien zijn de waarnemingen niet zo nauwkeurig dat kleine ($\lesssim$ 10 $\mathrm{km\,s^{-1}}$) snelheidsverschillen opgemerkt worden, waardoor elke vorm van traag bewegend gas bijdraagt aan deze absorptie component. De absorptie lijnen die duiden op gas met een snelheid van ongeveer 3000 $\mathrm{km\,s^{-1}}$ kunnen verklaard worden met de sterrenwind van de Wolf-Rayet ster zelf. Echter, de absorptielijnen die duiden op gas met snelheden tussen de 150 en 650 $\mathrm{km\,s^{-1}}$ vormen een groter probleem. De meest aannemelijke verklaring is dat ze afkomstig zijn van een schil, voortgedreven door de Wolf-Rayet wind in het gas van een eerdere, langzamer wind. Aangezien de levensduur van een dergelijke schil slechts kort is, brengt de aanwezigheid van deze lijnen in het spectrum ons tot de conclusie dat de Wolf-Rayet fase nog korter geweest moet zijn. Dit betekent een inperking van de mogelijke evolutie van de ster. Een begrenzing die ons kan helpen bij het speuren naar die sterren die gamma flitsen zouden kunnen veroorzaken.

Acknowledgements

It has been four years since I finished my Masters thesis and now that I have completed my PhD thesis, I find myself back where I was then: trying to thank the people, who helped me to come this far.

First of all I wish to thank my parents for their love and support during all these years.

I also want to express my gratitude to my supervisor, Norbert Langer, for giving me the opportunity to do my PhD research and for his guidance during the past four years and to Guillermo García-Segura and Bram Achterberg for their help with my research and my papers.

I also owe a dept of gratitude to the people of the AstroHydro 3D project; Vincent Icke, Garrelt Mellema, Erik-Jan Rijkhorst, Jelle Ritzerveld and the others from whose experience and knowledge I benefited.

I am grateful to Wim Rijks for his work on the parallel version of the ZEUS code, and to the members of the gamma-ray burst group at the Anton Pannekoek Institute in Amsterdam who helped me understand the observations of gamma-ray burst afterglows.

Last, but certainly not least, I want to thank all my colleagues at the Astronomical Institute; their interest, their support and their critique during these past four years have been greatly appreciated.

If I have forgotten to mention anyone who feels that they should have been thanked, I can only beg your pardon. The fault lies in my wretched memory, not in you.

Curriculum Vitae

Place and date of my birth are Amsterdam, Sunday, March 19th, 1978. Two months later my family moved to Hilversum, where I attended a protestant primary school and a non-denominational grammar school (Gemeentelijk Gymnasium Hilversum). In 1996 I passed my final exams and that same year started to study (theoretical) physics at the University of Amsterdam. During this period the Science Faculty offered the, to me welcome, opportunity to study both Physics and Astronomy at the same time. On April 29th, 2002 I graduated in both subjects under the supervision of Leo van den Horn (Institute for Theoretical Physics) and Gert-Jan Savonije (Astronomical Institute Anton Pannekoek) on the subject 'Non-Radial Oscillations in a proto-Neutron Star Model'. I did my stint as student representative in the Educational Committee of the Faculty during my 5th year, a challenging but rewarding job.

In May 2002 I started my career as Assistent in Opleiding with Norbert Langer at the Department of Astronomy, University of Utrecht, on the subject of 'Circumstellar medium of massive stars', the result of which is this thesis. The research was part of the AstroHydro 3D project.

Moreover, during the four years at the Department of Astronomy I was given ample scope to develop skills in Theoretical and Computational Astrophysics and to attend workshops and conferences to enhance and share my knowledge.